DEVELOPMENT OF MICRO-PATTERN GASEOUS DETECTORS – GEM

Diploma Thesis of the Physics Department
of the
Ludwig-Maximilians-Universität of Munich

presented by

David Heereman von Zuydtwyck

November 2010

Erstgutachter: Prof. Dr. Otmar Biebel
Zweitgutachter: Prof. Dr. Wolfgang Dünnweber

Dedicated to Engin Abat
29/09/1979 - 30/11/2007

Abstract

After the planned high-luminosity upgrade of the **L**arge **H**adron **C**ollider at CERN to finally $\mathscr{L} = 5 \times 10^{34}$ cm^{-2}s^{-1} part of the detectors in the forward region of the ATLAS muon spectrometer will be no longer able to cope with the proportionally increasing background. The muon detectors experiencing highest rates are the cathode strip chambers (CSC), that will by that time also reach their expected lifetime, as well as the monitored drift tube (MDT) chambers sitting close by. At occupancies of up to 70% for the latter, unique track reconstruction is expected to be no longer possible. The spatial resolution of a single drift tube is supposed to be deteriorated largely by space charge effects.

Gaseous detectors based on the **G**as **E**lectron **M**ultiplier technique (GEM) can be operated as fast muon detectors. Space charge effects are intrinsically reduced.

The present work reports the development of a triple GEM detector to achieve high spatial resolution. Several versions of the detector are built and investigated: one with an unsegmented anode, one with five-fold segmented anode, one version with 360 anode strips of 150 μm width and a pitch of 250 μm to be read out by GASSIPLEX frontends and a similar device with 384 strips to be read out by APV25 frontends. All versions feature an active area of 100×100 mm^2 and are filled with Ar/CO_2 gas at a ratio of $93/7$. Stable operation over several days is achieved. 5.9 keV X-rays from a ^{55}Fe source and cosmic muons are used to investigate and characterize signal formation, rise time, efficiency and energy resolution. Thereto the signals are recorded using a charge sensitive preamplifier and a 1 GHz flash analog-to-digital converting (ADC) readout system. Studies are performed by varying the voltage difference at the GEM foils or across the drift gap and induction gap of the detector with optimized operational parameters. Energy resolutions of approximately 18% and efficiencies over 95% are observed. Pulse height variations in dependence of the size of the readout strips is investigated. The difference between the rise time of 5.9 keV X-ray and muon induced signals is quantitatively understood. The implementation of a highly segmented anode for spatial resolution measurements is completed for two different readout systems. Data taking is under way for the GASSIPLEX based version. Preliminary results recorded with this readout system during the last three days before due-date of the presented thesis yield a position resolution of $79 \pm 5\ \mu m$. The readout chain for the APV25 based frontends is designed and the boards are in production. Tests of the triple GEM detectors' tracking capability of 140 GeV muons at the H8 beam line at CERN and their position accuracy of cosmic muon detection at increased background of gammas or neutrons are foreseen. Larger active areas are achievable, such that they are a viable candidate for replacement of the CSC and the drift detectors in their vicinity.

Contents

Introduction

Our universe is momentarily described by the standard model [Grif 08]. It contains three generations of *leptons* consisting of electron, muon, tau and their corresponding neutrinos and six *quarks*, namely the up and down, charm and strange as well as top and bottom. They represent the *fermions*, spin $\frac{1}{2}$ - particle.
Interactions are mediated via *bosons*: the photon responsible of the electromagnetic interaction, the W^-, W^+ and Z bosons for the weak interaction and eight gluons as carrier of the strong force.

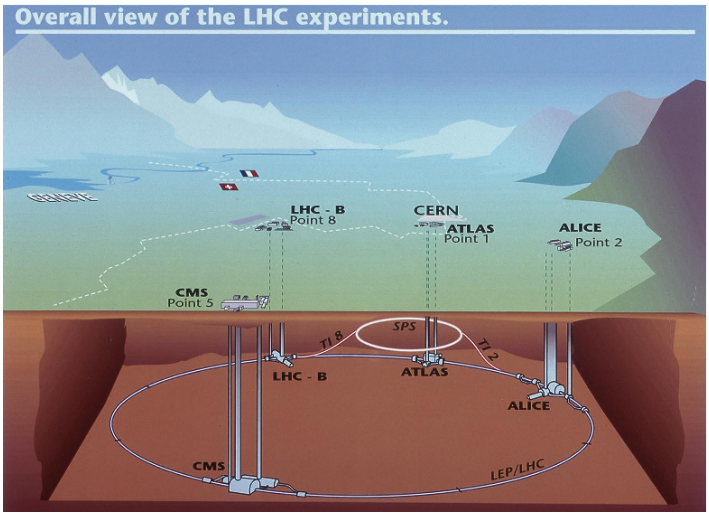

Figure 1: The LHC near Geneva and the installed experiments [CERN 10].

About 100 m deep underground in the **L**arge **H**adron **C**ollider at CERN[1] (cf. Fig 1) near Geneva protons collide at center-of-mass energies of up to 14 TeV to further investigate nature. A main interest is the question of the generation of mass that is supposed to result from the Higgs mechanism. To study the physics of these collisions, detectors are installed around the beam interaction points.

One of them is the ATLAS[2] detector, shown in Fig. 2. It is a multi purpose detector of 44 m length and 25 m height that detects the reaction products of proton collisions designed to occur every 25 ns [ATLA 10]. The detector has a multi layer structure beginning with the inner tracking detectors ("SCT[3]", "Pixel Detector" and "TRT[4]" in Fig. 2) near the collision point and in a solenoid magnetic

[1] European Organization for Nuclear Research
[2] **A** **T**oroidal **L**HC **AS**
[3] **S**emi **Conductor** **T**racker
[4] **T**ransition **R**adiation **T**racker

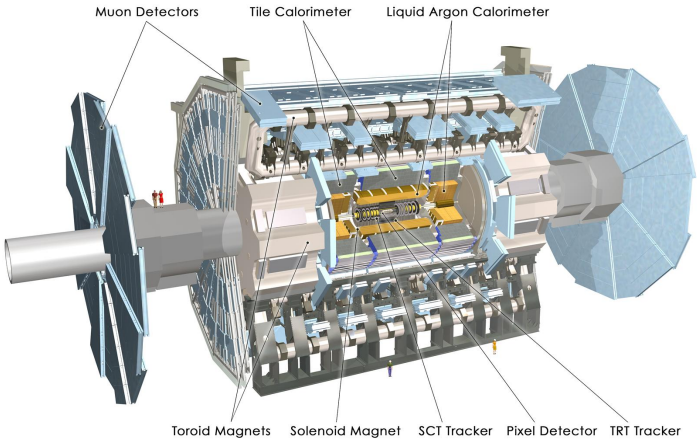

Figure 2: Schematics of the whole ATLAS detector [ATLA 10].

field of 2 T. The hadronic ("Tile Calorimeter") and electromagnetic ("Liquid Argon") calorimeters are responsible for measuring the energy deposited by the corresponding particle in the material. In the outer region the muon chambers surround the detector in three layers. Only muons reach this area as all other particle are supposed to be absorbed in the inner layers. The muon system consists of cathode strip chambers (CSC) and Ar/CO_2 filled drift tube chambers placed in a toroidal magnetic field of 0.4 T for measuring the momentum of the traversing charged muons by their radius of curvature. Resistive plate chambers and thin gap chambers provide the trigger.

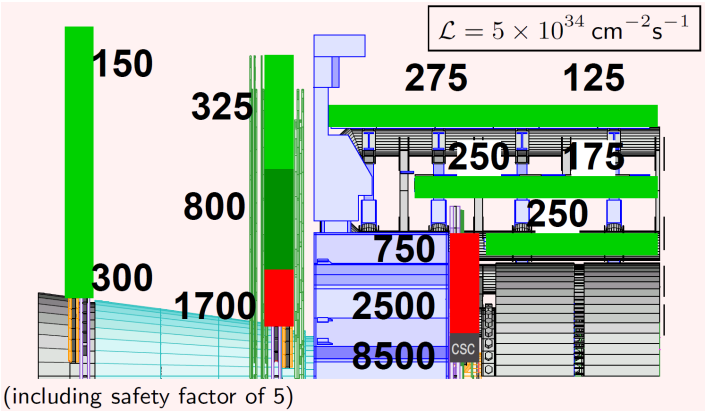

Figure 3: Expected background rates in $\left[\frac{Hz}{cm^2}\right]$ at five times LHC luminosity [Loeb 10].

Additionally to the primary collision products from the proton-proton collision, background radiation is produced, mostly by interactions in the collimator. For the planned luminosity upgrade to $5 \cdot 10^{34}$ cm^{-2}s^{-1} for SuperLHC the proportionally increased background rate will decrease the performance of specific detector regions.
Fig. 3 shows the expected background rate in the muon spectrometer. Mostly affected are the CSC and the muon chambers sitting close by. Estimated background rates in the detector reach here values of 8500Hz/cm^2. Due to their intrinsic insensitivity to space charge effects, large area GEM detectors are considered as replacement candidates.
To study the influence of high radiation background on ATLAS MDT chambers our working group

is testing tubes with alternative drift gases and geometries at background rates up to 1 MHz per tube provided by 662 keV γ-rays or fast neutrons.

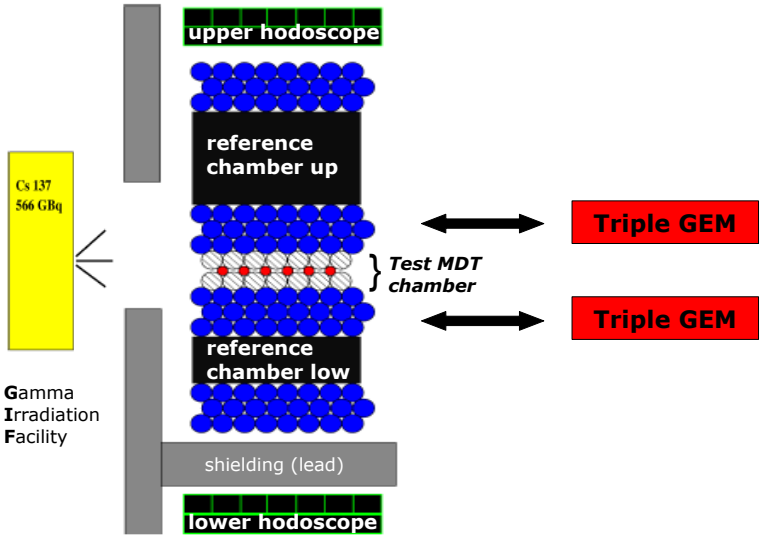

Figure 4: Schematic of the GIF assembly with prototype of drift tubes, reference chambers and trigger hodoscope [Adom 10] for tracking cosmic ray muons. Alternatively a tracking system of triple GEM detector replacing the reference chambers is shown.

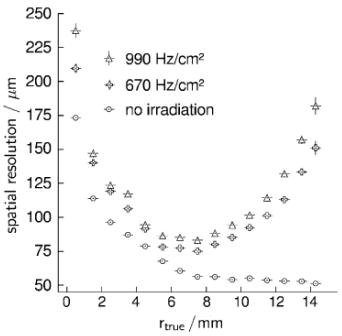

Figure 5: Spatial resolution of 30 mm drift tubes for muons under gamma rates [Deil 04].

Research on the effect of high gamma background is done in the GIF[5] at CERN where prototype chambers can be irradiated with a ^{137}Cs source that emits 662 keV gammas at an activity of 566 GBq [Adom 10]. Fig. 4 shows how the test chamber is placed in the GIF setup between two reference chambers and a trigger hodoscope. The resolution of the reference chambers decreases under irradiation due to space charge effects, as shown in Fig. 5. A detector traversing muon creates electron-ion pairs in the tube, the electrons drift to the anode wire and are amplified by electric field that increases proportional to the distance to the wire ($\propto 1/r$). Ions liberated by heavy γ-irradiation in the drift volume increase the space-charge density that affects the drift velocity of the electrons. This results in a decrease of gas gain worsening the resolution at small radii and space charge fluctuations reducing the resolution at large radii as shown in Fig. 5.
In gaseous detectors based on the **G**as **E**lectron **M**ultiplier principle (GEM) [Saul 97] space charge effects are suppressed. A tracking system of triple GEM detectors replacing the reference chambers would be an alternative solution and would also strongly increase the opening angle for cosmic ray muons. Here fore 30 cm^2 large GEM detectors are envisaged.
Muon track determination was investigated at the H8 beam line at CERN with a 140 GeV muon beam. In this setup, shown in Fig. 6, an MDT prototype chamber with 15 mm diameter tubes was under investigation. As in the GIF assembly a reference system built of standard MDTs with 30 mm diameter was installed to monitor the muon track. Additionally two scintillators in front of the test chamber provide a trigger for the readout. For this assembly, a tracking system with high spatial resolution would be useful to monitor the beam. It would considerably ease the analysis.
The spatial resolution of the muon reference chamber could be easily improved by implementing a

[5] **G**amma **I**rradiation **F**acility

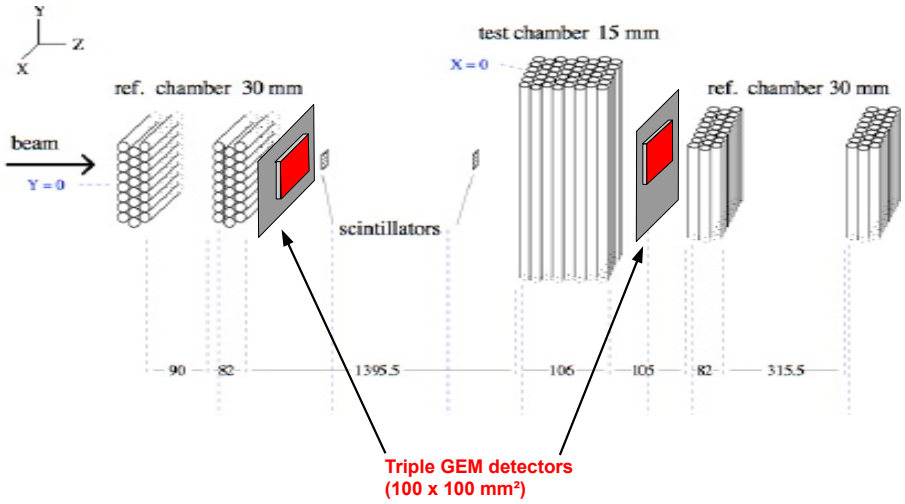

Figure 6: Schematic of the H8 beam setup with prototype of 15 mm drift tubes and reference chambers. A tracking system by triple GEM detectors replacing the reference chambers is proposed.

new tracking system of four 10×10 cm^2 GEM detectors with a spatial resolution of approximately 50 μm. This is one motivation of this thesis.
With the implementation of the micro-pattern gaseous detectors developed in this thesis the problem of space charge effects can be strongly reduced.

The present thesis deals with the construction of triple GEM detectors with active areas of 10×10 cm^2. Principle, manufacturing and operation of the GEM foil are explained in Ch. 2.
The construction of a triple GEM "prototype 1.0" with an unsegmented as well as with a five-fold segmented copper anode is documented in Ch. 3. The description includes the monitoring of the HV supply and the Ar/CO_2 gas mixture at a ratio of $93/7$.
Analog signals are recorded using a charge sensitive preamplifier followed by a 1 GHz flash ADC. The analysis is based on an inverse Fermi-fit to the signals generated by cosmic muons or 5.90 keV X-rays from a ^{55}Fe source.
After optimization of the voltage differences across the GEM foils or across the drift gap and induction gap 18% FWHM energy resolution of the 5.90 keV K_α line is observed.
The energy resolution at the outer regions of the active area is 10% to 20% better compared to the central source location indicating deformations of the GEM foils as discussed in Ch. 4.2.
Ch. 4.3 treats the analysis of cosmic muon signals. It is shown that the measured energy loss corresponds to a Landau-like distribution. The mean energy loss agrees with the theoretical estimate within 8% deviation.
Studies on the pulse height as a function of the induction field are presented in Ch. 4.4. An almost linearly increase in the observed field range from 0.05kV/cm to 2.33kV/cm is measured as expected by the charge transfer processes in a GEM detector.
Pulse height variations in dependence of the size of the readout plane are investigated using a five-fold segmented anode. In Ch. 4.5 the pulse height is increasing at smaller size of the readout strips. An explanation correlating the increasing signal with decreasing capacity describes data, but further investigation is necessary for complete understanding.
The muon detection efficiencies are reported in Ch. 5. The implementation of stable gas flow and pressure leads to an efficiency over 95%. Variations of the temperature are observed to worsen the

efficiency. Monitoring of this parameter is recommended. Stable operation of the detector over several days is observed.
Rise time studies in Ch. 6 compare the difference in the rise time of cosmic events and X-ray generated events. Muons create primary charge-pairs along their track all over the drift gap whereas ^{55}Fe X-ray interact punctually. Comparing the rise times of both signal types with simulated electron drift times across the drift gap allows for explanation of the difference.
In Ch. 7 the gas gain follows the predictions of Townsend's theory. Increasing the potential difference at the GEM foils results in an exponential rise of the gas gain reaching maximum values of 10^4 for voltage differences at the GEM foils of $\Delta U_{GEM} = 350$ V in Ar/CO_2 at a ratio of $93/7$.

The last chapter of this thesis documents the design and implementation of a second prototype equipped with a highly segmented anode to achieve spatial resolution. Ch. 8.1 describes the design of two different readout systems. A readout system based on the GASSIPLEX chip is presented in Ch. 8.2. It is implemented for a triple GEM detector with $90 \times 100\text{mm}^2$ anode segmented into 360 strips of 150 μm width and 250 μm pitch. Data taking just started and is momentarily ongoing. First results yield a position resolution around 70 μm.
As the availability of GASSIPLEX frontends is limited, Ch. 8.3 provides a readout chain based on the APV25 chip. The production of the required parts is in progress and will be completed soon.

Before the presentation of these results an introduction to the physical processes in a gaseous detector is given in the upcoming Ch. 1. Many details of the interactions of charged particle and photons in matter are needed in the following chapters.

Chapter 1

Interactions of Charged Heavy Particle and Photons in Matter

This chapter deals with the physics inside a gaseous detector. The interaction of charged heavy[1] *particle in matter and the derivation of their specific energy loss according to Bethe-Bloch is presented before the primary interactions of photons with matter. Ch. 1.2 documents the behavior of liberated charges in a gas volume with or without an applied electric field leading to the principle of gas amplification.*

1.1 Primary Processes in Gaseous Detectors

[Grup 08, Ch.1], [Bieb 08, Ch.2], [PDG 10], [Leo 94], [Klei 92]
When a particle interacts with matter, the physical reaction can be abstracted to an interaction of a (virtual) photon with an atom. This is called the Photo-Absorption-Ionization-Model and will be illuminated in the following to guide to the important primary processes of particle in gaseous detectors.

1.1.1 Ionization and Excitation

Model of Photo-Ionization and -Absorption

The interaction of heavy charged particle with matter is of electromagnetic nature and therefore mediated by photons.

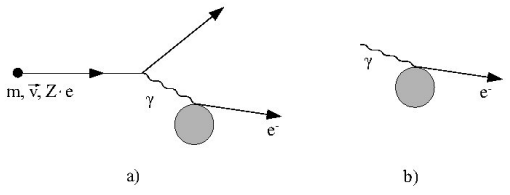

Figure 1.1: Photo-ionization-absorption model

In the so called *photo-ionization-absorption model* one treats the electromagnetic interaction, that is the energy loss, of a particle with charge $q = Z \cdot e$, mass m and velocity $\vec{v} = \vec{\beta} \cdot c$ like the

[1] heavy relative to an electron

electromagnetic interaction of a photon that carries the energy $E = \hbar\omega$ and momentum $\vec{p} = \hbar\vec{k}$ (cf. Fig. 1.1a and 1.1b). Furthermore this photon is not interacting with a single target but is traveling through a medium of refraction index n or with a dielectric constant $\varepsilon = \varepsilon_1 + i\varepsilon_2$ with $n^2 = \varepsilon_1$ respectively. Looking at ε, it is clear that the photon can be virtual since $\hbar\omega = c \cdot \hbar|\vec{k}|$ and accordingly in a medium $\omega = c \cdot |\vec{k}| \cdot (n)^{-1}$. Thus the interaction of a particle with matter, which is basically the energy loss of this particle, is described by the interaction of a photon with matter.

Involving this model in more serious calculations one considers the relativistic energy-momentum conservation of the process described in Fig. 1.2.

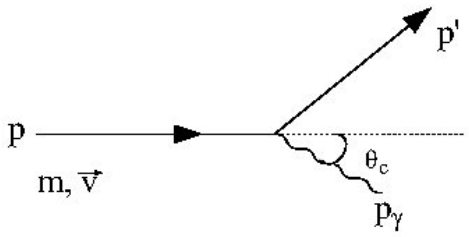

Figure 1.2: Four-momentum of photon-matter-interaction

The conservation of energy and momenta says:

$$p' = p - p_\gamma \tag{1.1}$$

with the four-momenta of the involved candidates:

$$p = \begin{pmatrix} \frac{E}{c} \\ \vec{p} \end{pmatrix} = \begin{pmatrix} \gamma mc \\ \gamma m\vec{v} \end{pmatrix} \tag{1.2}$$

for the incident particle and

$$p_\gamma = \begin{pmatrix} \frac{E_\gamma}{c} \\ \vec{p}_\gamma \end{pmatrix} = \begin{pmatrix} \frac{\hbar\omega}{c} \\ \hbar\vec{k} \end{pmatrix} \tag{1.3}$$

for the emitted (virtual) photon respectively.
Putting this relation in the squared Eq. 1.1 and making the assumption that the photon carries low energy and momentum:

$$\hbar\omega \ll \gamma \cdot m \cdot c^2 \;\; \& \;\; \hbar k \leq \gamma \cdot m \cdot v \tag{1.4}$$

one gets an expression for the angular frequency of the photon in connection with the angle of emission and the particle's velocity :

$$\omega = v \cdot |\vec{k}| \cdot \cos\theta_c = \vec{k} \cdot \vec{v} \tag{1.5}$$

where θ_c is the angle where the so called *Cerenkov-radiation* can be observed if the particle is traveling through matter faster than the speed of light in this medium.
Together with the dispersion relation for (real) photons in matter:

$$\omega^2 = \frac{(\vec{k} \cdot c)^2}{\varepsilon} \quad . \tag{1.6}$$

The energy loss of the incident particle is classified in three different ranges depending on ω or the energy of the photon respectively:

- Considering E_γ to be in the range of some eV. This leads to real-valued ε and θ_c and therefore a real photon. This means one can observe the already mentioned *Cerenkov radiation*.
- If the Photon carries energy bigger than some keV and is traversing from one medium into another the so-called *transition radiation* occurs. However, in homogeneous matter no interaction at all is observed which is defined as *transparency*.
- The most important case for gaseous detectors lies in the energy range between the two mentioned. A photon carrying an energy from eV to some keV has a complex-valued ε and this results in either *absorption* of the photon or **ionization** and **excitation** of the target matter caused by the energetic photon.

The energy loss of a (virtual) photon scattered on an electron depends on the energy and momentum of the former:

$$\frac{d^2\sigma}{dE\ dp} \tag{1.7}$$

with $E = \hbar\omega$ and $p = \hbar k$. An analytical integration over the momentum p leads to an approximation of the mean energy loss per unit length:

$$\frac{dE}{dx} \approx -\int_I^{T_{max}} E \cdot \frac{d\sigma}{dE}\ dE \tag{1.8}$$

where I is the mean ionization potential of the atom. T_{max} is the maximum energy transfer to an electron at rest, i.e. in a central collision.

Average Energy Loss by Ionization and Excitation

Executing the integration of Eq. 1.8, one obtains the **Bethe-Bloch** formula, that gives the average energy loss dE per length dx of a heavy charged particle in matter:

$$\boxed{-\left\langle \frac{dE}{dx} \right\rangle = 2\pi \cdot N_A \cdot \rho \cdot r_e^2 m_e c^2 z^2 \frac{Z}{A} \frac{1}{\beta^2} \left(\ln \frac{2m_e c^2 \gamma^2 \beta^2 \cdot T_{max}}{I^2} - 2\beta^2 - \delta - 2\frac{C}{Z} \right)} \tag{1.9}$$

This formula represents a generally good approximation for the energy loss of charged particles by excitation and ionization in matter, it contains:

- The incident particle's Lorentz factor γ and its velocity β, that include its energy and momentum, as well as its mass m and charge z in units of the elementary charge.
- The excited or scattered electron's classical radius r_e and its mass $m_e c^2$

- The matter's atomic number Z, atomic weight A and density ρ, the Avogadro number N_A, it's ionization potential I and the maximum energy transfer T_{max}.

The additional terms in the brackets refer to corrections, firstly the density effect δ which describes the screening of the incident particle's electric field by the charge density of the atomic electrons. It can be neglected for gases under normal pressure thus it is important for dense absorbers. The second corrections C is due to the movement of the electrons in the shells .

The energy loss decreases like $1/\beta^2$ in the low momentum range and reaches a minimum near $\beta\gamma \approx 4$. Comparing the minima of different absorbers one observes a decreasing energy loss at the ionization minimum with increasing atomic number of the absorber. These characteristics are mainly due to the Z/A term in Eq. 1.9 and is shown in Fig. 1.3.

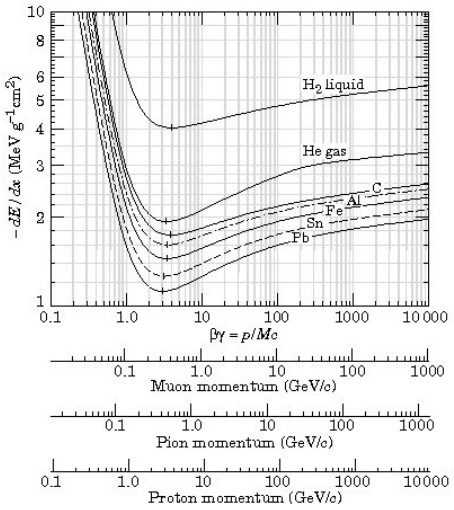

Figure 1.3: Mean energy loss rate in liquid hydrogen, gaseous helium, carbon, aluminium, iron, tin and lead. [PDG 10]

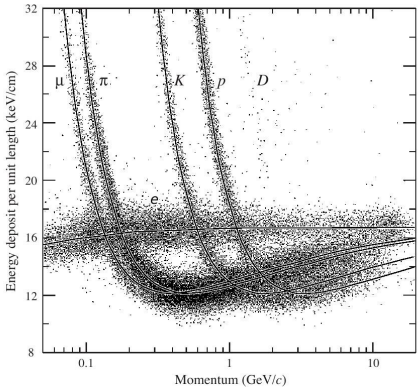

Figure 1.4: Energy deposit measurements of different incident particle in a Time Projection Chamber (TPC) filled with $Ar : CH_4$ in ratio 80 : 20 at 8.5 atm pressure [PDG 10]

Relativistic particle with $\beta\gamma \approx 4$ are called *minimum-ionizing particle* (MIP). Their energy loss corresponds to the mentioned minimum. The logarithmic term in Eq. (1.9) provides an increasing energy loss for values of $\beta\gamma \approx 5...100$. Large energy transfer per interaction is responsible for a large fraction of the rise in this energy range. These electrons, detached from the atom by large energy transfers, are called δ- *electrons* or *knock-on electrons*. The logarithmic or relativistic rise is followed by a constant plateau for $\beta\gamma \approx 500...1000$, induced by the density effect. For incident particle with higher momentum ($\beta\gamma \gg 1000$) the formula of Bethe-Bloch receives further corrections caused by radiation losses since Eq. 1.9 holds only for energy losses due to ionization and excitation.
If the incident heavy charged particle is not traveling through a pure medium but a mixture of absorber materials or chemical compounds, the average energy loss per length can be approximated by Bragg's additivity for the energy loss which is also named the *stopping power* in this context [Thwa 83]. Thus the average mass stopping power is:

$$\frac{1}{\rho}\left\langle \frac{dE}{dx} \right\rangle = \sum_i \frac{\omega_i}{\rho_i} \cdot \left\langle \frac{dE}{dx} \right\rangle_i \tag{1.10}$$

where ω_i and ρ denote the fraction and density of material i in the compound. This results from effective characteristic values of the medium, that are Z_{eff}, A_{eff}, $\ln I_{eff}$,δ_{eff} and C_{eff}, which can be directly inserted in the Bethe-Bloch formula.
The Eq. 1.9 also allows identification of particle in the low-energy region $\beta\gamma < 1$ since for a given momentum p and specified energy loss the $\beta\gamma$-value decreases for increasing mass m of the particle, following the relation:

$$\beta\gamma = \frac{p}{m \cdot c} \quad . \tag{1.11}$$

Fig. 1.4 shows how the dE/dx - curves are horizontally shifted by a factor $\left(\ln \frac{m_1}{m_2}\right)$, regarding two particle with different masses m_1 and m_2.
Of special interest in this work is the energy loss of cosmic ray muons in Ar/CO_2 gas mixed at a ratio $93/7$.

Energy Loss Distribution

The Bethe-Bloch formula gives only the average energy loss of charged particle by ionization and excitation. Introducing the parameter

$$\kappa := \frac{\langle \Delta E \rangle}{T_{max}} \tag{1.12}$$

it is possible to distinguish between thick ($\kappa > 10$) and thin ($\kappa < 10$) absorbers. For thick absorbers the energy loss can be described by a Gaussian distribution. However, in the second case large fluctuations around the average energy loss generate a strongly asymmetric energy-loss distribution (cf. Fig. 1.5).

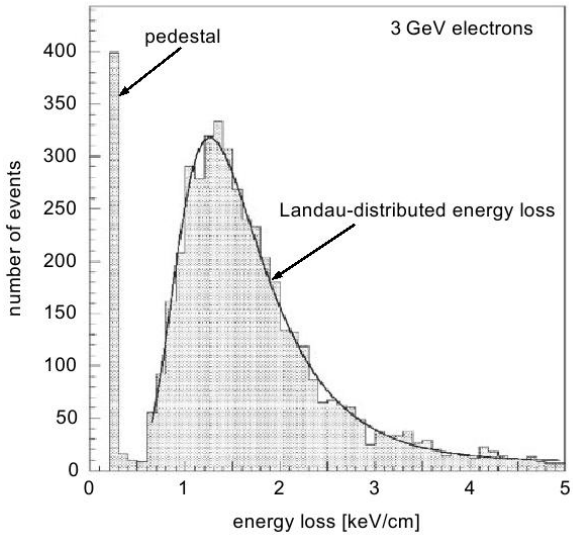

Figure 1.5: Energy-loss distribution of 3 GeV electrons in a thin-gap drift chamber filled with $Ar : CH_4$ (80 : 20) [Grup 08]

For κ <0.01 the energy loss is parametrized by the *Landau theory*. A reasonable approximation of the **Landau distribution** is:

$$L(\lambda) = \frac{1}{\sqrt{2\pi}} \cdot \exp\left[-\frac{1}{2}(\lambda + \exp^{-\lambda})\right] \tag{1.13}$$

with the characteristic parameter λ that states the deviation from the *most probable energy loss* E^W in a layer of thickness x:

$$\lambda = \frac{\Delta E - \Delta E^W}{\xi} \tag{1.14}$$

where ξ carries the characteristics of the excited or detached electron as well as the absorber material:

$$\xi = 2\pi \cdot N_A r^2 m_e c^2 z^2 \frac{Z}{A} \cdot \frac{1}{\beta^2} \rho \cdot x \tag{1.15}$$

with the same notations as in Eq. 1.9.
The tail of the Landau distribution is due to δ - electrons which absorb a big amount of energy in one interaction. Their energy spectrum and their contribution has to be included for a precise average energy loss calculation.
The charged particle of interest in this study are cosmic ray muons that lose energy in the Ar/CO_2 gas, mixed at a ration of $93/7$ in our detector. Argon and CO_2 have a density of [Groo 01]:

$$\rho_{Ar=}1.66 \text{ g/cm}^3 \quad \textit{and} \quad \rho_{CO_2} = 1.84 \text{ g/cm}^3 \tag{1.16}$$

respectively. The muon is traversing a drift volume (see Ch. 2.2) of $100 \times 100 \times 4\text{mm}^3$ to be efficiently detected. Thus we can speak of a thin absorber and their energy loss distribution can be described by this Landau distribution. This is discussed in detail in Ch. 4.3.

1.1.2 Interactions of Photons in Matter

Interactions of photons with matter differ fundamentally from the above mentioned interactions of charged particle. On the one hand, they can be absorbed in the medium by the *photoelectric effect* or by *pair production*, depending on the energy of the photon beam. On the other side, they may be scattered off into a large angle through the *Compton effect*.
Therefore, detection of photons in matter happens not directly but via charged particle, produced by the photons, when they are passing through the medium. These charged particle cause ionization which can be recorded by the sensitive volume of a detector.
Since these processes are statistical, the intensity I of the beam is rarefied after the passage through a material with thickness x, exponentially:

$$I(x) = I_0 \cdot \exp^{-\mu x} \tag{1.17}$$

where μ is the *mass attenuation coefficient* that depends on the photon-absorption cross section σ according to :

$$\mu = \sigma \cdot \rho \frac{N_A}{A} \tag{1.18}$$

Since the photo-absorption cross section σ is a function of the photon energy E_γ, the mass attenuation coefficient depends strongly on E_γ as well. In terms of the *photon absorption length* (or *mean free path*), which is defined as

$$\lambda = 1/(\mu/\rho) \quad \left[\frac{\mathrm{cm}^2}{\mathrm{g}}\right] \ , \tag{1.19}$$

the dependence on the photon's energy is shown in Fig. 1.6.

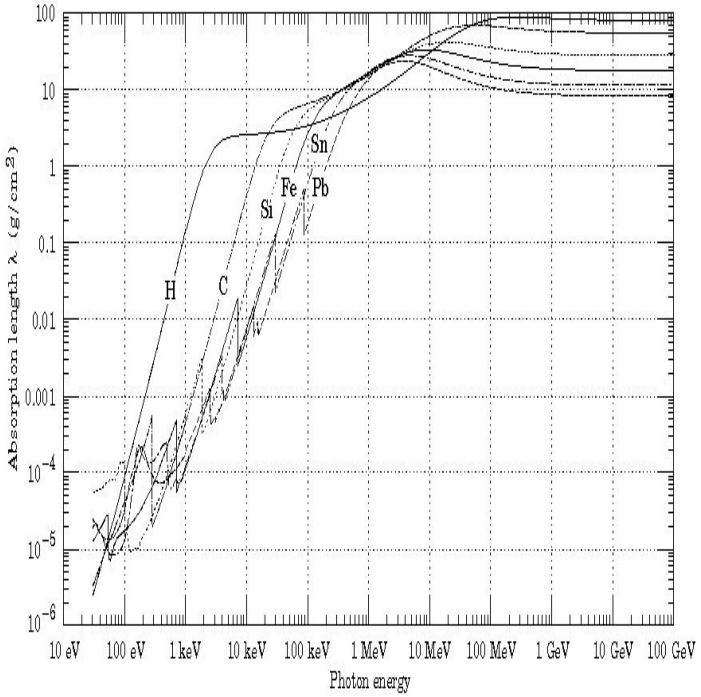

Figure 1.6: The photon absorption length for various elemental absorbers as a function of photon energy. [PDG 10].

Depending on the photons energy three different processes are responsible for the attenuation or absorption, respectively. Fig. 1.7 shows the three ranges for photons in $Ar/C0_2$ at $93/70$ ratio that is filled in the triple GEM detector.
In the range of low energies (ionization energy $\leq E_\gamma \leq \mathcal{O}(100\ \mathrm{keV})$) the photoelectric effect is dominant:

$$\gamma \ + \ atom \ \longrightarrow \ atom^+ \ + e^- \ , \tag{1.20}$$

with a squared dependence of the mass attenuation coefficient on the photons energy:

$$\mu \propto \frac{1}{E_\gamma^2} \tag{1.21}$$

For medium energies ($E_\gamma \approx 1\ MeV$) the Compton effect, which is the scattering of photons off quasi-free atomic electrons, has the largest cross section:

$$\gamma \ + \ e^- \ \longrightarrow \ \gamma \ + e^- \ , \tag{1.22}$$

where

$$\mu \propto \frac{1}{E_\gamma} \ . \tag{1.23}$$

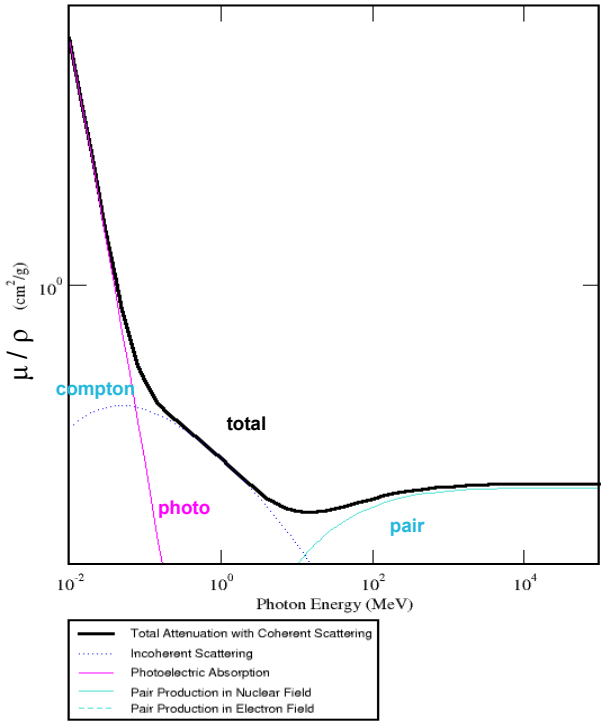

Figure 1.7: The total mass attenuation coefficient for photons in Ar/CO_2 at a ratio of 93/7 in the range of 10keV $< E_\gamma <$ 10GeV [NIST 10]. Photoelectric effect (pink), Compton scattering (blue dotted) and pair production (blue straight line) summarize to the black envelope.

Photons with higher energies ($E_\gamma \gg 1\ MeV$) are dominantly absorbed by the nucleus for pair production:

$$\gamma \ + \ nucleus \ \longrightarrow \ e^+ + e^- \ + \ nucleus, \tag{1.24}$$

with

$$\mu \propto \text{const}(E_\gamma) \ . \tag{1.25}$$

Due to momentum conservation the absorption of a photon by an atomic electron needs a third collision partner which takes the recoil momentum, in this case the atomic nucleus. In the vicinity of the nucleus, that is in the K shell, the cross section for absorption of a photon carrying energy E_γ is about 80 % of the total cross section. If the photon energy lies above the K shell binding energy E_K the total photoelectric cross section is given in the *Born approximation* by

$$\sigma_\gamma \approx \frac{32\pi}{3} \cdot \sqrt{2} \cdot Z^5 \alpha^4 \cdot r_e^2 \cdot \left(\frac{m_e c^2}{E_\gamma} \right)^2 \tag{1.26}$$

with $E_K < E_\gamma < m_e c^2$.

Photoelectric Effect for ^{55}Fe

For measurements with the GEM detector later presented, see Ch. 3, a ^{55}Fe source is used to analyze certain properties of the chamber.
^{55}Fe decays by electron capture to excited Manganese ^{55}Mn which emits photons by returning into the ground state. Depending on the inner rearrangement of the electrons, two different photon energies are characteristic. The K_α photon which represents the transition of an electron from the L to the K shell, carries an energy of $E_\gamma = 5.90$keV.
If the ^{55}Mn atom returns to its ground state via M-to-K transition of an electron, a K_β- photon is emitted with an energy of $E_\gamma = 6.50$keV.
The line intensity proportion for K_α and K_β is 24.4% and 2.86%, respectively, the K_α process dominates over K_β by approximately 10 : 1 [PDG 10].

When these photons are interacting with the $Argon/C0_2$ gaseous filling of the GEM detector, the photoelectric effect is the dominating process .

The K_α- photon energy is higher than the binding energy or an electron from the K shell of Argon ($E_K = 3.22$keV). The electron can detach with a remaining kinetic energy of 2.68 keV. The excited Argon atom then returns to its ground state through emission of one ore more photons that leave the volume without being detected.

The resulting X-ray spectrum consists of three line with the energies: 2.68 keV, 5.90 and 6.50 keV.
By photoelectric effect the X-ray energy is transferred to an electron in the active volume of the detector. Recording of this spectrum with the triple GEM detector can be used to state the energy resolution of the device and is illustrated in Ch. 4.1.
Since excitation dominates over ionization for statistical reasons, the required energy loss for an ionization is greater than the simple ionization potential. Therefore the total number n_t of ionized particle is:

$$n_t = \frac{1}{W_i}\frac{dE}{dx} \tag{1.27}$$

where (dE/dx) is the energy loss of the incident particle and W_i represents the average energy required for the production of an ion-electron pair. For Argon the mean energy for ion-electron-pair creation is $W_i = 26$ eV which is nearly a factor two larger than the simple ionization potential of 15.8 eV.
Since the gas used in the GEM detector is not purely mono atomic Argon but a mixture of Ar/CO_2 in the ratio $93/7$, average values for W_i should be taken. With the given mean energy for ion-electron creation for Argon and CO_2

$$W_i^{Ar} = 26 \text{ eV and } W_i^{CO_2} = 33 \text{ eV} ,$$

the gas mixture has a value of:

$$W_i^{gas} = 0.93 \cdot W_i^{Ar} + 0.07 \cdot W_i^{CO_2} = 26.50 \text{ eV} , \tag{1.28}$$

as lower limit for ion-electron pair production. Thus the average number of ionized atoms generated by the ^{55}Fe photon is:

$$n_t = \frac{5.90 \cdot 10^3 \text{ eV}}{26.50 \text{ eV}} \approx 223. \tag{1.29}$$

1.2 Free Charges in Gases

For further studies it is of interest how these ions and electrons, either produced by ionizing photons or muons move in the gas filled active detector volume.

1.2.1 Diffusion

If there is no electric field applied to the gaseous volume, the produced charges will lose their kinetic energy quickly, since they are colliding with the nearby gas atoms and molecules. Corresponding to the temperature of the gas, the charges will assume the average thermal energy distribution. Thus the produced ionization, formerly locally distributed, diffuses due to multiple collisions, corresponding to a Gaussian distribution:

$$\frac{dN}{N} = \frac{1}{\sqrt{4\pi Dt}} \cdot \exp\left(-\frac{x^2}{4Dt}\right) dx \tag{1.30}$$

where $\frac{dN}{N}$ states the portion of charges which will be diffused in the length element dx at a distance x and after a time t. D stands for the *diffusion coefficient* and characterizes the width σ_x of the distribution:

$$\sigma_x = \sqrt{2Dt} \quad \text{and} \quad \sigma_V = \sqrt{6Dt} \tag{1.31}$$

for the linear case and a volume diffusion respectively. The diffusion coefficient D can be calculated by means of the kinetic gas theory which leads to the following explicit form:

$$D = \frac{2}{3\sqrt{\pi}} \cdot \frac{1}{p \cdot \sigma_0} \cdot \sqrt{\frac{(kT)^3}{m}} \tag{1.32}$$

where σ_0 denotes the total cross section of a charge for a collision with a gas molecule, p is the pressure, m the mass and T the temperature of the gas.
The diffusion coefficient of Argon-ions in Argon D^+ is $0.04\frac{cm^2}{s}$ which corresponds to a classical mean free path of $1.0 \cdot 10^{-5}$cm.
Whereas the diffusion coefficient D^- for electrons lies in the range of $250\frac{cm^2}{s}$ with a classical mean free path that is four times longer compared to that of ions. The effect of diffusion becomes important at the point of spatial resolution of the detector since position and size of the charge cloud are affected by the above mentioned process.

1.2.2 Recombination and Attachment

The number of particle produced by an ionizing electron-ion pair is an indicator for the energy deposited. It is important to separate these pairs as quickly as possible so that their number can not be reduced significantly by *recombination* and *electron attachment*. A fast separation is achieved by applying a high drift field ($E_{drift} > 100$ V/cm) and small drift gaps.

The rate of recombination dn depends on the concentration of positive n^+ and negative n^- particle in the gas:

$$dn = -\text{const}\, n^+ \cdot n^- \cdot dt \tag{1.33}$$

involving a constant defined by the gas.

Certain impurities in the gas volume, as O_2, Cl_2 or water are able to capture electrons, since they have outer shells, which are nearly fully occupied (so-called *electron affinity*). This effect may keep electrons from reaching the readout to be detected. For instance, a pollution of 1 % air in Argon and a drift fields of 500 V/cm leads to a removal of about 33% of the liberated electrons per cm drift [Saul 77].

1.2.3 Drift of Ions and Electrons

Applying an electric field to the active detector volume leads to acceleration of free charges and gives rise to drift velocity. The proportional constant between the field E and the mean *drift velocity* v_D of the charged particle is called *mobility* μ :

$$\mathrm{v}_D = \mu \cdot E \cdot \frac{p_0}{p} \tag{1.34}$$

where p is the gaseous pressure and p_0 the standard pressure of 1013 mbar. The mobility of ions is typically smaller than that of electrons. Explicitly:

Gas	Ion	mobility μ $\left[\frac{\mathrm{cm}^2}{\mathrm{V\ s}}\right]$
Ar	Ar^+	1.7
CO_2	CO_2^+	1.09
Ar	CO_2^+	1.72

Table 1.1: Mobility of ions in Argon and CO_2. Argon-ions in CO_2 gas are not reported by the literature.

The mobility of electrons is about 100 to 1000 times higher than of ions. The greater mean free path λ enables the electrons, differently to ions, to gain considerably energy between collisions with the gas molecules. In an electric field, electrons reach energies of some eV which leads to a *de-Broglie* wave length of the size comparable to the atomic diameter. Quantum mechanical effects result in a cross section σ for the electrons that strongly depends on their kinetic energy and therefore also depending on the free path λ, since $\lambda \propto 1/\sigma$. This behavior is sketched in Fig. 1.8 for the cross section of electrons in Argon as a function of their kinetic energy. The characteristic minimum is called *Ramsauer minimum*.

The electron drift in gases is described in [Bieb 08] and [Grup 08] where the drift velocity v_D is approximated in terms of the electric field:

$$\mathrm{v}_D \approx \sqrt{\frac{2}{3}\sqrt{\frac{\Delta E_{kin}}{3}} \cdot \frac{eE}{m} \cdot \lambda_e} \tag{1.35}$$

where ΔE_{kin} is the fraction of energy transferred to the gas molecule during collision with the electron. For the electric fields used in the GEM detector (typically $1.0...2.0(\mathrm{kV/cm})$) in an Ar/CO_2 mixture in the ration $93/7$, the drift velocity is about $4\ \mathrm{cm}/\mu\mathrm{s}$.

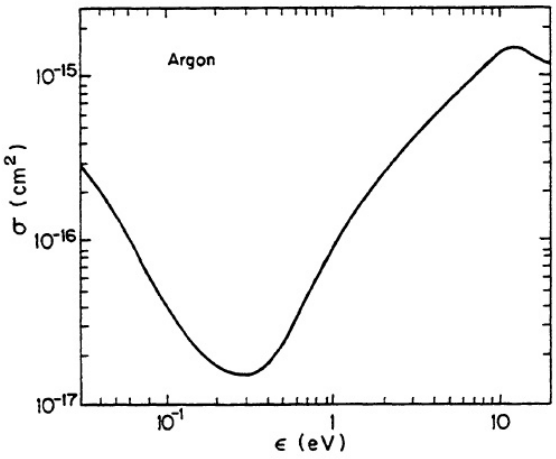

Figure 1.8: Elastic cross section with *Ramsauer minimum* for electrons in Argon as a function of the electron's energy. [Saul 77]

1.2.4 Gas Amplification

In order to readout the total charge created by primary ionization, the amount has to be multiplied, since it is usually too small to be detected. This feature makes the *gas amplification* to the key principle in gaseous detectors.

Applying high electric fields accelerates the electrons along the field lines and they gain enough energy between two collisions to ionize other gas molecules, whose liberated electron also gains energy in the field to ionize more molecules and so on. This avalanche of ions and electrons has drop-like shape, due to the difference in the drift velocity and the diffusion of migrating charges in the gas (cf. Fig. 1.9). One of the most important properties of a gaseous detector is the one associated with the gas amplification, the so-called *gas gain G* and is defined as:

$$G = \left(\frac{n(x)}{n_0}\right) = \mathrm{e}^{\alpha x} \tag{1.36}$$

with n_0 and $n(x)$ the number of ion-electron pairs before and after an amplification along the path x. The total number of ionized electrons generated by one primary electron per unit length of drift is called *first Townsend coefficient* α. The exponential rise of liberated charge is only valid as long as recombination and attachment are negligible and no ionization due to UV-photons takes place. The multiplication factor cannot be increased in any order. The *Raether* condition gives a phenomenological limit for the gas amplification:

$$\alpha x \approx 20 \quad \text{or} \quad G \approx 10^8. \tag{1.37}$$

From Eq. 1.37 it is obvious that for increasing path length, i.e. gap thickness in the GEM detector (cf. Ch. 3), the Raether limit will be met at decreasing values of α. Therefore the breakdown probability increases for a given field strength with the gap size. The Townsend coefficient, normalized to the applied pressure, for Ar/CO_2 mixtures in several percentages can be seen in Fig. 1.10.

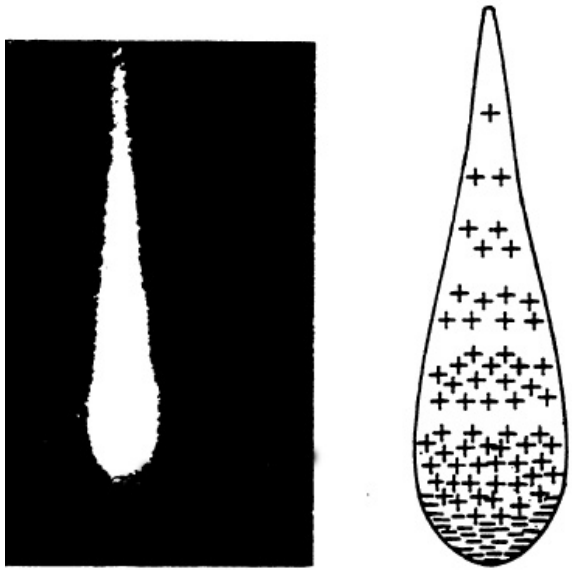

Figure 1.9: Drop-like shaped avalanche due to gas amplification. The photo on the left is recorded in a cloud chamber. [Saul 77]

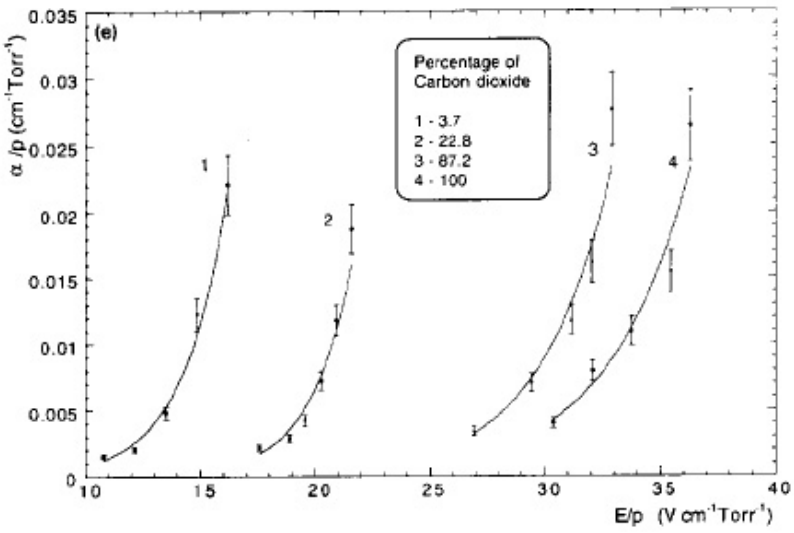

Figure 1.10: First Townsend coefficient α/p as a function of the reduced electric field E/p. [Shar 93]

Chapter 2

The GEM Principle

*In 1997 F. Sauli suggested the **G**as **E**lectron **M**ultiplier foil [Saul 97] which is the device responsible for charge amplification in the gaseous active area of the correspondent GEM detector. This chapter illustrates the manufacturing and design of the foils and their operation in a detector.*

2.1 Manufacturing and Design

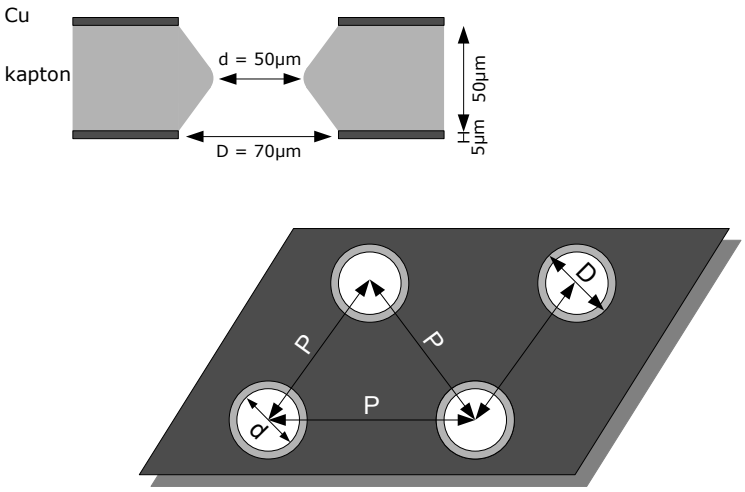

Figure 2.1: Dimensions of a standard conical designed GEM (CERN)

The GEM foil consists of an insulating polymer foil, mostly kapton, which is metal-coated on both sides. In a chemical etching process[1] a periodic geometry of holes is etched into this composite sheet. In the first step, the hole structure is etched only into the metal planes. To avoid slanted holes, the perfect alignment of the two etching masks with each other is fundamental [Altu 02]. The perforated copper planes serve as a mask for the second process of etching with Ethylendiamin, an etching solution that only solves the polymer foil. Since the etching is done from both sides, the holes have

[1]Fabrication Technology was developed by R. De Oliveira, A Gandi and L. Mastrostefano (CERN Surface Treatment Service)

double-conical shape (see Fig. 2.1). This shape is a compromise due to research results, as a non-realizable cylindrical shape should be preferred [Benl 98] to keep the walls from charging-up. Due to irregularities in the material, local defects or even total removal of the kapton layer may occur after an etching process for cylindrical holes [Altu 02]. The double-conical geometry was introduced to improve the dielectric rigidity and also to prevent shortcuts between the upper and lower copper cladded side of the foil under operation at e.g. $\Delta U_{gem} \approx 350$ V.
A typical GEM foil, or shortly GEM, as it is designed by the CERN workshop, consists of a 50 μm kapton layer covered on both sides by 5 μm thick copper films. Since the holes are double-conically shaped, one can define two diameters, see Fig. 2.1. The inner diameter in kapton is about 50 μm and the outer one in copper about 70 μm, with a center-to-center distance of 140 μm [Saul 97] and [Bij 05].
The ratio of material liberated area to total area of the foil is defined by the *optical transparency* [Simo 01]

$$\tau = \frac{\text{perforated area}}{\text{unit cell}} = \frac{\pi \left(\frac{d}{2}\right)^2}{\frac{\sqrt{3}}{2} \cdot P^2} = \frac{2}{\sqrt{3}} \cdot \pi \left(\frac{d}{P}\right)^2 \tag{2.1}$$

where d is the inner diameter and P the pitch of the holes as denoted in Fig. 2.1. The GEMs used here provide a $\tau \approx 0.46$. Fig. 2.2 presents a microscopic view of such a foil.

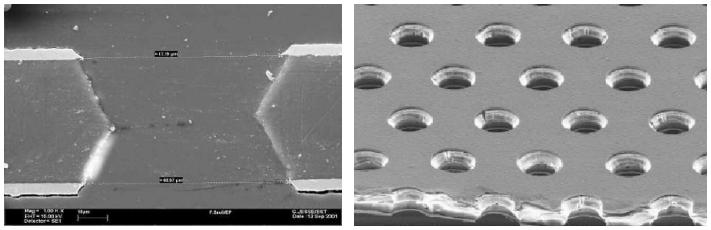

Figure 2.2: Microscopic pictures of the GEM foil. On the left the cross-section of a hole [Altu 02]. Size of holes and pitch are 70 μm and 140 μm, respectively [Saul 03].

2.2 The GEM Foil Principle

Applying high voltage to the GEM's copper electrodes generates an electric field inside the holes as high as 55 kV/cm, for a given voltage difference of $\Delta U_{GEM} = 350V$. Placed in an appropriate gas-filled environment, this field is able to provide energies for the electrons that are high enough for gas amplification. The simplest way to build a particle detector including a GEM foil is by inserting the foil in a parallel plate electric field, generated by a drift electrode and a charge collection anode (cf. Fig. 2.3).

Electron-ion pairs, created by a traversing ionizing particle, are separated in the electric field of the upper *drift gap*. As shown in Fig. 2.3, the electrons drift towards the holes, where they undergo gas amplification, due to the high field in the GEM. The multiplied charge is guided by the field lines into the so-called *induction region* to the anode structure, from where it can be readout.

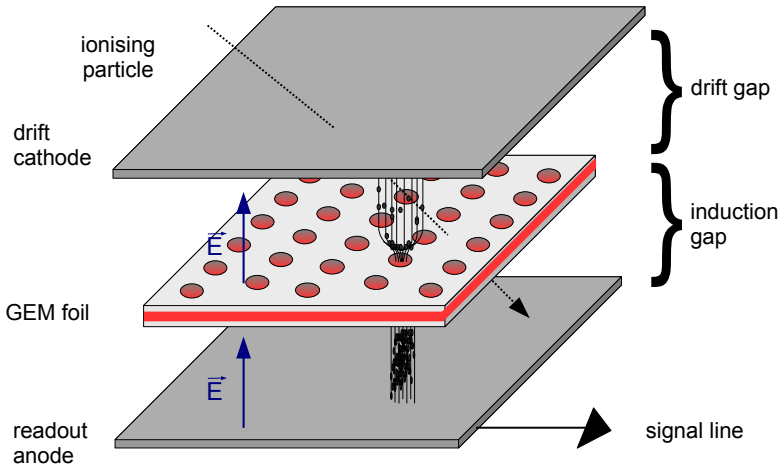

Figure 2.3: Schematics of the operation principle of a single GEM detector. Primary electrons drift in the *drift gap* towards the GEM. After amplification the negative charges cross the *induction gap* to be collected by the readout anode.

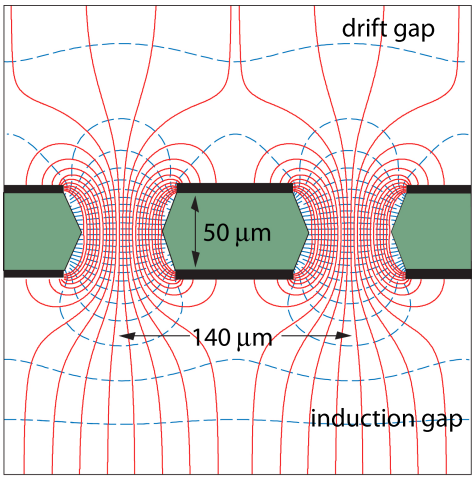

Figure 2.4: Schematic view of the field configuration in the GEM holes. The electric field (solid lines) and corresponding equipotenital lines (dashed) are computed by the *MAXWELL* simulation program [PDG 10].

It depends on the strength of the electric fields how many of the primary produced electrons from the upper region are passing the holes and reach the charge collection anode (see Fig. 2.4). In an optimal setup, most of the electrons from the *drift region* travel to the foil and leave it after gas amplification towards the *induction gap* and the anode. The fraction of negative charges from the drift region that effectively reaches the amplification zone in the GEM foil is the so-called *electron transparency* [Weit 03].
On the other hand, the primary ions drift along the field lines above the foil to the cathode without affecting significantly the electron signal at the readout structure. More important are the ions from the amplification area in the holes of the GEM since they may modify the electric field. As the

mobility of ions is about hundred to thousand times smaller than for electrons, the former stay along the field lines and are collected by the top electrode of the foil. In an optimal process they will reach neither the drift nor the induction gap. In reality there may be a fraction of ions which escape into the gap regions resulting in an induced current at the cathode. This defines the *ion feedback* to be the ratio of induced charges at the drift electrode owing to ions and the desired induced signal caused by electrons at the anode [Simo 01]. In this way space charge effects are reduced to a minimum. On account of this ion suppression that results in an achievable excellent spatial resolution, GEMs are used in a wide range of implementations from particle physics over astrophysics to medical applications [Saul 03].

2.3 Multiple GEMs

Multiple GEM detectors are already used in several experimental setups. For instance, a lot of research on GEM detectors was done for the COMPASS[2] experiment at CERN since they represent an important fraction of the installed tracking devices. This detector investigates hadron structure and hadron spectroscopy by running in high intensity muon and hadron beams [Ketz 04] and [Ketz 03].

Discharges that may occur inside a GEM foil or even propagating all the way from the GEM electrode to the readout structure are a serious concern. Initiated by heavily ionizing particle, these local currents cause a voltage breakdown that may result in destruction of detector material or readout devices.
In order to attain detectable amounts of charges for the readout, one can multiply the effect of the GEM by using several GEM foils in a stack. In such an assembly, the uppermost GEM acts as an amplifying stage for the subsequent foils, increasing the overall gas gain to the power of installed GEMs. For instance, in view of a triple GEM configuration and a given gain $G \approx 20$ per foil, the total primary charge is amplified by a factor of $20^3 = 8000$ [Murt 02], depending on the applied voltages and used gas mixture.

The performance of GEM detectors in high irradiation environment and the corresponding discharge probability is studied intensely by Bachmann et al., for instance in [Bach 01a] and [Bach 01b]. Measurements with single and multiple GEM foils in a detector under alpha particle irradiation indicate that for a given gain the discharge probability reduces the most for a setup of three GEM foils [Bach 02]. Fig. 2.5 shows how the effective gain of a particular GEM detector increases by approximately an order of magnitude per added foil without affecting the discharge probability significantly. By considering a desired gain of $G = 4000$ the double GEM structure reports a discharge probability of 0.09×10^{-2} which corresponds to an already serious rate. Taking triple GEM detector decreases the discharge probability under the measurable limit of 6×10^{-6} .

These results are based on data taken for detectors filled with Ar/CO_2 at a ratio of $70/30$ and with ^{241}Am as an irradiation source that provided collimated α-particles at a frequency of approximately 100 Hz. The electric fields applied in a multiple GEM detector can be decreased in comparison to single GEM detectors by still reaching higher and safe gain. Additionally it was found that the total gain can be further increased by cascading the voltage across the foils with the uppermost foil at the highest voltage difference (see Ch. 3.2). Although the gas volume of the detector has to be

[2] **CO**mmon **M**uon and **P**roton **A**pparatus for **S**tructure and **S**pectroscopy

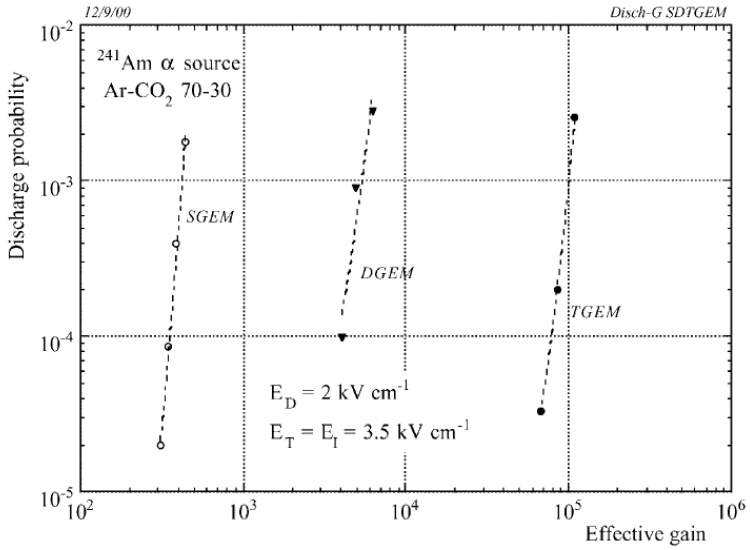

Figure 2.5: Discharge probability as a function of effective gain for single, double and triple GEM detectors [Bach 02].

enlarged for housing three foils, the triple GEM structure proofs to be the optimal candidate for the just mentioned reasons.

As a consequence, a triple GEM configuration is chosen for this work. In contrast to triple GEM detectors as they are implemented in COMPASS, for instance, we chose the GEM foils to be located 3 *mm* distant to each other and we chose a drift gap of 4 *mm*. Implementation of this assembly means a 25% wider induction region as well as a 33% broader drift gap. These dimensions were taken for the first triple GEM detector, "prototype 1.0", as they provide stable operation parameters. In the upcoming Ch. 3.1 a detailed report on the implementation of the triple GEM will be given. The standard dimensions in terms of foil-to-foil and foil-to-cathode/anode distances are implemented in later designed detectors, referred to as "prototype 2.0".

Chapter 3

The Triple GEM Prototype 1.0

The first prototype has been built with the intention of learning about development and commissioning of such a detector from the very beginning. Since most measurement and most analyses of this work are done with the "prototype 1.0", this chapter will emphasize its commissioning in detail. A second and third prototype ("GEM prototype 2.0") with the aim of high resolution position tracking are implemented and documented in Ch. 8.

3.1 Assembly of the Triple GEM Detector

This section documents the setup of the detector and describes in detail its materials and dimensions.

3.1.1 The Stack

Framed Foils

As mentioned in the previous Ch. 2, GEM foils with CERN standard geometry were chosen for the gas amplification. The foils are delivered by CERN already glued on supporting fiberglass frames, surrounding an active area of $(100 \times 100)\ mm^2$ (see Fig. 3.1). Dimensions can be found in Fig. B.1.

During preparations it was ascertained that the used GEM foils could not be operated at the limit documented by CERN, namely a breakdown voltage of $\Delta U_{GEM} = 650$ V and a leakage current of less than 10 nA at 600 V. Depending on the individual foil, the breakdown voltage is in the range of 300...400 V in a gas filled environment of Ar/CO_2 at the ratio $93/7$.
Although it is possible to "train" the foils by gradually increasing the voltage and stopping at each step for some time, no higher field than the above mentioned could be achieved. Washing the GEMs in alcohol and drying them in the clean room ensured the quality after long storage and was mandatory to gain a stable operation of the foils.

In order to bring the GEMs to the right position and distance in the detector, thread rods are installed at each of the corners. Spacer on the rods and spacer glued in the middle on every frame's flank are stabilizing the stack which is shown in Fig. 3.2. The whole mounting has to be done under clean room conditions. The handling with gloves and facial mask prevents (re-)contamination of the foils, since any impurity on the foil could lead to shorts [Saul 04].

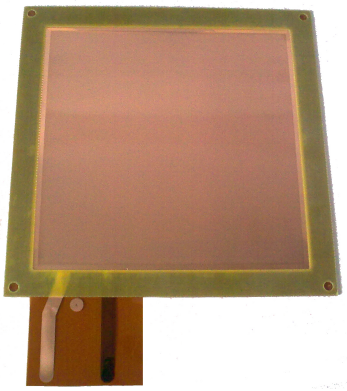

Figure 3.1: Framed GEM foil of $(100 \times 100)mm^2$ active area, as it is produced and delivered by CERN.

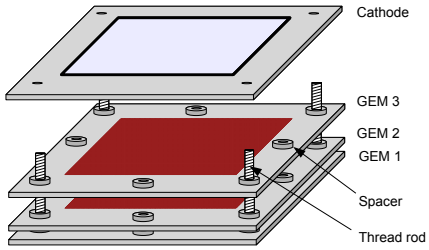

Figure 3.2: Exploded view of the triple GEM stack with spacers and drift cathode.

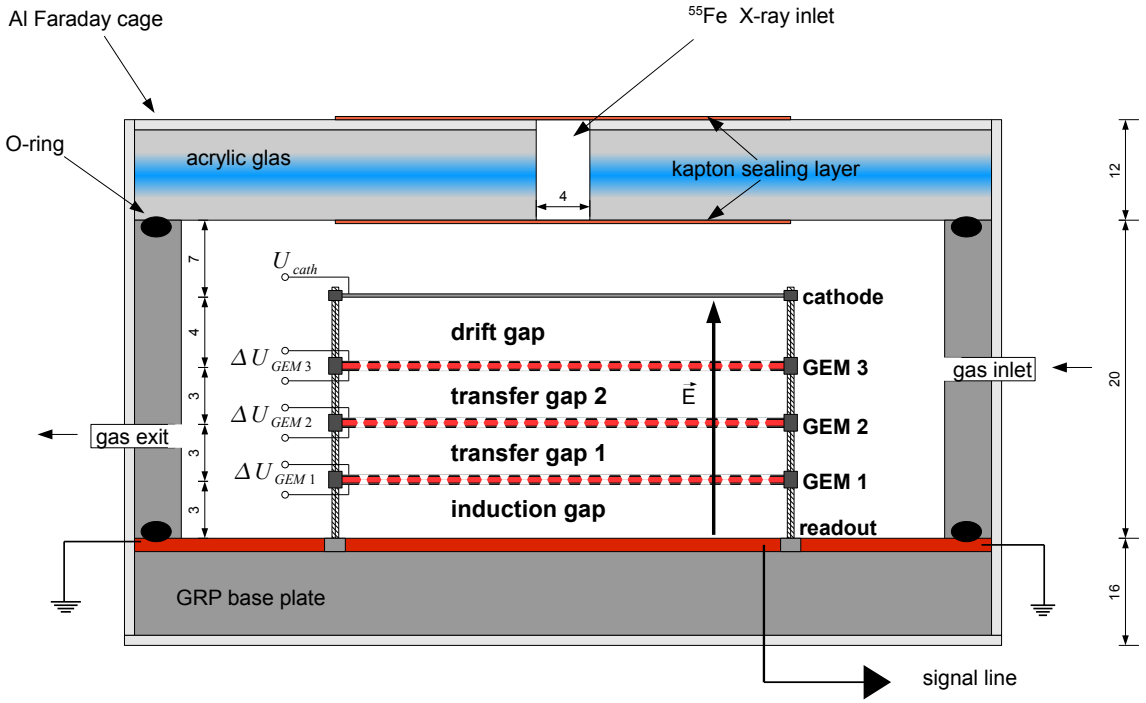

Figure 3.3: Schematic profile of the triple GEM detector. Dimensions are given in mm. Drawing not to scale.

The Cathode

The cathode is made of a $36\mu m$ thick aluminum covered *mylar* foil, basically a metalized boPET[1] film, that warrants good electric properties with respect to high voltage as well as high stability and strength. The film is glued with epoxy on a 2 mm thick aluminum supporting frame which holds the same dimension as the fiberglass frames of the GEMs.

The Anode

An unsegmented 1.6 mm thick copper-clad PCB with $(210 \times 300)mm^2$ base area, to suit the housing dimensions, was chosen for the first measurements. The anode area of $(115 \times 155)mm^2$ is separated from the surrounding grounded copper top and bottom layer (cf. Fig. B.2). The collected charge is read out via a broad strip of 22 *mm* that is connected to the preamplifier and thus to the following electronics.
For a further step of measurements, we implemented a fivefold segmented PCB[2] anode, with same dimensions but an active area of $(100 \times 104)mm^2$, divided into five equal strips of $(100 \times 20)mm^2$ separated by 1 mm insulation length, see Fig.B.3, also surrounded by grounded top and back planes.

3.1.2 The Complete Housing

A schematic profile of the detector is provided in Fig. 3.3.
The gas volume of $(170 \times 240 \times 20)mm^3 = 0.82$ l is enclosed by a bottom plate and a frame made of GRP[3]. The top plate is made of acrylic glass for optical control possibility. O-rings between frame and PCB anode, which is mounted on the bottom plate, and between frame and top plate ensure the hermetic sealing of the volume. The gas is supplied to the detector volume via gas feeds on two sides of the frame. As Fig. 3.4 shows, there are also divider walls placed in the detector, guiding the gas flow through the active area, i.e. the triple GEM stack. Furthermore, seven drills are made for HV supply of the cathode and six GEM electrodes, placed on the right side in Fig. 3.4, oppositely to the readout side.

To reduce noise, the whole detector is covered by a 2 mm thick Faraday cage and an additional conductive copper tape.

For measurements with an ^{55}Fe irradiation source (cf. Ch. 4, Ch. 6 and Ch. 7), five holes, centered to the active area of the triple GEM detector, are installed in the top plate and sealed with kapton layers (see Fig. 4.6).

3.2 HV Supply

Seven different voltages are needed to generate the high potentials on the GEM foils and the gaps. Fig. 3.6 shows an exemplary setup of voltages for the configuration. Decoupling capacitors are not implemented in the current setup since they were not needed.

[1] Biaxially-oriented polyethylene terephthalate, a polyester film that is produced by stretched PET
[2] **P**rinted **C**ircuit **B**oard
[3] **G**lass **R**einforced **P**lastic

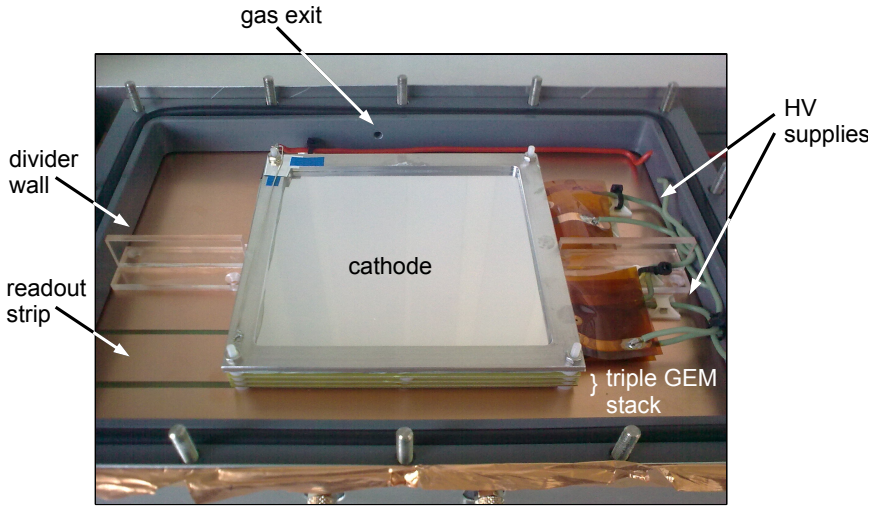

Figure 3.4: Inside view of the prototype 1.0 with unsegmented copper anode. The connection straps of the GEM foils to HV supply are visible on the right.

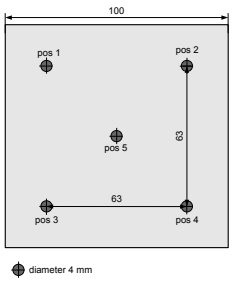

Figure 3.5: Schematic view of the cover plate with ^{55}Fe X-ray inlets.

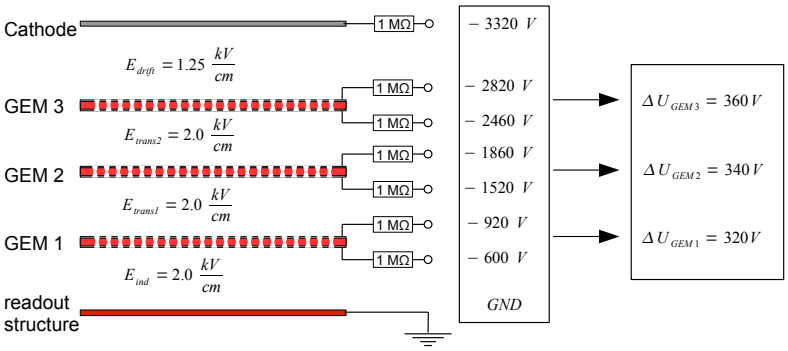

Figure 3.6: Loading resistors and exemplary set of applied voltages for the triple GEM detector.

Four computer controlled dual channel HV power supplies [iseg 01] are used. These devices are equipped with a RS232 interface to control and monitor the actual voltages and currents. To the programs for communication with the device and to cope with the interface's hardware settings is referred in App. D.1. The program checks every 30 seconds if a discharge occurred in the detector. This is enabled by the hardware current limit which is set to a few nA. Any current between the

copper-cladded sides of one foil which rises higher than a few nA results in a shutdown of the high voltage supply. With this procedure, an essential tool is implemented to avoid damage on the foils, due to (continuous) discharges. At the latest 30 seconds after a trip of the HV supply is recognized by the control code, an entry with time stamp and name of the tripped foil(s) is added to the output file, followed by the gradually re-increasing of the voltages to the operation value. The potentials on the GEM foils are not identical in the exemplary configuration of Fig. 3.6, but slightly increase from first to last GEM, since it was experienced that discharge rates can be minimized this way (compare Ch. 2.3 and [Bach 02]).

3.3 The Gas System

3.3.1 Benefits of Noble Gases - The Gas Choice

In general, there are no exclusions on the choice of gas or gas mixture for the operation of any gaseous detector. Since the initiation of gas amplification of a corresponding gas depends on the kinetic energy of the incident particle, the high voltage limit of the suppling device is the only constraint, theoretically.
However, a main point in the considerations for a detector are low working voltages, as they directly affect the design and material constraints. Furthermore, one should think of a short dead time or the capability of high particle rates, as it is also a motivation for this triple GEM detector.

Looking for gas amplification at low electric field, noble gases are the best candidates, due to their shell configuration. For the desired detection of MIPs in the drift region of the detector, one needs a specific minimal amount of ionized gas particle, that increases with the atomic number of the corresponding gas. Since the noble gases Krypton and Xenon are among the rarest elements on earth and therefore extremely expensive, Argon is the filling gas, chosen for the GEM detector, as for many other gaseous detectors.

Due to primary ionization in the drift region and gas amplification inside the GEMs, the gas volume is filled with ions and excited atoms, that are not collected by the readout structure. Ions are guided on the field lines to neutralize at the GEMs surfaces or the cathode, maybe followed by the emission of a photon. The gas atoms descend to their ground state by either emitting an electron from an inner shell (*Auger effect*, see Ch.1.1.2) or by emission of another photon. Taking into account that the minimum energy of these photons is $E_{\gamma}^{Ar} = 11.6$ eV and therefore higher than the ionizing potential of copper ($E_{ion}^{Cu} = 7.7$ eV), they may hit metal-clad surfaces in the detector and release new electrons which may undergo amplification processes as well. To prevent these “wrong” electrons from being detected and added to the real signal, one applies so-called *quencher* gases to the detector volume. They consist of polyatomic molecules and are inserted to absorb the trouble causing photons before reaching any surface and displace their energy in rotation and vibration modes [Saul 77]. In our case CO_2 was used which is a neither flammable nor a polymerizing molecular gas.
We chose to operate the triple GEM detector with a mixture of Ar/CO_2 at a ratio of $93/7$.
The properties of this mixture are well understood and studied for long time in our group, as it is the gas mixture, chosen for the Monitored Drift Tube detectors at ATLAS. Intense studies on these gas filled tubes were done at the Cosmic Ray Measurement Facility in Munich, see [Bieb 03] and [Engl 09] for detailed discussion.

3.3.2 Gas Supply System

In the test stand assembly, a pre-mixed gas at a ratio of $93/7$ is supplied to the detector via 3 mm thick gas feeds. Two gas inlets are placed centrally with respect to the active detector area as can be seen in Fig. 3.7, showing the whole detector setup. First measurements were done using the pressure regulator on the gas bottle and a needle valve for pressure control. To guarantee more stable operation conditions for further measurements, a flow and pressure control unit was implemented between the detector and the gas supply, as can been seen in Fig. 3.8.

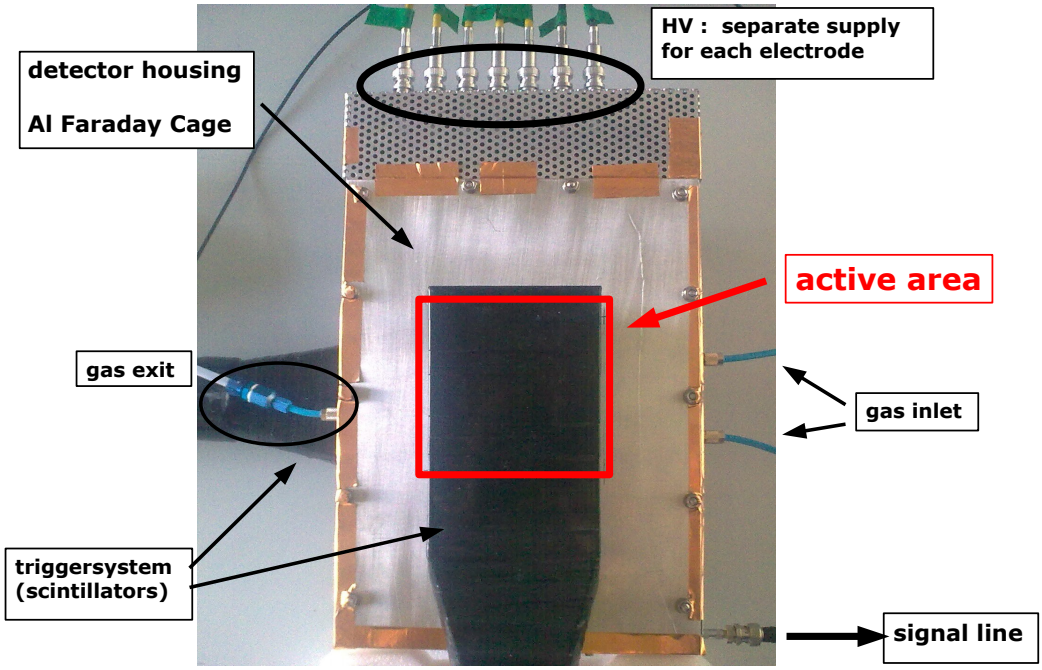

Figure 3.7: Top view of the closed prototype 1.0 triple GEM detector with connections to HV supply, gas system and readout electronics. Trigger units are positioned above and beneath.

The mass flow controller (*BROOKS 5850S*), installed in the gas line between bottle and detector, is adjusted to a constant gas flow of $0.900 ln/h$, which is implemented with the flow computer *WMR 4000*. A (*MKS Baratron*®) is used to monitor the pressure at the exit line. In case the pressure deviates from the nominal value, an electronically controlled regulation valve corrects for it. It was found that, due to internal problems of the pressure control unit, the pressure could be stabilized only in the range of ± 10 mbar. It was decided to regulate the detector's pressure to a mean value of 1020 mbar, keeping it independent of atmospheric influences.

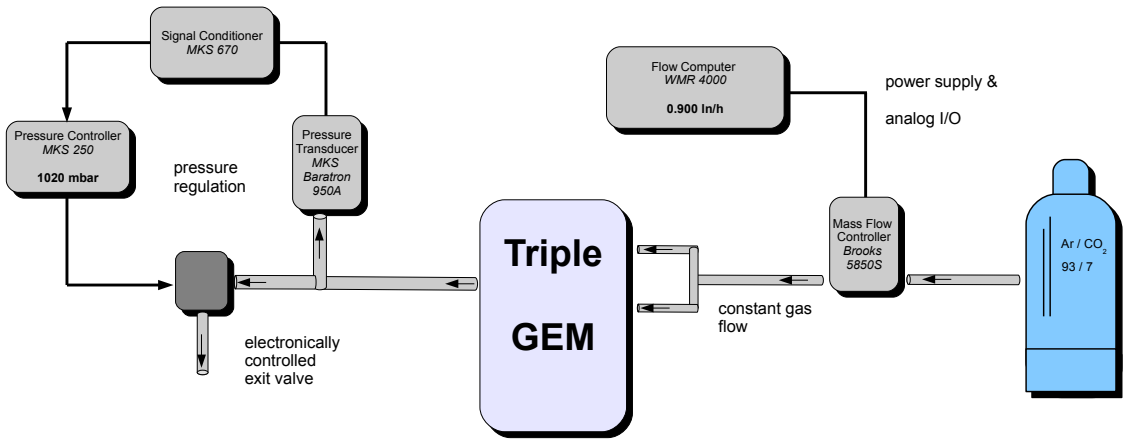

Figure 3.8: Schematic setup of the gas system.

3.4 Flash ADC Readout

Ionizing particle create electron-ion pairs in the detector volume as explained in the previous chapter. In this section it is illuminated how the amplified charges are processed electronically.

3.4.1 Readout Chain

The charges, reaching the anode structure of the triple GEM detetctor, are read out via charge sensitive preamplifier.
For the first measurements, a charge and time sensitive preamplifier, *CATSA82*, was used [Tran 87]. Later on, a *Canberra2004* [CANB 07] and a preamplifier home-built by the Electronics Laboratory of the LMU Munich (*ELab*) [Karg 10], were also implemented. The Canberra preamplifier is originally produced for semiconductor-detectors but also suits micro-structured gaseous detectors.

The electronic readout is given in Fig. 3.9. The amplified analog signal splits into two lines. The pulse is translated to a digital output by the VME flash analog-to-digital converter (FADC) [CAEN 10] allowing for data storage and further analysis. The FADC records a range of 12 bit, at an acceptance of ± 0.5 V, and 1 GHz sampling frequency. With its 2520 ns sampling time, the typical signal's risetime of about 100 ns can be easily covered by the FADC. The communication with the flash ADC is ensured with an *SIS3150* USB-to-VME interface by *Struck*.

On the second line, the preamplifier's signal is feed to a timing filter amplifier (TFA), developed by the ELab[4], with an integration time of 200 ns and a course gain of 20. Followed by a *CAEN N845* discriminator and stretched to a $1\mu s$ long pulse in the *CAEN N93B timer*, this NIM[5] signal is used as first trigger line, as it is exploited for measurements with a ^{55}Fe-source. In order to avoid crashes of the VME FADC by receiving new triggers while still processing the last signal, the trigger line is connected to the FADC via a second timer, that creates a theoretically infinitely long NIM pulse. After the FADC has completed a readout cycle, the input-output register (I/O Register) in the VME

[4] **E**lectronic **Lab**oratory of the LMU Munich, Garching
[5] **N**uclear **I**nstrumentation **M**odul Standard

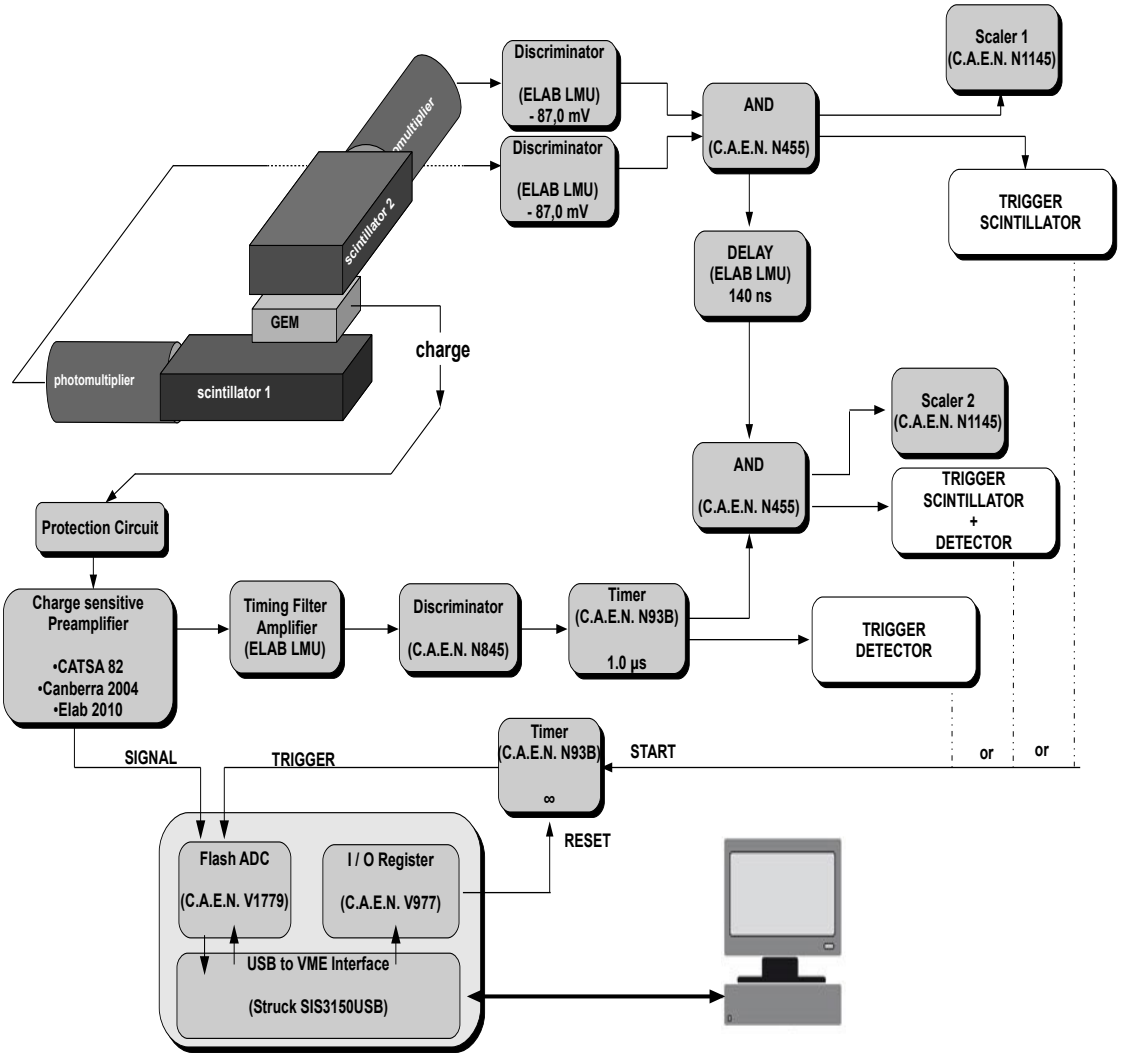

Figure 3.9: Schematics of the readout chain with Flash ADC, trigger and signal lines.

unit resets the timer for the next event.

Further trigger lines are generated by two scintillators, connected to photomultipliers, that are placed beneath and above the GEM and are sensitive to cosmic muons. After discrimination of their signal at a threshold of -87.0 mV with a discriminator by the ELab, the scintillators signals are fed to a *CAEN N455* coincidence unit. If coincident within 20 ns, this NIM signal provides the second trigger line.

Combining this trigger line trough a *ELab* delay unit of 140*ns* with the detector's signal, one derives the triple coincidence trigger line with another *CAEN N455* coincidence unit. Putting a *CAEN N1145* scaler in each of the last two trigger circles, the ratio of three- to twofold coincidences can be detected, as it is necessary for efficiency measurements. Since the scintillator's sensitive surface of 160×90 mm^2 is larger than the GEM's active area, one has to consider this difference for efficiency

calculations (see Ch. 5.1).

3.4.2 Protection Circuit

As it was already mentioned in Ch. 2.3 and Ch. 3.2, discharges may occur in the GEM detector, induced by heavily ionizing particle. Unlike other MSGCs[6], the GEM foil discharges do usually not propagate all the way to the anode. This is due to the separation of the readout structure from the amplification region at distances of a few millimeters which represents already a long passage for electrons. Therefore, discharges may result in large but fortunately non-destructive signals [Bach 02]. One the one hand, prevention of damages in the foils is done via large loading resistors, as explained in the previous Ch. 3.2. On the other hand, discharges towards the anode structure cannot be completely excluded. Therefore a protection circuit is implemented between the readout structure and the preamplifier, as it is schematically illustrated in Fig. 3.10.

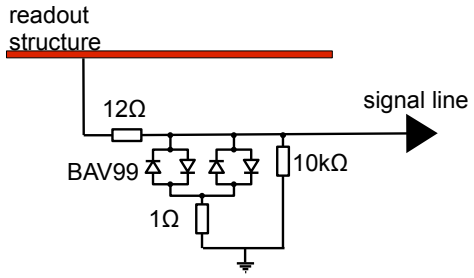

Figure 3.10: Schematics of the protection circuit of two fast BAV)) protection diodes and the subsequent preamplifier connection to the anode of the triple GEM detector.

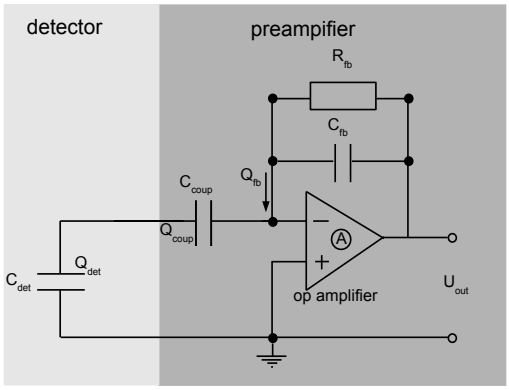

Figure 3.11: Details of a charge sensitive preamplifier. The detector capacity is schematically shown to the left. The protection circuit is omitted for clarity.

The protection circuit consists of two *BAV99* small signal diodes with a breakdown voltage of 70 V and a characteristic low capacity of 1.5 pF [Semi 10]. A resistor of 12 Ω is implemented for protection against high currents that may destroy the diodes. Reduction of the noise level on the anode is done by the 10 kΩ resistor that is connected to ground in the signal line.

3.4.3 Preamplifier

Fig. 3.11 shows the components of a charge sensitive preamplifier. The values of coupling capacitor, feedback capacitor and feedback resistor are shown in Tab. 3.1. The coupling capacity C_{coup} of a charge sensitive preamplifier is usually in the range of a few nF; whereas the feedback capacity C_{fb} is about a factor of 1000 smaller, to ensure a reasonable gain of the outgoing voltage. Tab. 3.1 shows also the feedback resistors R_{fb} of the individual preamplifiers. They define the decay time of the output signal.

The used preamplifiers consist of two amplification stages, one of them being the mentioned charge to voltage conversion, connected to a voltage amplifier. The total charge Q_{tot} that is generated by

[6] **M**icro **S**tructured **G**aseous **C**hamber

preamplifier	C_{coup}	C_{fb}	R_{fb}	F_{CV}
CATSA 82	50 nF	10 pF	30 MΩ	$1\frac{V}{pC}$
Canberra 2004	970 pF	4.7 pF	13 MΩ	$0.83 \pm 0.04\frac{V}{pC}$
LMU *ELab* 2010	1.5 nF	1 pF	66 MΩ	not calibrated

Table 3.1: The three different preamplifiers and their values of coupling and feedback capacity, as well as the feedback resistors's value. F_{CV} is the total conversion factor of the individual preamplifier (see text).

an ionizing particle and amplified by the GEM foils, reaches the anode and will split into two parts. Q_{det} is the part remaining on the anode's capacity C_{det}; whereas Q_{coup} denotes the amount of charges flowing on the coupling capacitor of the preamplifier. Due to voltage equalization one gets:

$$Q_{tot} = Q_{det} + Q_{coup} \tag{3.1}$$

and

$$U_{in} = \frac{Q_{det}}{C_{det}} = \frac{Q_{coup}}{C_{coup}} \quad . \tag{3.2}$$

The charge sensitive amplifier is an inverting charge-to-voltage converter with feedback to its negative operational amplifier input. The charge on the coupling capacitor Q_{coup} is compensated by the contrary signed charge Q_{fb} on the feedback capacitor [Spie 05]:

$$U_{fb} = (A+1) \cdot U_{coup} = (A+1) \cdot U_{in}, \tag{3.3}$$

where A denotes the internal amplification factor of the amplifier.
Thus the voltage gained at the exit of the operation amplifier is only dependent on the feedback capacity C_{fb} and proportional to the incoming charge Q_{coup}:

$$U_{out} = \frac{Q_{fb}}{C_{fb}} = -\frac{Q_{coup}}{C_{fb}} \tag{3.4}$$

In case of a downstream amplifier the output voltage is given by:

$$U_{out} = -\frac{Q_{coup}}{C_{fb}} \cdot A \quad , \tag{3.5}$$

with A being the amplification factor of the downstream amplifier. The total conversion factor F_{CV} of the Canberra 2004 preamplifier is mentioned in the data sheet with 1 V/pC.
Since for the other preamplifiers no official facts about the gain factor were provided, the conversion factor of the home-built *ELab* was calibrated using the Canberra data and repeating measurements under similar conditions. The *CATSA82* shows less amplification due to a large coupling capacity C_{coup} compared to the other preamplifiers; thus it was not calibrated.
The presented simple considerations will be completed and referred to in later chapters (cf. Ch. 4 and Ch. 7).

3.5 Methods of Signal Analysis

Signals by the triple GEM detector and recorded with the flash ADC are processed for further studies with the following software algorithm : an inverse Fermi-function is fitted to the rising edge:

$$f(x) = \frac{par0}{\exp\frac{par1-x}{par2}} + par3 \tag{3.6}$$

which can be seen in Fig. 3.12. Due to the characteristics of the flash ADC, namely its 12*bit* range and 1 GHz sampling frequency, the axes scaled with a factor $m_{ADC} = 0.244$ mV and 1 ns, respectively. The behavior of the fit function is determined by four parameters, starting with $par0$ that reflects the maximum of the signal, i.e. the pulseheight.

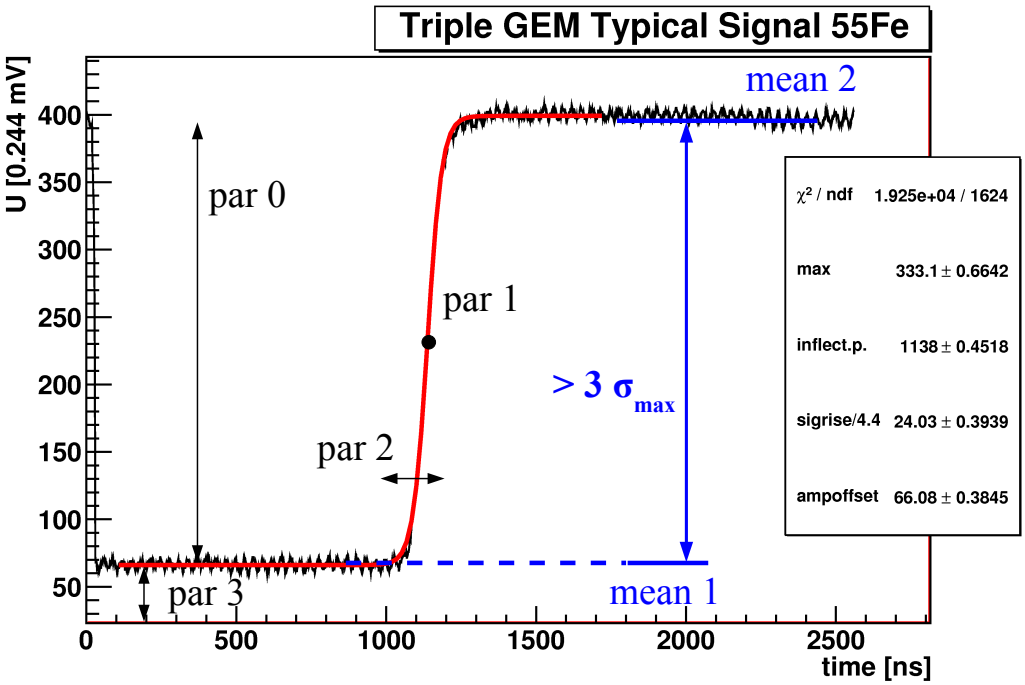

Figure 3.12: A typical signal generated by ^{55}Fe in the GEM detector and recorded with the FADC. The inverse Fermi-function is shown in red, fitted to the rising edge.

The second parameter $par1$ provides the inflection point of the pulse and therefore a possibility for calculating the exact event time. In the measurements presented in this work, the signal time should stay constant, as for cosmics the implemented trigger scintillator deliver a fast signal. This holds also for the ^{55}Fe source measurements since in this case the signal is triggering its acquisition.
In the inverse Fermi-function the $par2$ represents the rise time of the signal. Solving equation 3.6 for given values of 10% and 90% of the maximum pulseheight, one gets a factor of 4.4 which has to multiplied with $par2$ for receiving the signal's risetime in this range. The added forth parameter $par3$ corresponds the offset of the preamplifier. In order to record a complete pulse spectrum for measurements of cosmic muons including also very small signals, every pulse passing the discriminator in the hardware chain was recorded without any further software discrimination since every signal triggered by the scintillators can be considered a real event.
This is not necessarily true for X-ray measurement, where no scintillators are triggering but the first

trigger line, i.e. the detector itself, is responsible for activating the readout electronics. Therefore a software discrimination is reasonable and implemented in the analyzing algorithm. In a time frame of about 400 ns before the signal rise and 1000 ns after the signal's maximum, average values of the data point in these frames and their standard deviations are calculated. The Fermi-function fit will only be executed if the difference between the two average values is bigger than three times the maximal standard deviation:

$$mean2 - mean1 > 3 \cdot \sigma_{max} \longrightarrow \text{executing Fermi} - \text{fit} \tag{3.7}$$

Independent of the software cuts, all parameters of the fit function are filled in histograms for the corresponding data samples and are the basis for the following analysis.

Chapter 4

Energy Resolution and Pulse Height Analysis

This chapter addresses the analysis of measurements of cosmic muons as well as X-rays from a ^{55}Fe source. At first the resolution of pulse spectra resulting from a ^{55}Fe source is documented as it is obtained by prototype 1.0 for different anode geometries recorded by various preamplifiers. As Ch. 4.2 illuminates, the resolution was found to depend on the source position. The following section about the energy distribution for cosmic ray muons completes the topic of energy resolution of the prototype 1.0. Ch. 4.4 treats the charge transfer processes in a GEM and the impact of the electric fields on it. Detailed measurements regarding the pulse height dependence on the electric field of the induction gap, E_{ind}, can be found subsequently. After the installation of a five-fold segmented anode, we describe in Ch. 4.5 changes of the pulse height as a function of segmentation.

4.1 ^{55}Fe Pulse Spectra and Energy Resolution

4.1.1 Spectrum Recorded with Unsegmented Anode Readout via *CATSA82* Preamplifier

As in Ch. 1.1.2 already covered, the photons generated by the ^{55}Fe decay carry mainly an energy of $E_\gamma = 6.50$ keV, 5.90 keV and 2.68 keV. They interact with gas molecules due to the photoelectric effect. Recording these peaks in the spectrum of ^{55}Fe is the motivation of the following measurement in order to state the energy resolution of the triple GEM.
The source is placed centrally above the active area as described in Ch. 3.1 and readout via the first trigger line with self-triggering detector. The lower scintillator (Sc1, cf. Ch. 3.4.1) is used as a veto-trigger for discriminating accidental recording of cosmic muons. In Fig. 4.1 the pulse height spectrum of ^{55}Fe is plotted as taken with the first setup of prototype 1.0, that is including an unsegmented Cu-anode and readout via the *CATSA82* preamplifier. The peak on the left is due to remaining cosmics which traverse the detector under a large zenith angle without hitting the bottom scintillator. Their spectrum is fitted with a Landau distribution and will be reviewed in upcoming sections.

The peaks of interest are the central and the right ones which represents the characteristic escape peak, the K_α line and the K_β peak, respectively. For stating quantitatively the energy resolution, three Gaussian functions are fitted to the histogram:

$$G(x,\mu,\sigma) = \frac{1}{\sigma \cdot \sqrt{2\pi}} \cdot \exp \frac{-(x-\mu)^2}{2\sigma^2} \tag{4.1}$$

where μ identifies the mean and σ the standard deviation of the distribution [Leo 94]. The total fit function is the sum of the Landau function together with the two Gaussians for the ^{55}Fe spectrum. It is indicated by the black envelope.

For calculating the energy resolution dE/E at full width of half maximum (FWHM), as it is commonly used, one needs to transfer σ to full width at half maximum:

$$FWHM = 2 \cdot \sigma \cdot \sqrt{2 \ln 2} = 2.35 \cdot \sigma \tag{4.2}$$

Fig. 4.1 yields a $dE/E = 22.5\%$ for the first measurements. The K_β- peak that underlies the dominant K_α line can be seen on the right shoulder.

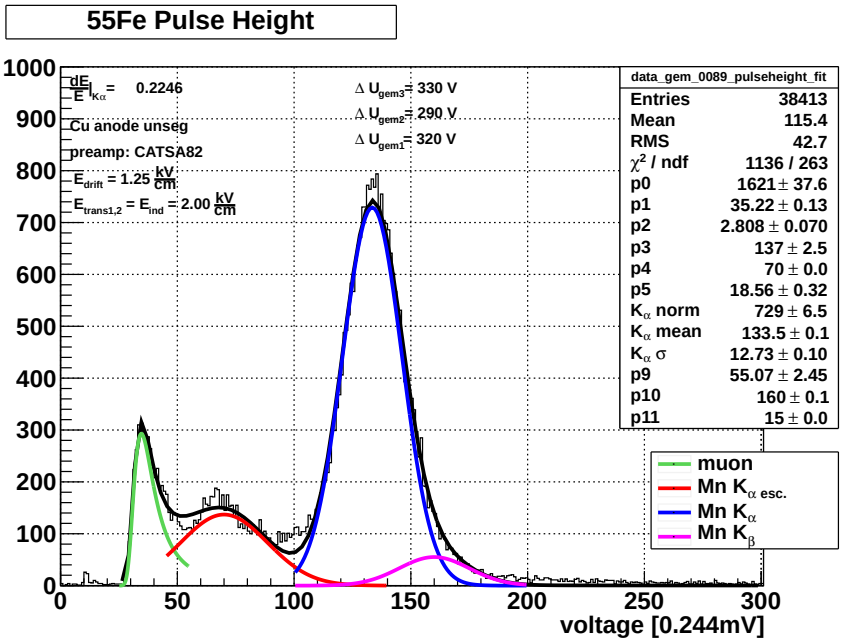

Figure 4.1: Pulse spectrum of ^{55}Fe detected by the prototype 1.0 equipped with an unsegmented Cu anode. An energy resolution of 22.5 % is observed for a centrally placed irradiation source. The escape peak lies around ADC channel 70, the K_α peak around 133. The K_β peak is shown on the right shoulder at channel 160.

4.1.2 Energy Resolution with a Five-Fold Segmented Anode

In order to compare results from the unsegmented anode with results from the five-fold segmented anode, the latter is readout via one signal line, i.e. all five strips are shorted to one readout and fed to the homemade preamplifier by the LMU *ELab*. Furthermore, the uppermost two GEM foils were exchanged to new ones resulting in a higher applicable potential difference and gain. The same electric fields were applied to the gaps to guarantee equal drift properties. The energy resolution of the thus rebuilt detector shows a slightly better performance in terms of resolution (Fig. 4.2). The spectrum is shifted by approximately a factor of 5 to higher values due to a greater amplification

factor of the *ELab* preamplifier. The measured and expected positions of the peaks are shown in Tab. 4.1, calibrated with respect to the K_α line.

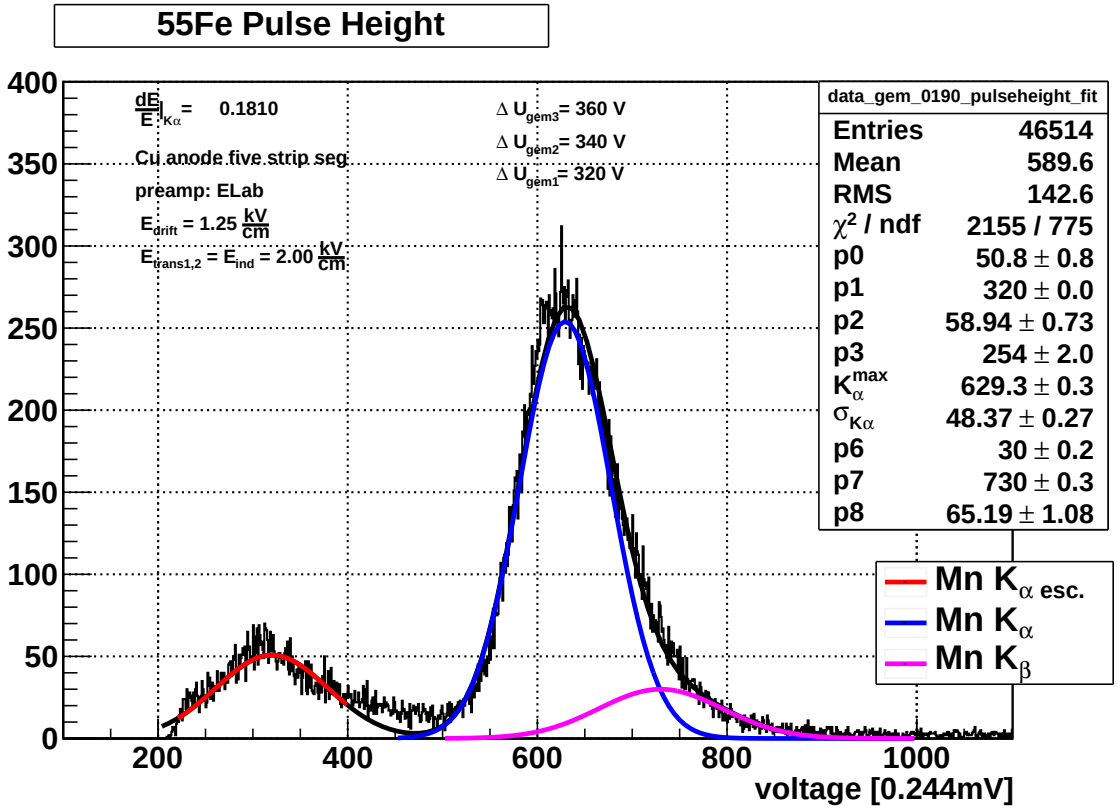

Figure 4.2: Histogram of pulse heights of the ^{55}Fe spectrum recorded with the *ELab* preamplifier and five-fold segmented anode. The underlying K_β peak (magenta) is shown on the right shoulder of K_α. An energy resolution of $dE/E = 18.1\%$ for the K_α line is observed.

	Energy [keV]	measured mean of ADC counts	expected mean of ADC counts
K_α escape	2.68	320	285
K_α	5.90	628	628
K_β	6.50	730	689

Table 4.1: Spectrum and expected mean values of ^{55}Fe spectrum recorded with *ELab* preamplifier and the five-fold copper anode that was shorted to one signal line.

Furthermore, measurements of the ^{55}Fe energy spectrum with a *Canberra2004* preamplifier were implemented. Fig. 4.3 shows an exemplary spectrum as taken with this preamplifier. In these measurements the potential differences at the foils were chosen to be identical and smaller compared to the previous plots. The energy resolution for the fitted K_α peak is observed to be approximately 18%.

Comparing the spectra taken with these three different preamplifier it is obvious that they do not affect the energy resolution of the detector which lies in the range:

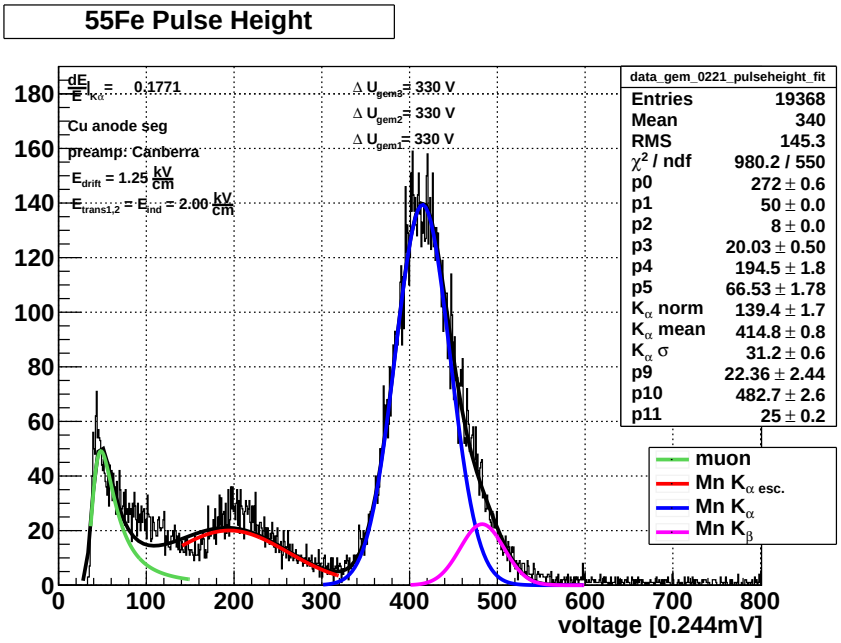

Figure 4.3: ^{55}Fe pulse height spectrum as taken with *Canberra2004* preamplifier. All peaks are resolved. An energy resolution of $dE/E = 17.7\%$ for K_α is observed.

$$\left(\frac{dE}{E}\right)_{FWHM} = 0.20 \pm 0.03 \tag{4.3}$$

for all tested setups.

The statistical limit gives a lower limit for the resolution. The relative mean error of a Poisson distribution is given by [Leo 94]:

$$\frac{\sigma}{\mu} = \frac{1}{\sqrt{\mu}} \tag{4.4}$$

with the mean μ and the standard deviation σ. Considering the fact that the energy of a single K_α photon can be identified with an ionization of $\mu = N = 223$ molecules of the filling gas, one receives theoretically a lower limit for the relative resolution at FWHM:

$$\left(\frac{dE}{E}\right)_{FWHM} = 2.35 \cdot \left(\frac{1}{\sqrt{\mu}}\right) = 2.35 \cdot \left(\frac{1}{\sqrt{N}}\right) = 2.35 \cdot \frac{1}{\sqrt{223}} = 0.1576 \quad . \tag{4.5}$$

The factor 2.35 corresponds to the former presented relation of the standard deviation of a Gaussian distribution and the full width at half maximum. Inclusion of the *Fano factor F* [Fano 47] leads to:

$$\sigma^2_{corr} = F \cdot \mu \quad . \tag{4.6}$$

where F characterizes the detecting gas as a function of all possible processes of particle in the medium, i.e. including photon excitation [Leo 94]. In the case of pure Argon the Fano factor has a value of [Hash 84]:

$$F = 0.23 \quad . \tag{4.7}$$

Thus the lower limit of energy resolution at FWHM including Fano's correction factor is:

$$\left(\frac{dE}{E}\right)_{FWHM} = 2.35 \cdot \sqrt{\frac{0.23}{223}} = 0.076 \tag{4.8}$$

The demonstrated results deviate from the calculated statistical limit by a factor of three. Nevertheless, the energy resolution of prototype 1.0 is in agreement with results reported by other authors regarding triple GEM detectors [Altu 02], [Simo 01], [Haas 04].

4.2 Homogeneity of Pulse Height

So far, only measurements were considered in which the source is placed centrally on the detector. In order to make statements about the energy resolution of the whole detector, the homogeneity of the foils is tested at different source locations.

4.2.1 Energy Resolution for Different Source Positions

Measurements with the first setup were taken at five different locations for testing the overall performance of the triple GEM detector. As it is schematized in Fig. 4.6 the irradiation inlets are realized by holes of 4 mm diameter, sealed with kapton layers.
A Gaussian fit to the data results in an energy resolution between 17% and 21% for the peripheral regions (see Fig. 4.4). For a centrally located irradiation one observes a slightly worse resolution of 22.5%, as reported in Fig. 4.1. This behavior arises from the fact that the GEM foils are not stabilized in their active region. Spacers are glued to the frame and are also placed on the supporting rods (see Fig. 3.2). Due to electromagnetic forces at the electrodes, the foils are not planar but deformed in the not supported central area. This leads to electric field distortions which influence the drift and gas gain properties, resulting in a degradation of resolution.
The statement that the resolution in the central area impairs due to field effects is verified by examination of the measuring time of the data samples. A data set of $N = 40000$ is taken for every source location with a deviation from the average measuring time of only 2% including the data set at the central region (see Fig. 4.5). If there were any inefficiencies of the material the recording time were increased assuming a constant freauency of irradiation. This is confirmed by the pulse height distribution shown in Fig. 4.7. A decrease of about 20% in pulse height of the signal for the central region is observed. Since the counting rate of the central point is not decreasing but only the pulse height is affected, one can state that the decrease in energy resolution is mainly due to complex field alternations and not to any inefficiencies of the GEMs.

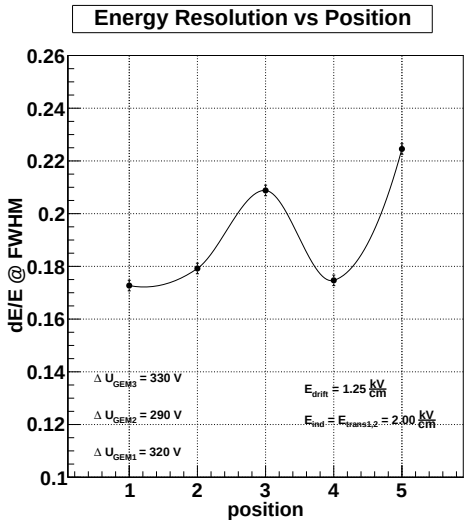

Figure 4.4: Homogeneity test via energy resolution at five source positions. The central region's resolution differs from the peripheral regions by 20 %.

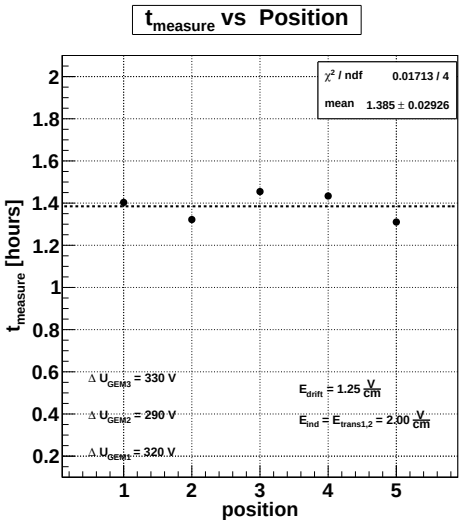

Figure 4.5: Duration of data taking for 40000 events at five positions. The data deviates 2% from the mean value of 1.39 hours.

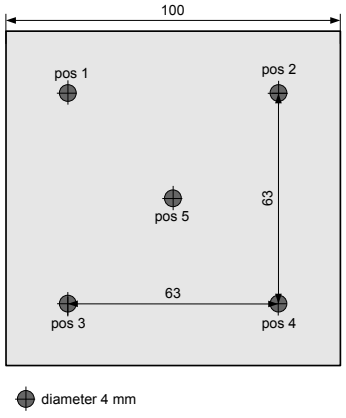

Figure 4.6: Schematics of the possible locations of an irradiation source with respect to the GEM foils (repetition).

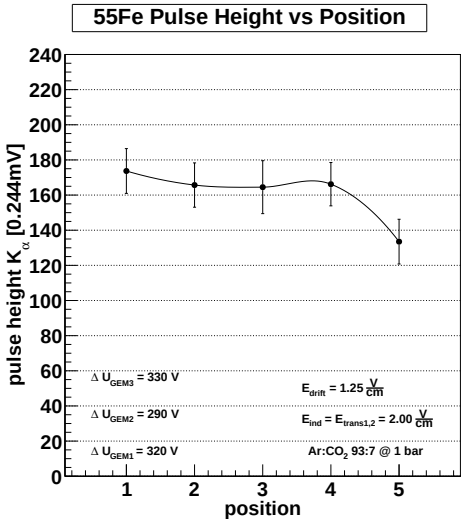

Figure 4.7: Pulse height of K_α as a function of source location.

4.3 Cosmic Muon Spectrum

The ^{55}Fe source served well for determination of the energy resolution since it provides a discrete line spectrum for calibration. However, X-rays do not provide an external trigger and therefore can not be used to evaluate, for example, the efficiency (see Ch. 5) of the triple GEM detector.
Looking for sources with higher energies, the omnipresent cosmic ray muons are a favorable choice for further detector tests. Their energies are high enough to trigger the scintillation counters while still penetrating the detector. This section illustrates the characteristics of cosmic muons as minimum ionizing particle (MIPs) and reports on measurements of their spectrum with the prototype 1.0.

4.3.1 Pulse Height Spectrum of Cosmics

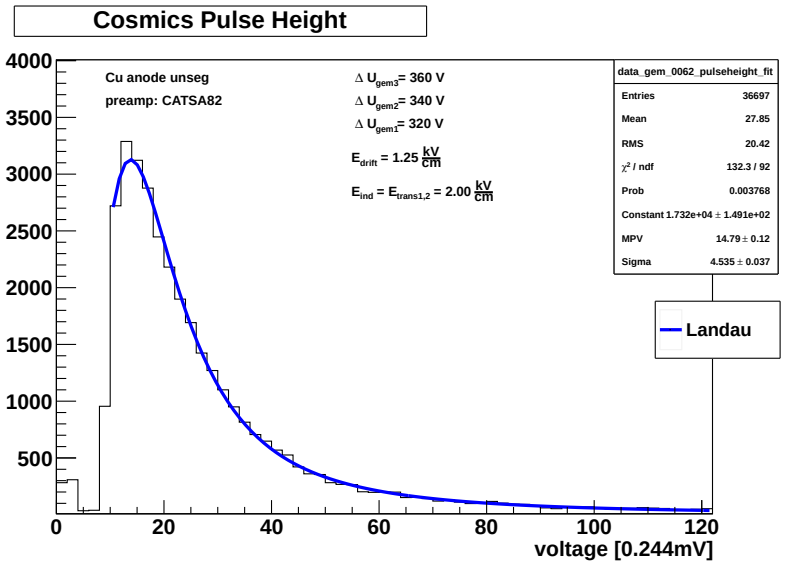

Figure 4.8: Pulse height spectrum of cosmic muons recorded with prototype 1.0 and single plane readout.The spectrum is cut off due to preamplifier performance.

Muons account for 80% of all charged cosmic ray particle at ground level [Grup 08]. A minimum ionizing muon, that is a particle of $\beta\gamma \approx 4$, carries an energy of $E_\mu \approx 420$ MeV. In a gaseous environment of Ar/CO_2 at a fraction of $93/7$ this muon creates approximately 97 primary electron-ion-pairs per cm due to inonization [PDG 10]. According to this and considering the dimension of the detector, about 39 primary electrons are realeased by a cosmic ray muon that penetrates the drift region perpendicular to the active area. Since the angular distribution of cosmic ray muons is proportional to $\cos^2\theta$, with θ being the zenith angle, this is the most probable value to assume [PDG 10]. For a given maximal incident angle of $\theta = 63^\circ$, that is defined as the zenith angle of a muon hitting the inner edges of both scintillators (see Ch. 5.1), this number increases to approximately 86 charges in the drift gap. As discussed in Ch. 1.1.1 this calculation holds for the average energy loss $\left\langle \frac{dE}{dx} \right\rangle$ which is denoted by the *mean* in the presented histogram. As the prototype 1.0 contains a drift gap of 4 mm, it can be treated as a thin absorber and a Landau distribution is used to describe the muon's energy distribution (see Ch. 1.1.1). Fig. 4.8 illustrates such a distribution as it is taken with the first detector setup.

The data taking of cosmics with an equivalent sample size compared to ^{55}Fe X-rays is achieved during

overnight measurements. This is due to the fact that the muon flux rate of $1\text{cm}^{-2} \cdot \text{min}^{-1}$ [Grup 08] is rather small and results in a detection frequency of approximately 0.7 Hz.
From Fig. 4.8 it is obvious that the Landau function fitted to the histogram is in good agreement with the data. However, one can observe that the spectrum is cut off at low energies. This is an artefact of the preamplifier *CATSA82* which amplifies the signal not high enough. The discriminator in the hardware readout chain had to be set at a threshold that prevented signals corresponding to a low energy loss of the muon from being detected. Therefore a complete analysis of the energy loss could not be accomplished. With the implementation of another preamplifier (*ELab*) this problem was solved and allows for further studies in the next section.

4.3.2 Complete Pulse Height Analysis of Cosmic Signals

By exchanging the preamplifier in the signal readout a full spectrum of energy loss distribution of cosmic ray muons is detectable. During the implementation of the *ELab* preamplifier also the five-fold segmented anode (cf. Ch. 3.1.1) was embedded. Fig. 4.9 shows an exemplary data set of a full energy loss spectrum.

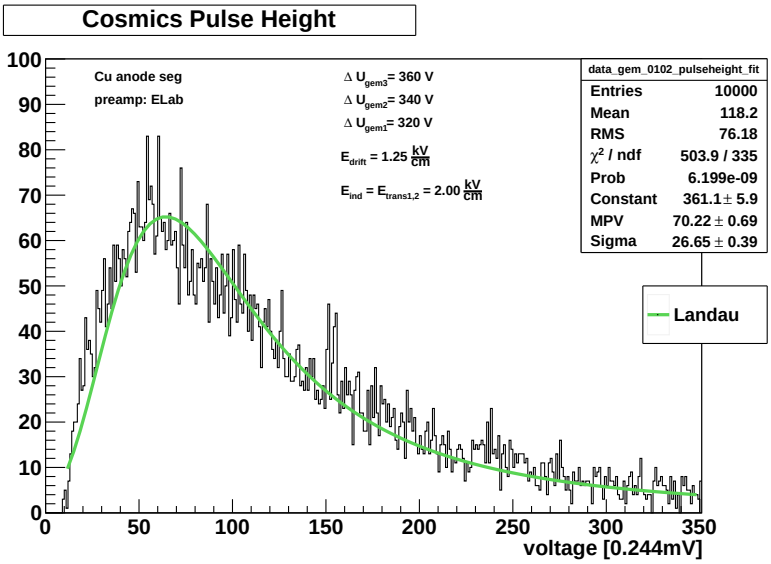

Figure 4.9: Pulse height spectrum of cosmic muons. Recording via *ELab* preamp. Full spectrum detectable.

The green line corresponds to a Landau fit [Kolb 84]. Its quality is indicated by the χ^2/ndf - value which should be close to 1 for a meaningful fit. Recent studies provide a different parametrization for the energy loss distribution for thin absorbers which differs from the commonly applied Landau distribution. The differences between the original Landau function and the fluctuations including "straggling function" (Landau-Bichsel-distribution) [Bich 06] can be seen in Fig 4.10. The solid line shows the corrected energy loss for minimum ionizing particle ($\beta\gamma = 3.6$) penetrating through a 1.2 cm thin layer of Argon; whereas the dotted line indicates the original Landau function for such particle. The most probable value (MPV) is slightly shifted to lower energies and the distribution extents to zero. In comparison to that the classical Landau distribution provides a smaller range of energy loss and a shorter tail. Comparing this with the experimental results it can be stated that the Landau-Bichsel function would describe the measurements better since the distribution also extends

to zero. Nevertheless, the fit function used in Fig. 4.9 suits the measurements in a good manner, confirmed by a $\chi^2/ndf = 1.41$.

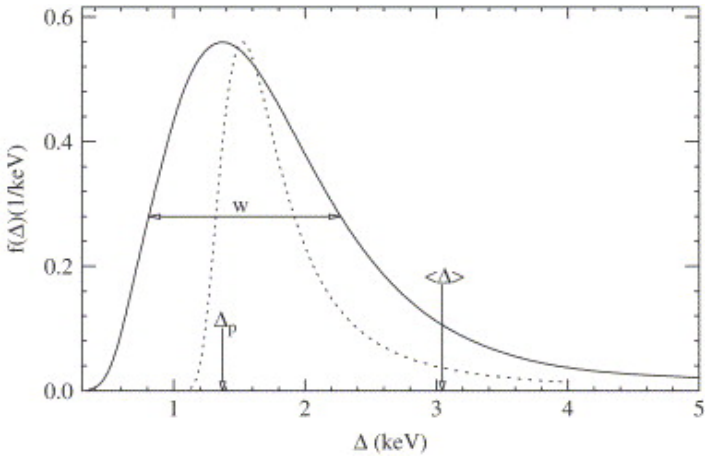

Figure 4.10: Energy loss distribution function for MIP $\beta\gamma = 3.6$ in an 1.2 cm thin Argon layer. The function corresponding to the solid line includes fluctuations. The original Landau distribution is indicated by the dotted line [Bich 06].

A statement of quality for the presented data can be given by approximating the average energy loss $\left\langle \frac{dE}{dx} \right\rangle$ of the shown distribution and comparing it with theoretical values. The ^{55}Fe measurements presented in Ch. 4.1 suits for transforming the FADC scale into meaningful energy units. Since the K_α line and the K_α escape peak represent energies of 5.90 keV and 2.68 keV respectively, (see Ch. 1.1.2), one derives a scaling factor by taking a data set with corresponding operation parameters. This is done via the measurement presented in Fig. 4.2. From table 4.1 one derives a linear relation between the two energies with 10% deviation. This results in a scaling factor of 9.4 eV/channel. Thus the *mean* value of 118.2 of the distribution in Fig. 4.9 is equivalent to a mean energy loss of:

$$\text{mean} \times \text{scalingfactor} = 118.2 \text{ channel} \times 9.4 \frac{\text{eV}}{\text{channel}} = \left\langle \frac{dE}{dx} \right\rangle \approx \frac{1111 \text{ eV}}{4\text{mm}} \tag{4.9}$$

On the other hand, the mean energy loss is related to the average energy $\langle W_i \rangle$ required for the production of primary electron-ion-pair and their total number $\langle n_t \rangle$ as explained in Ch. 1.1.2. Including the theoretical values of $\langle n_t \rangle = 97$ per cm and $\langle W_i \rangle = 26.50$ eV for Ar/CO_2 at a ratio of 93/7 one derives a mean energy loss of:

$$\left\langle \frac{dE}{dx} \right\rangle = \langle W_i \rangle \cdot \langle n_t \rangle = 26.50 \text{ eV} \cdot \frac{97}{\text{cm}} \cdot 0.4 \text{ cm} = 1028 \text{ eV} \tag{4.10}$$

in 4 mm drift. The experimental results are consistent with the theoretical estimated mean energy loss within 8% deviation.

4.4 Pulse Height Dependence on Induction- and Drift - Fields

Since the introduction of the gas electron multiplier thirteen years ago, various studies were published concerning the charge transfer in GEM detectors depending on the applied fields of drift and induction region (see for example [Bach 99], [Shar 00a], [Shar 00b] and [Gued 03]). This is essential to understand the physical processes taking places in a GEM detector. Some important outcomes of these studies including simulations of field configurations are summarized in the first part of this section before data samples taken with the prototype 1.0 will be presented and discussed.

4.4.1 Charge Transfer Processes in a GEM Detector

To investigate the field line configurations in a GEM detector the simulation package GARFIELD [Veen 98] was used. Fig. 4.11 shows a cross section of a GEM foil placed in an induction field and in a drift field of 2 and 6 kV/cm, respectively. The electrons released in the drift region by a traversing ionizing particle are guided along the field lines to the foil without any losses since diffusion processes can be neglected for drift fields $E_{drift} > 100$ kV/cm [Bach 99].
It was pointed out that a fraction of charges will not reach the induction field region but is collected by the GEM electrodes. Due to particle collisions inside the GEM holes the amplified charges deviate from the central amplification channel into regions where field lines are ending on the foil. Depending on the field strength a fraction of the amplified electrons will be extracted by the lower and ions by the upper electrode. This is also shown in Fig. 4.13 for the electrons. Applying the fields in an inversed manner and lowering the GEM voltage difference results in a field map according to Fig. 4.12. It is obvious that the electron transparency[1] is lower in this configuration compared to the previous since field lines are ending on the upper electrode.

By comparing Fig. 4.11 and Fig. 4.12 one can expect that the fraction of electrons reaching the readout is strongly affected by the induction field for otherwise constant operation parameters. Researches on a single GEM detector found the effective gain of the detector to increase almost linearly for $0 \leq E_{ind} \leq 2$ keV/cm (Fig. 4.14). According to the author this fact indicates that the dependence is only due to electrostatic effects [Bach 99]. At an induction field of $E_{ind} \approx 8$ kV/cm the linear approach is substituted by another rise. This gain results from the induction field itself that reaches values that are high enough for extending the gas amplification area to the vicinity of the lower electrode resulting in a larger amount of liberated electrons [Bach 99].
For a double GEM detector the dependence of the signal height with respect to the induction field is similar, as shown in Fig. 4.15. The pulse area in the denoted plot is proportional to the total charge reaching the readout structure [Gued 03].
These summarized results give a glance at how electrons travel across a GEM detector and underline that the choice of the drift and induction fields have a big influence on the detected signal.

[1] for definition see Ch. 2.2

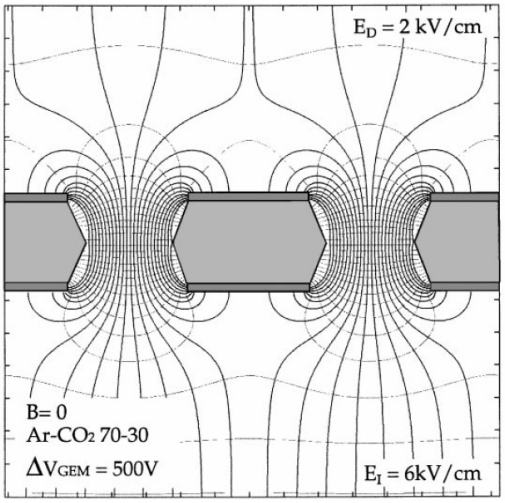

Figure 4.11: GARFIELD simulation of electric field lines in an operation mode of $\Delta U_{GEM} = 500$ V, $E_{drift} = 2$ and $E_{ind} = 6$ kV/cm in $Ar/CO_2 = 70/30$ [Bach 99].

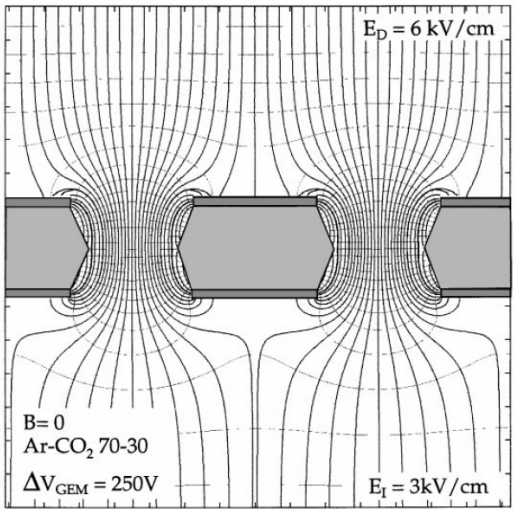

Figure 4.12: GARFIELD simulation of electric field lines in an operation mode of $\Delta U_{GEM} = 250$ V, $E_{drift} = 6$ and $E_{ind} = 2$ kV/cm [Bach 99].

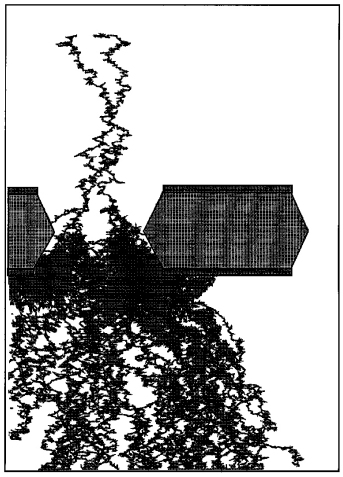

Figure 4.13: GARFIELD simulation of an avalanche process in a GEM hole [Shar 00b].

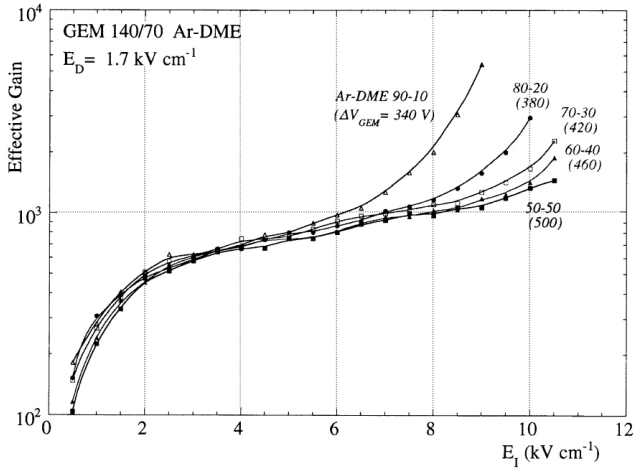

Figure 4.14: Effective gain for several gas mixtures dependent on the induction field strength E_{ind} [Bach 99].

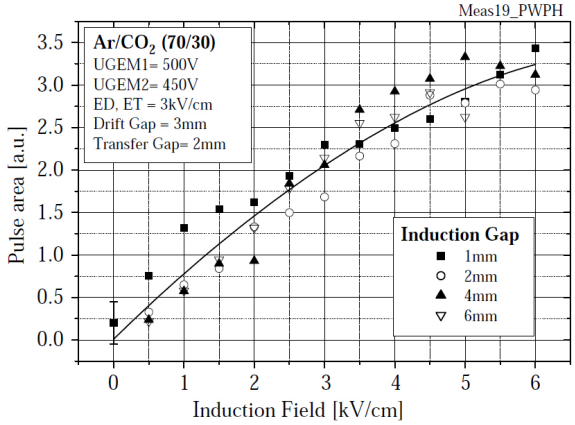

Figure 4.15: Pulse area ($\hat{=}$ pulse height) as a function of induction field strength E_{ind} for a double GEM detector in Ar/CO_2 at $70/30$ [Gued 03].

4.4.2 Impact of Induction- and Drift-Field Variations on the Signal

In order to analyze the pulse height dependence on variations of electric fields surrounding the GEM foils, we took data with cosmic ray muons and X-Rays from the ^{55}Fe source. Fig. 4.16 displays results of data for cosmics taken by the triple GEM detector with five-fold segmented anode and readout via the *ELab* preamplifier. For this measurement we chose the applied potential differences at the foils to be slightly cascaded:

$$\Delta U_{GEM1} = 320 \text{ V} \ , \ \Delta U_{GEM2} = 340 \text{ V } \textit{and } \Delta U_{GEM2} = 340 \text{ V} \ ,$$

for reasons of better operation stability. The drift field and the transfer regions $E_{trans1,2}$ were held at constant values of $E_{ind} = 1.25$ kV/cm and $E_{trans1,2} = 2.00$ kV/cm, respectively. The potential difference at the individual GEM foils is also held at constant values for a stable gain per foil. It is shown that the recorded pulse height is increasing linearly with the induction field. The range of applicable field strength is limited at the lower side by the pulse height which is not rising above the noise level for $E_{ind} < 800$ V/cm. On the upper limit frequent discharges in the order of $\mathcal{O}(\text{discharge}) \approx 1\text{min}^{-1}$ prevent higher induction fields. The pulse height is increased by a factor of two over a range of 1 kV/cm stating a doubled extraction efficiency due to better transparency of E-field lines through the holes of foil GEM1 (see Ch. 4.4.1).

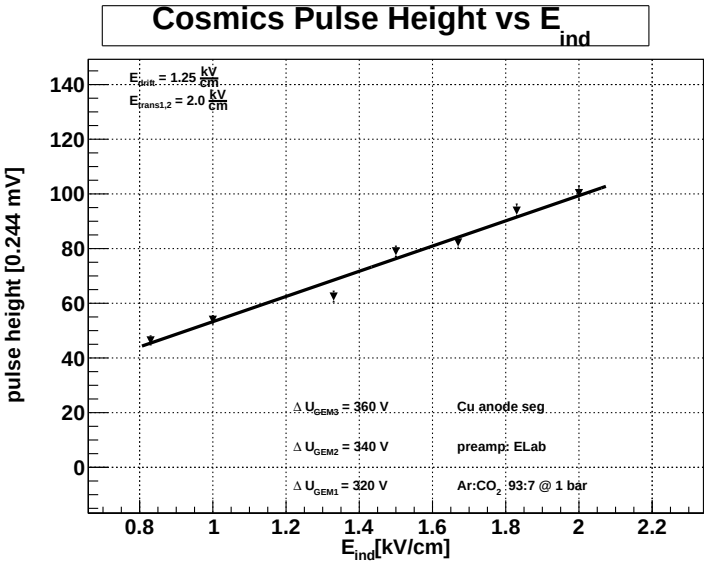

Figure 4.16: Pulse height of cosmic muons as a function of induction field E_{ind}.

The X-rays from the ^{55}Fe source, in contrast, deposit their total energy in the drift gap since they are absorbed via the photoelectric effect. Therefore higher pulses are generated. This results in a broader range of induction field variation for the measurements (Fig. 4.17). The data confirms the assumption of a linearly increasing pulse height with the induction field E_{ind} in accordance with the effects found for double GEM detectors in the corresponding field range [Gued 03].
Fig. 4.18 shows the same data set but translated to effective gain as a function of the induction field. Please see Ch. 7 for details of this translation. For comparing these results with those of a single GEM detector (Fig. 4.14) one has to take the different gas mixtures into account. Furthermore our triple GEM configuration yields, of course, a higher gain than a detector containing only one amplification stage. Nevertheless, it can be concluded that the triple GEM prototype 1.0 is working as expected

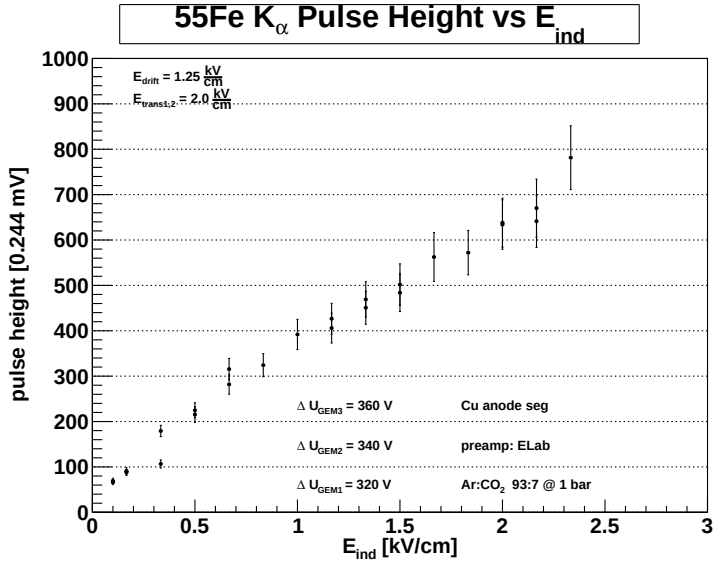

Figure 4.17: Pulse height of K_α peak of the ^{55}Fe as a function of induction field E_{ind}.

since the presented results are in good agreement in the corresponding field range $0.05\ \mathrm{kV/cm} \leq E_{ind} \leq 2.3\ \mathrm{kV/cm}$ with observations reported by [Bach 99] and [Gued 03].

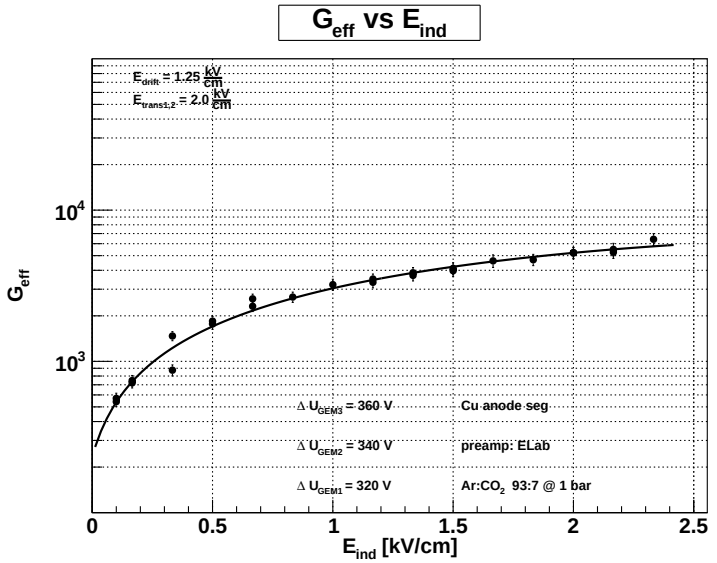

Figure 4.18: Effective gain as a function of induction field E_{ind}.

We have also investigated the effect of the drift field on the pulse height with constant transfer and induction fields for comic ray muons. The MPV[2] of the Landau spectrum is plotted as a function of increased field strength of the drift gap in (Fig. 4.19). The effect of less electron losses to the lower *GEM1* electrodes by increased induction field is visible in the vertical shifting for three different induction and transfer fields. The highest pulses are recorded for a constant $E_{ind} = 2.0$ kV/cm. Owing to an improved separation of primary electrons from ions with increased induction field one

[2]**M**ost **P**robable **V**alue

observes a greater pulse height for all three configuration at $E_{drift} = 1.25$ kV/cm. This is followed by a slight decrease going to higher drift fields. One assumes that this may be due to electric field lines ending on the upper electrode of *GEM3* preventing them from being amplified in the GEM foils.

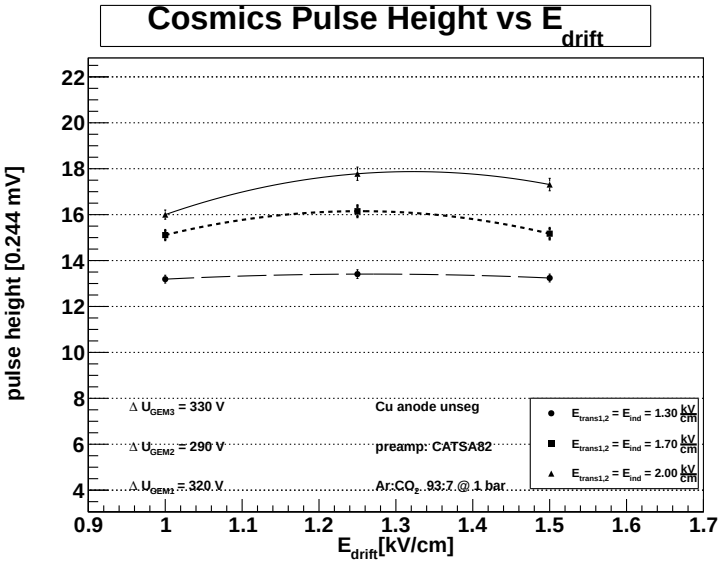

Figure 4.19: MPV of the *Landau* spectra as a function of E_{drift} at constant $E_{trans1,2} = E_{ind}$

This may be just a part of the answer since the physical processes in a triple GEM detector are very complicated [Buzu 02]. Nevertheless, these effects result only in a small variation of 5% in the pulse height concerning measurements at constant $E_{ind} = E_{trans1,2} = 1.7$ kV/cm.

4.5 Pulse Height Dependence on Strip Readout

The five-fold segmented anode was used to study the influence of strip size on the pulse height of the anode signals. Five data points were taken when one, two, three, four and all five strips were readout by one preamplifier. The dimension of a single readout strip is shown in Fig. 4.20. We used the ^{55}Fe source located at the central position and recorded data samples with all three preamplifiers. The readout copper strips of the five-fold segmented anode were coupled together while open strips were connected with a resistor of 100 Ω to ground as shown in Fig. 4.20. Fig. 4.21 repeats schematically the capacities and charge flows necessary for the following calculations. Foremost, data samples with 40000 events taken with the *CATSA82* preamplifier can bee seen in Fig. 4.22. For comparison, the operation parameters were chosen to be identical to a setup with unsegmented anode (round data point in Fig. 4.22). The pulse height is decreasing as more strips are readout being coupled together. This results in a 50% smaller peak for five stripr being read out compared to only one strip-readout. The unsegmented anode shows the lowest pulse height of the ^{55}Fe spectrum.

One observes for all preamplifiers a decreasing pulse height with increasing strip number, see Fig. 4.23. This plot shows measurements at identical operation parameters recorded once with the *Canberra* preamplifier and repeated with the *ELab* version.

The detected charge Q_{tot} flows from the anode (C_{det}) to the coupling capacitor C_{coup}. At equilibrium the voltage on C_{det} and C_{coup} is identical:

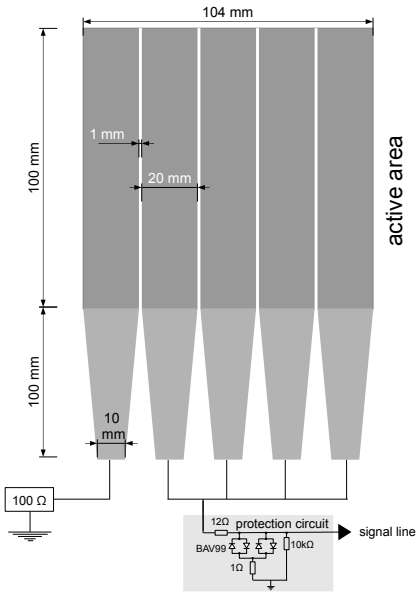

Figure 4.20: Principle of variable strip readout. Exemplary shown is the readout of four strips. A strip has a surface of 0.0035m^2 including an active area of 0.0020m^2.

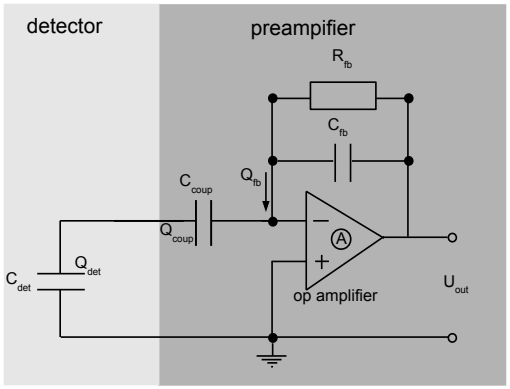

Figure 4.21: Schematic of the charge sensitive preamplifier

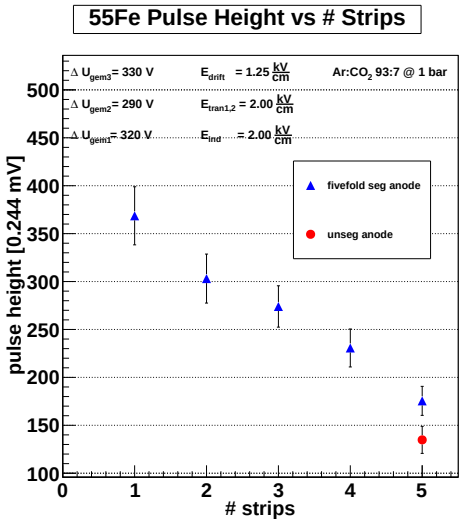

Figure 4.22: Pulse height as a function of the number of readout strips by *CATSA82*.

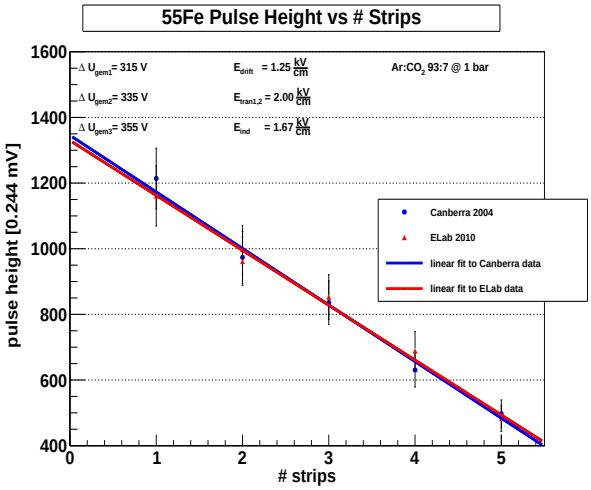

Figure 4.23: Pulse height as a function of the number of readout strips recorded with *Canberra2004* and *ELab* preamplifier, respectively. A linear function is fit to the data.

$$U_{in} = \frac{Q_{det}}{C_{det}} = \frac{Q_{coup}}{C_{coup}} \tag{4.11}$$

where Q_{det} is the part of the total charge Q_{tot} that remains on the anode. Therefore the total charge that was generated by primary ionizing particle and amplified by the three GEM foils, is divided in:

$$Q_{tot} = Q_{det} + Q_{coup} \tag{4.12}$$

from these two equations one derives an expression for the charge on the coupling capacitor:

$$Q_{coup} = \frac{Q_{tot}}{\frac{C_{det}}{C_{coup}} + 1} = \frac{U_{out}}{F_{CV}} \tag{4.13}$$

The pulse height U_{out} is connected to the fraction of charges Q_{coup} via the charge-to-voltage conversion factor F_{CV} of the charge sensitive preamplifier. The *Canberra* has a conversion factor of $F_{CV} = 1$ V/pC and the conversion factor of the *ELab* preamp is 0.83 ± 0.04 V/pC (see Ch. 3.4.3). The amplification factor of the *CATSA82* preamplifier has not been determined since its coupling capacity $C_{coup} = 50$ nF results in less gain.
As the flash ADC records data in a 12 bit range with an acceptance of ± 0.5 mV one can identify a scaling factor m_{ADC}:

$$m_{\mathrm{ADC}} = 0.244 \ \frac{\mathrm{mV}}{\mathrm{ADC\ channel}} \tag{4.14}$$

Using this we transform from the recorded pulse height to the detected charges Q_{coup}.

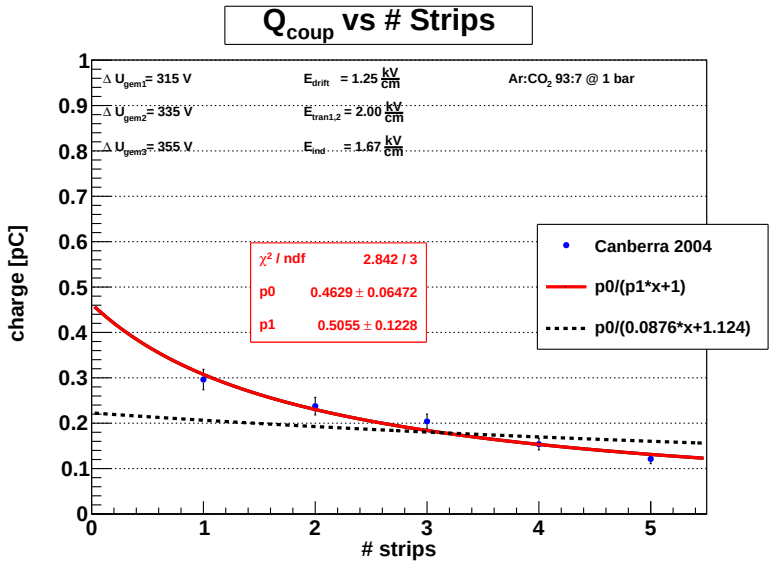

Figure 4.24: Amount of collected charge that reaches the preamplifier as a function of the number of readout strips being coupled together. The decreasing pulseheight is due to increasing detector capacity as a function of readout strips.

In order to proof equation 4.13 the data taken with the *Canberra2004* preamplifier is transformed as it is shown in Fig. 4.24. A fit function with two free parameters is applied to the data (red line in Fig. 4.24) and yields a strip capacity C_{strip}^{PCB} of:

$$C_{strip} = p1 \cdot C_{coup} = 0.5055 \cdot 970 \text{ pF} = 490 \pm 120 \text{ pF} \tag{4.15}$$

assuming the detector capacity to be a multiple of its single strip capacity:

$$C_{det} = n \cdot C_{strip} \quad , \; n \in [1,5]. \tag{4.16}$$

Including the dimension of the readout plane, its thickness d_{PCB} and the area A_{strip} of the readout strips as well as the dielectric constant of the PCB material, the theoretical capacity of a single strip with respect to the backplane is:

$$C_{strip}^{PCB} = \frac{\varepsilon_0 \cdot \varepsilon_{PCB} A_{strip}}{d_{PCB}} = \frac{8.85 \cdot 10^{-12}(\text{F/m}) \cdot 4.5 \cdot 0.0035\text{m}^2}{1.6 \cdot 10^{-3}\text{m}} \approx 85 \text{ pF} \quad . \tag{4.17}$$

Together with the coupling capacity of the *Canberra* preamplifier it is inserted as a fixed second parameter in the fit function:

$$\frac{C_{strip}}{C_{coup}} = \frac{85 \text{ pF}}{970 \text{ pF}} = 0.0876 \tag{4.18}$$

Additionally, the capacity of one strip to its neighboring strips has to be taken into account. The capacity of two neighboring strips with length l, thickness b and distance d can be estimated to be [Nuhr 02]:

$$C_{neighbor} \approx 6.65 \cdot 10^{-2} \cdot \varepsilon_{PCB} \cdot \frac{b \cdot l}{d} \; pF = 6.65 \cdot 10^{-2} \cdot 4.5 \frac{10 \cdot 2}{0.1} = 60 \; pF \quad . \tag{4.19}$$

This theoretically derived values are inserted in the fit function:

$$Q_{coup} = \frac{Q_{tot}}{n \cdot \frac{C_{det}}{C_{coup}} + \frac{2 \cdot C_{neighbor}}{C_{coup}}} = \frac{Q_{tot}}{n \cdot 0.0876 + 1.124} \quad , \; n \in [1,5] \tag{4.20}$$

with Q_{tot} being the only free parameter. This fit is shown as dashed line in Fig. 4.24.
From the fit functions' first parameter $p0$ one derives a theoretical range of the total charge:

$$Q_{total} \in [0.25, 0.46]\text{pC} \tag{4.21}$$

This corresponds to an average gas gain G of:

$$G := \frac{N_{total}}{N_{primary}} = \frac{Q_{tot}/1.6 \cdot 10^{-19} C}{223} = 1.0 \pm 0.3 \cdot 10^4 \tag{4.22}$$

which is in agreement with the measurements of the gas gain in Ch. 7.
Concerning the active area of a single strip with respect to the lowest GEM foil as the responsible detector capacity C_{det} one gets:

$$C_{strip}^{GEM} = \frac{\varepsilon_0 \cdot A_{active \; strip}}{d_{ind \; gap}} = \frac{8.85 \cdot 10^{-12}(\text{F/m}) \cdot 0.002\text{m}^2}{3,0 \cdot 10^{-3}\text{m}} = 5.9 \text{ pF} \tag{4.23}$$

which results in a constant Q_{coup} since $C_{strip}^{GEM} \ll C_{coup}$.
The theoretical values for C_{strip}^{GEM} and C_{strip}^{PCB}, respectively, deviate from the experimental result at least by a factor of five. Further investigation of the involved capacities in the detector is needed. With the implementation of a highly segmented anode ("prototype 2.0") the low capacity range can be studied and is in preparation.

Chapter 5

Efficiency Determination

This chapter addresses the efficiency of prototype 1.0. Since the trigger scintillators cover a larger area than the active size of the detector one has to correct for a geometrical factor which is presented in Ch. 5.1. The efficiency of prototype 1.0 equipped with an unsegmented anode is illustrated in Ch. 5.2. With the installation of a flow and pressure control unit in the gas system as well as optimized operational voltage settings one obtains an optimized efficiency which is reported in Ch. 5.3.

The efficiency ε is defined as the ratio of recorded signals S over the sum of all triggering events S_{total}:

$$\varepsilon = \frac{S}{S_{total}} = \frac{N_{detected\ \ particles}}{N_{total\ \ particles}} \tag{5.1}$$

5.1 Efficiency Simulation

The measurement of the efficiency is realized by two scalers (cf. Fig. 3.9). One of them counts the triple coincidence between detector and the two trigger scintillators, the other counts the two trigger scintillators alone. The threefold coincidence of scintillator triggers combined with the GEM's signal is the real number of detected particles that are recorded by the FADC. Coincidence of the GEM surrounding scintillators gives the number of total particle that are crossing the active detection area. Since the surface of the two scintillators is about 40 % bigger than the detectors active area and taking their rectangular positioning into account, one has to correct the number of two-fold coincidences by the geometrical factor. A MonteCarlo Simulation is implemented to derive the real count rate of particle traversing the active area of the GEM detector or scintillators.
As illustrated in Fig. 5.1, the two scintillators are abstracted to rectangles, consisting of a lower and an upper plane. The GEM detector itself is represented by a simple plane, centered to the surface covered by both triggering detectors. For points placed in small equidistant steps on the lower and upper surface of *Sc1* a large number of muons is simulated with incident directions defined by the angles θ and ϕ. It was assumed that the incident angles are distributed as $f(\theta) = cos^2\theta$ and normalized for the ϕ - coordinate via $g(\phi) = 1/2\pi$. The values of the direction vector are transformed to Cartesian coordinates:

$$\begin{aligned} \text{direc}[0] &= \cos(\phi)\sin(\theta) \\ \text{direc}[1] &= \sin(\phi)\sin(\theta) \\ \text{direc}[2] &= \cos(\theta) \quad . \end{aligned} \tag{5.2}$$

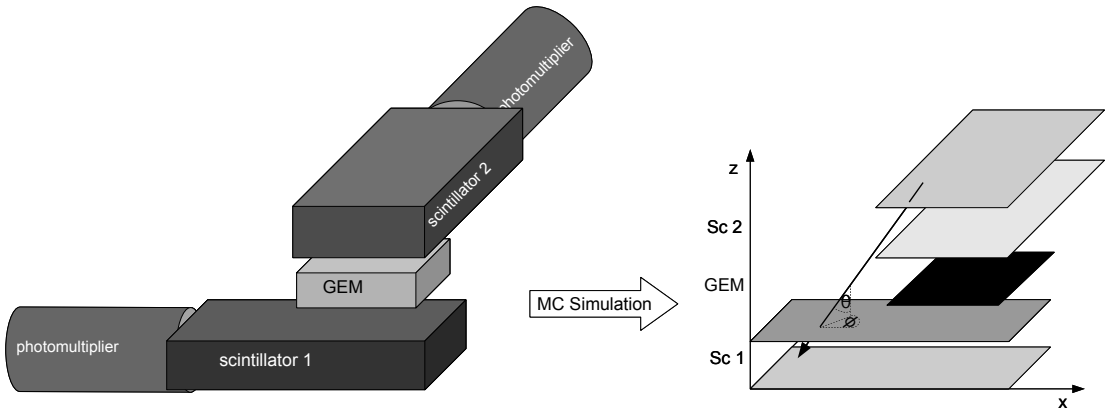

Figure 5.1: Schematics of the defined layers for simulation.

Normalizing this vector with respect to the z-axis defines the vector *check[i]* and $i \in [0,1,2]$:

$$\text{check[i]} = \frac{\text{direc[i]}}{\text{direc[2]}} \tag{5.3}$$

Starting with the detection point *posz* at the lower scintillator, the *check*-vector is extrapolated to the upper scintillators lower and upper surfaces, respectively.
If the endpoint of the track lays within the respective rectangle (see Fig. 5.2), the muon has crossed also the upper scintillator and will be tagged as an "upper scintillator hit". The same method can be applied to checking if this muon also hit the GEM detector. Then it is tagged as a "GEM hit" muon.

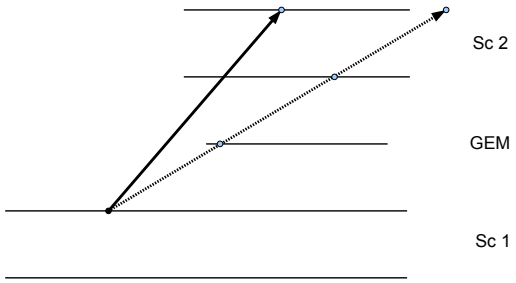

Figure 5.2: Cross section of the simulation model. The starting point of muons is on the lower scintillator *Sc1*.

Running this procedure for a large number of simulated events and taking the ratio of "GEM hits" over "upper scintillator hits", one receives the geometrical correction factor f_{corr} that has to be inserted in the efficiency calculation:

$$\varepsilon_{corr} = \frac{N_{detected\ \ particles}}{N_{total\ \ particles} \cdot f_{corr}} \tag{5.4}$$

Assuming an alignment of the two scintillators (cf. Fig. A.1 and Fig. A.2 within ±5 mm, the simulation yields for the correction factor of the efficiency a value of

$$\boxed{f_{corr} = 0.868 \pm 0.005} \quad . \tag{5.5}$$

In the following discussion this correction factor is considered when talking about efficiency.

5.2 Measurement with Unsegmented Anode

After construction and commissioning of the prototype 1.0, the first measurements of cosmic muons began in March 2010 with an unsegmented copper anode and readout by the *CATSA* preamplifier. As mentioned in Ch. 3.1.1 the GEM foils were conditioned to HV of ΔU_{GEM} around 300V see Tab. 5.1.

GEM foil number	1	2	3
Applicable ΔU_{GEMi} [V]	330 V	290 V	340 V

Table 5.1: Voltage rigidity of the GEM foils in the prototype 1.0 with unsegmented anode.

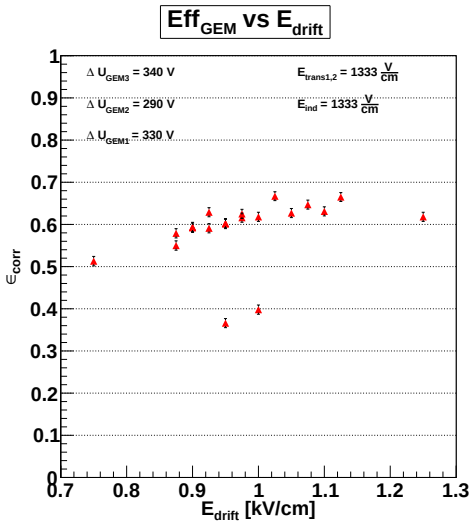

Figure 5.3: Efficiency as a function of the drift field E_{drift}.

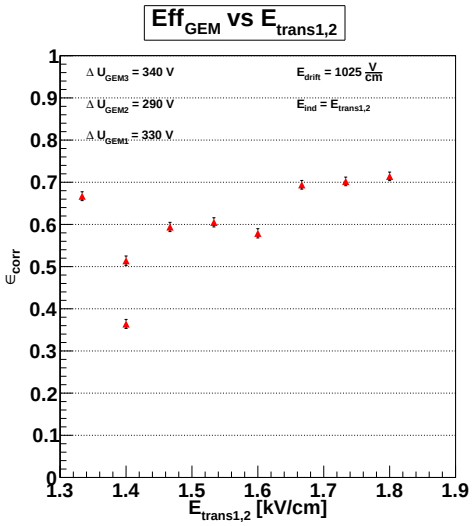

Figure 5.4: Efficiency as a function of increasing transfer and induction field $E_{trans1,2} = E_{ind}$.

Results of the first studies in March are shown in Fig. 5.3 and Fig. 5.4. Every data point represents a sample of $N_{sample} = 2000$ cosmic muon events. The statistical error is given by:

$$\Delta_{stat}.\varepsilon = \sqrt{\frac{\varepsilon \cdot (1-\varepsilon)}{N_{sample}}} \tag{5.6}$$

In order to find the optimal operation parameters with respect to the applied electric fields, voltage scans were done. By the plots presented in this chapter it was possible to determine a specific voltage setup for stable operation at highest efficiency.
The configuration of constant electric fields in the transfer gap and induction gap shows an improvement of the efficiency from 50% at low fields to about 65% in central range and slightly lower for the highest applied field in the drift region. Taking the the maximum of $E_{drift} = 1025$ V/cm and changing $E_{trans1,2}$ leads to Fig. 5.4. At $E_{trans1,2} = 1.80$ kV/cm the efficiency shows a maximum of 70% .
At that time the pressure and flow control unit was not yet implemented. Remarkable deviations of some measurements from the average (samples with $\varepsilon_{corr} \leq 0.4$) were recorded shortly after flooding the detector with gas.
Additionally, the spectrum recorded by the *CATSA82* preamplifier is cut off at low cosmic signals since its charge-to-voltage conversion factor is to low to separate the signals completely from the noise level (see Ch. 4.3). This problem is eliminated in further measurements by replacing the *CATSA82* by an *ELab* preamplifier with better performance.
A first step to stable operation conditions is done by the installation of the flow control unit *BROOKS 5850S* (cf. Ch. 3.3.2) resulting in efficiencies around 90%, see Fig. 5.6 - 5.7. Fig. 5.6 shows the variation of $E_{trans1,2} = E_{ind}$, the distributon is flat.
Analyzing the data involved in Fig. 5.7 illustrates that the optimal operation point with respect to $E_{trans1,2}$ and E_{ind} lies in the range of 2.00 kV/cm. The obvious increase of ε_{corr} with higher $E_{trans1,2}$ field strength is mainly due to the electric field line configuration. Since higher transition/induction fields mean catching more field lines from the upper region, namely the last amplification stage in the nearest GEM foil, more electrons are extracted from the holes and drifting along the field lines in direction of the anode structure. At lower fields more field lines exiting the gas amplifying GEM holes are ending on the lower electrode of the foil keeping the charges from being detected. As the pulse height of the signal is proportional to the number of readout charges, higher fields are equivalent to a better separation of the signal from the noise level and therefore resulting in better efficiency performance, see Ch. 4.3 and 4.4.

A voltage scan for the drift gap in Fig. 5.8 states an optimal E_{drift} of 1.25 kV/cm. The trend of efficiencies decreasing for drift fields of $E_{drift} > 1.25$ kV/cm is due to the decreasing pulse height as mentioned in Ch. 4.3 and Ch. 4.4.

Thus it is reasonable to run the detector with an arrangement of electric fields:

$$E_{drift} = 1.25 \text{ kV/cm} \quad \textit{and} \quad E_{trans1,2} = E_{ind} = 2.00 \text{ kV/cm} \quad . \tag{5.7}$$

5.3 Optimized Efficiencies

5.3.1 Modifications to Flow and Pressure

As it is shown in the previous section, one derives advanced conditions by controlled gas flow. By installing the pressure control unit in the gas line the preparations of a stable operation mode with respect to the gas system are completed (cf. Ch. 3.3). During this amelioration the segmented anode, consisting of five strips (cf. Fig.B.3), was also installed. In consideration to the fact that the first setup of GEM foils showed an unsatisfactory behavior in terms of HV rigidity limits we replaced the upper two GEM foils by new ones with better performance so that all implemented foils show a

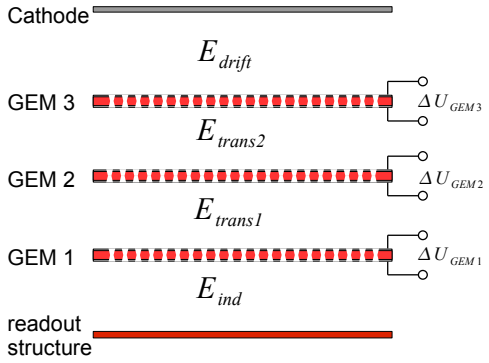

Figure 5.5: The triple GEM detector and its different field regions (repetition).

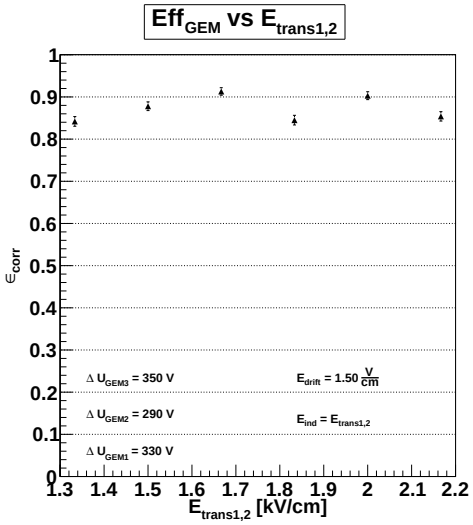

Figure 5.6: Efficiency scan for $E_{trans1,2} = E_{ind}$. The drift field is constant at $E_{drift} = 1.50$ kV/cm

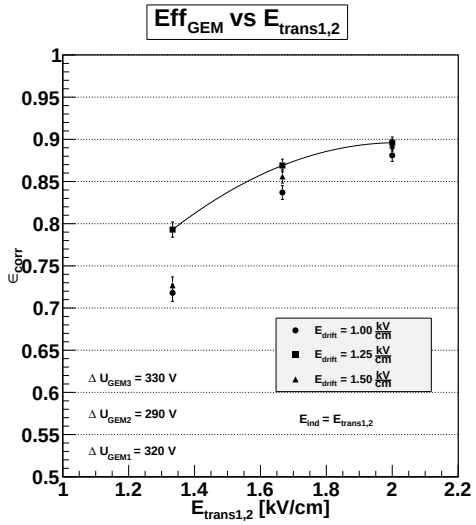

Figure 5.7: Efficiency dependence of $E_{trans1,2} = E_{ind}$ and three different E_{drift} fields.

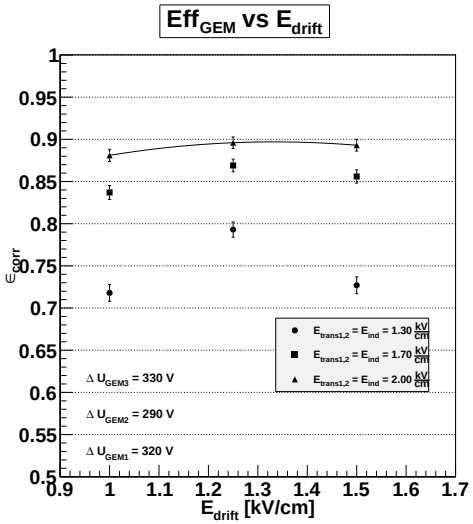

Figure 5.8: Efficiency dependence of E_{drift} for three different $E_{trans1,2} = E_{ind}$ fields.

breakdown voltage limit $\Delta U_{GEM}^{limit} \geq 360$ V.
Additional to this changing, the preamplifier *CATSA82* is replaced by an home-made *ELab*[1] preamplifier since it provides higher gains and faster rise time.

Testing the temperature influence could be realized by installing the triple GEM in an insulated box packed with cooling elements. Herefore it was necessary to insulate the HV supplies and all other electronic components against moisture for safety reasons. This lead to a worse noise performance in comparison to the normal setup which could not be eliminated and was accommodated with higher discrimination thresholds.

[1] **E**lectronics **Lab**oratory of the LMU Munich

5.3.2 Optimized Efficiency and Temperature Influence on Measurements

Since cascaded voltage differences applied to the foil stack decrease the discharge probability effectively, as reported in [Bach 02], we found that a configuration as displayed in Tab. 5.2 is the most stable in view of high gains and minimized discharge rates. With this setup stable operation of the detector in long term overnight-measurements is observed.

ΔU_{GEM1}	ΔU_{GEM2}	ΔU_{GEM3}	E_{drift}	$E_{trans1,2}$	E_{ind}
320 V	340 V	360 V	1.25 kV/cm	2.0 kV/cm	2.0 kV/cm

Table 5.2: Voltage or E-field setup in the prototype 1.0 with five-strip-segmented anode.

For studies of effects due to temperature, the detector was provided with a *Voltcraft* datalogger [Volt 07] to record temperature and moisture in the immediate vicinity of the triple GEM. In comparison to the laboratories room temperature $T_{room} \approx 28$ °C the cooler renders a nearly constant temperature of $T_{cooled} \approx 14$ °C. The triple GEM was placed in the box for some time before starting the record in order to ensure that the flushed gas takes the same temperature as the datalogger is recording. Measurements taken with normal and cooled decetor and gas setup are documented in Fig. 5.9 and Fig. 5.10.

Since almost 95% of the readout charges are generated by amplification in the undermost foil *GEM1*, it is obvious that a voltage variation with respect to the induction field E_{ind} should have a strong impact on the efficiency for field configuration reasons.

The measurement taken with the setup at room temperature shows an expected fast rise of more than 20% from small to medium electric fields, reaching the plateau at $E_{ind} \geq 1.66$ kV/cm with an efficiency:

$$\varepsilon_{corr} \geq 95\% \tag{5.8}$$

Voltage regions higher than $E_{ind} \geq 2.33$ kV/cm are not available as the discharge rate becomes unacceptably high in the order of $\mathcal{O}(\text{discharge}) \approx 1\text{min}^{-1}$ and the accompanying dead time of the detector after trips and restarts prohibits a successful data taking.
A similar behavior is observed for data from the cooled test stand setup. The efficiency can also be raised for 10% from small to medium induction fields but a plateau for higher E_{ind} is not visible due to strong fluctuations leading to an average close to 80%.
As a conclusion one can say that temperature influences are visible and therefore a temperature recording unit additional to flow and pressure control is recommended.

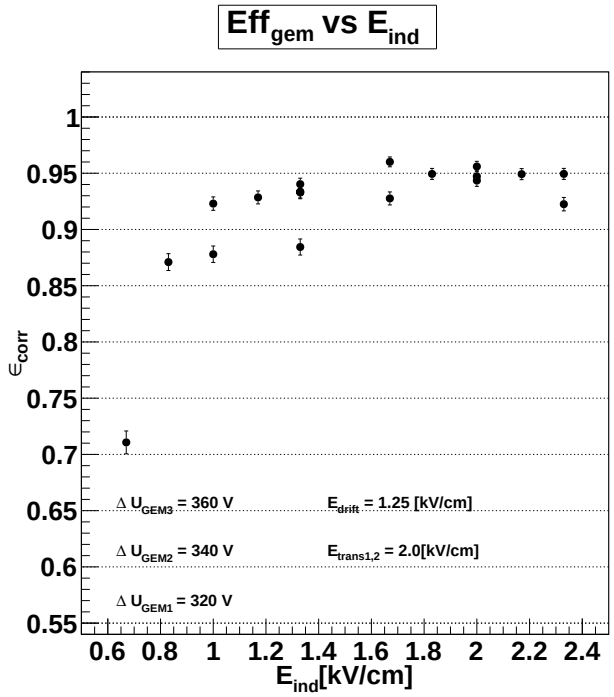

Figure 5.9: Efficiency as a function of E_{ind} with constant E_{drift} & $E_{trans1,2}$. The detector gas is at room temperature. $T_{detector} = T_{room} \approx 301$ K.

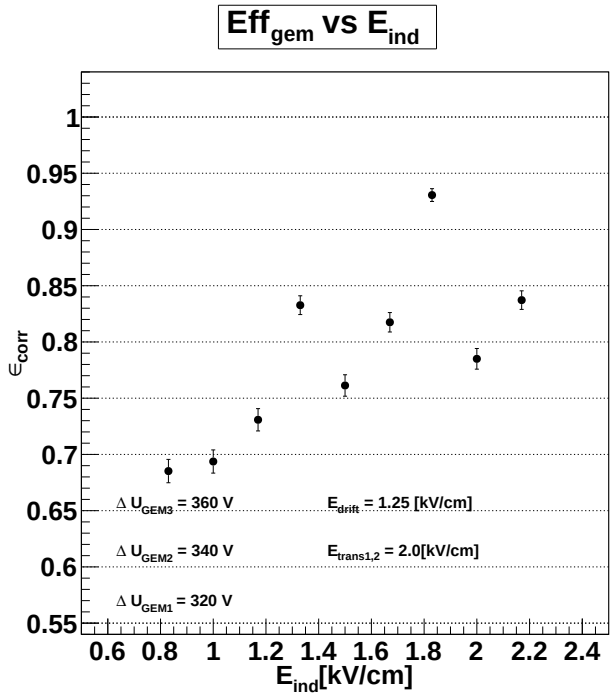

Figure 5.10: E_{ind} field scan with cooled detector and gas system. $T_{detector} \approx 285$ K.

Chapter 6

Rise Time Studies

For a better understanding of the signal creation in the GEM detector the rise time was studied in dependence on the operational parameters. This chapter starts with the time resolution of the prototype 1.0 and shows afterwards measurements done for electric field variations in the gap regions.

6.1 Time Resolution

The rise time can be determined via the inverse Fermi fit to the rising edge of the signal ($10\% - 90\%$ of the pulse maximum), as presented in Ch. 3.5. For investigation of the time resolution of the detector a localized primary charge distribution in the drift region is necessary. This includes analization of the electronics response using a temporarly defined pulse. For this analysis the charges generated by X-rays from the ^{55}Fe source can be used. Since the primary produced photoelectron loses its energy due to ionization of further atoms in a small range we can approximate the pulse as punctual in time and location. Fig. 6.1 and Fig. 6.3 show that such a point-like distributed charge generates a rise time of approximately 166 ns and 102 ns for signals recorded via the preamplifiers *CATSA82* and *ELab*, respectively. The Gaussian fits to the histogram of ^{55}Fe measurements present therefore good resolution, in addition as the detector is self-triggering. A resolution of these rise times as sharp as 7% and 2% for the *CATSA82* and *ELab* preamplifier, respectively, is thus given by default.

The cosmic ray muons, instead, produce electron-ion-pairs along their track while traversing the detector. Thus the charge produced by muons that is responsible for the signal creation is distributed over the whole drift region. The time between the first charges reaching the anode and the last depends on the drift velocity and the size of the drift gap.
Fig. 6.2 and 6.4 show the time resolution of exemplary data samples of cosmics recorded with the *CATSA82* as well as the *ELab* preamplifier. The rise time resolution is 26% and 20% for the individual preamplifiers.
The drift velocity of the electrons was determined by a GARFIELD/MAGBOLTZ simulation. In this simulation a parallel plate field is assumed ignoring the field configurations near the GEM foils (see Fig. 6.5). The program calculates the drift velocity in a given gas mixture, pressure and temperature for the indicated geometries. This results, for instance, in a drift time for electrons from the upper end of the drift region to the uppermost GEM foil of $t_{drift} = 99.5$ ns for a electric field of $E_{drift} = 1.25$ kV/cm, as it is drawn in Fig. 6.6.

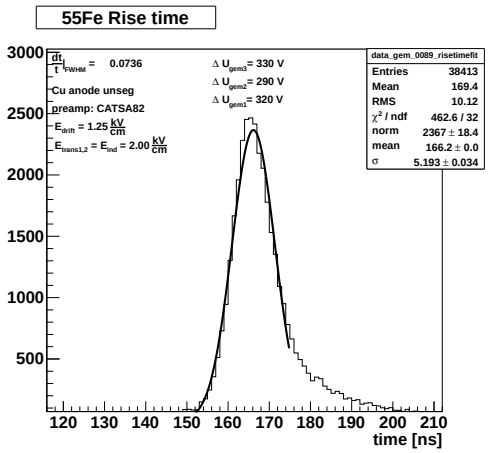

Figure 6.1: Rise time distribution for the K_α peak measured with *CATSA82*.

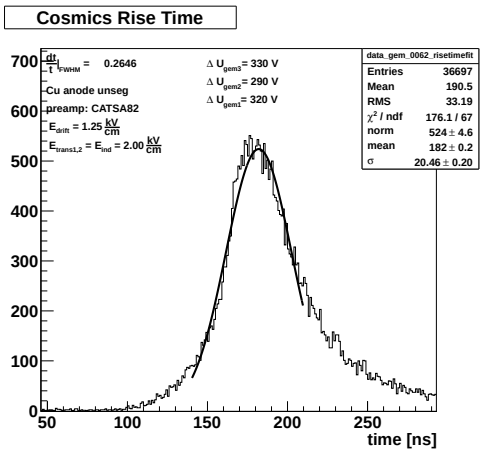

Figure 6.2: Rise time distribution for cosmic muons recorded via *CATSA82*.

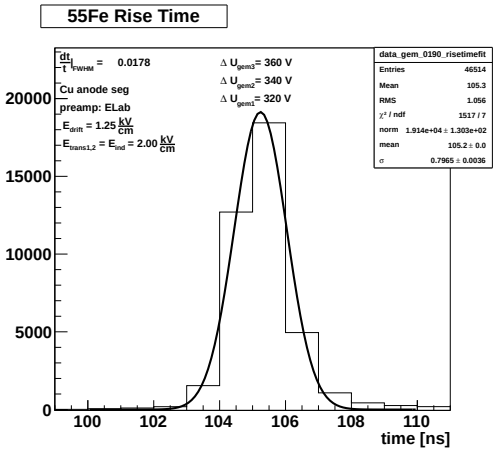

Figure 6.3: Rise time distribution for the K_α peak measured with the *ELab* preamplifier.

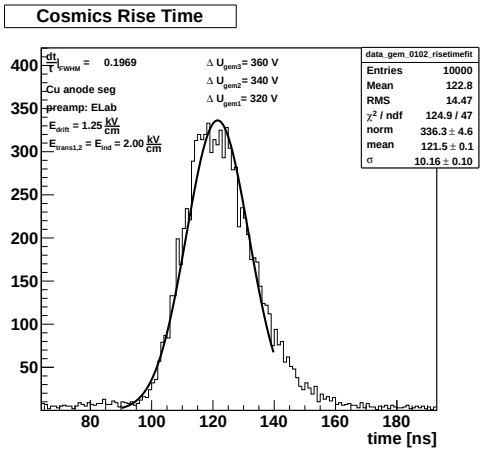

Figure 6.4: Risetime Resolution of cosmic muons recorded via *ELab*.

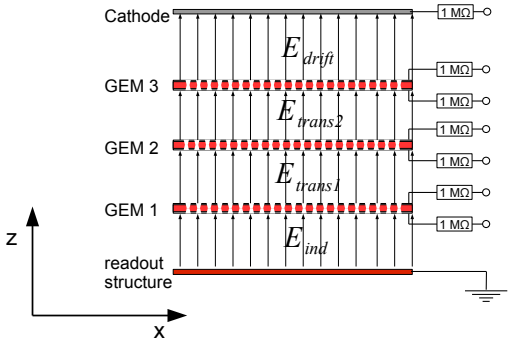

Figure 6.5: Parallel plane field line configuration in the detector for drift velocity simulation.

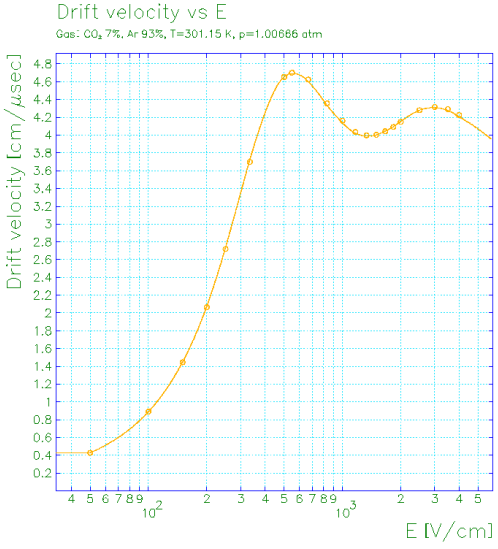

Figure 6.6: Electron drift velocity in $Ar/CO_2 = 93/7$ at 1020 mbar and room temperature.

The signal by cosmic muons can now be seen as a set of locally discrete charges distributed over the entire drift region. To this end we consider the maxima in the rise time histograms shown earlier as the width of an associated probability distribution of all signal times. In the case of X-ray generated events the shown signal time represents the width σ^t_{local} of locally produced charges that is smeared out due to diffusion effects. Furthermore, the drift time of electrons in 4 mm drift space characterizes the width σ^t_{drift} of a corresponding probability function if one considers all realizable drift times. Following this argument, the combination of these statistically distributed signal and drift times results in the signal rise time σ^t_μ of muon events. Mathematically, this is implemented by the convolution of the corresponding distribution relating the standard deviations quadratically:

$$\sqrt{(\sigma^t_{local})^2 + (\sigma^t_{drift})^2} = \sigma^t_\mu \tag{6.1}$$

Considering signals recorded with the *CATSA82* preamplifier and operation parameters as in Fig. 6.1 and Fig. 6.2 one derives theoretically rise times that are shown in Tab. 6.1. Additionally, the experimental results and the the characteristics of the used preamplifiers are denoted.

Preamplifier	X-ray: mean rise time$[ns]$	Cosmics: mean rise time $[ns]$	Cosmics: theoretical rise time $[ns]$	C_{coup} $[nF]$	Preamplifier: rise time $[ns]$
CATSA82	166.2	182	194	50	10
ELab	105.2	121.5	145	1.5	10

Table 6.1: Mean rise time for Cosmic and X-ray measuements with *CASTA82* and *ELab* preamplifier, respectively. The theoretically derived rise times are also shown. The preamplifier characteristics C_{coup} and rise time are required for following considerations.

Both theoretically derived approximations overestimate the experimental result slightly. This might be an effect of the simplified field configurations used in the simulation of drift velocities. By reversing the above stated equation one derives an experimental average value for the drift velocity of electrons of 5.4 cm/μs and 6.6 cm/μs both representing the drift in an electric field of $E_{ind} = 1.25$ kV/cm. The MAGBOLTZ simulation yields a drift velocity 4 cm/μs. Nevertheless, the estimation reproduces the correct range and it is assumable that the signal rise time of cosmic muon events can be considered as an ensemble of single localized charge clusters distributed over the complete drift space.
Now the question arises how these signal rise times of ^{55}Fe measurements are created. The data for locally limited generated charges recorded via the *CATSA82* preamplifier show a mean rise time that is 60 ns longer than samples taken with the *ELab* preamplifier for an equal setup of fields between the GEM foils. Thus one can conclude that the total signal rise time for ^{55}Fe events is not only based on the presence of liberated charges in the detector but also depending on the connected electronics. It is assumed that the rise time distribution recorded with the *ELab* preamplifier represents the real rise time accurately. The rise time of the *CATSA82* preamplifier is limited due to its big coupling capacity C_{coup} which can be shown with the following consideration. Assuming that the signal line contributes an effective output resistance $R = 2.5\Omega$ would lead to an internal rise time τ of the preamplifier:

$$\tau = R \cdot C_{coupl} = 2.5\Omega \cdot 50 \text{ nF} = 125 \text{ ns} \tag{6.2}$$

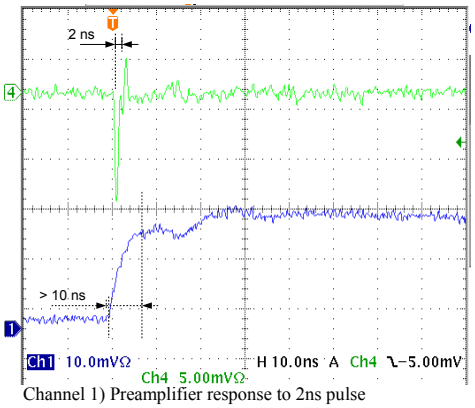

Channel 1) Preamplifier response to 2ns pulse
Channel 4) Scintillator pulse exiting differentiating circuit

Figure 6.7: Response of the *CASTA82* preamplifier to a δ - shaped pulse of 2 ns width.

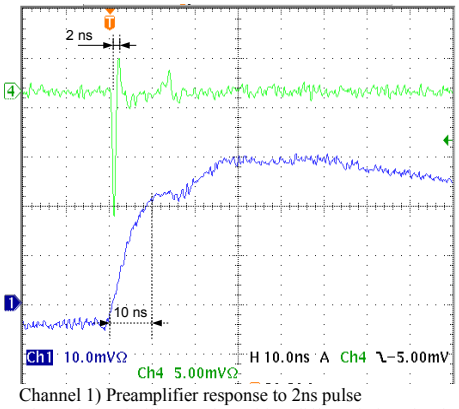

Channel 1) Preamplifier response to 2ns pulse
Channel 4) Scintillator pulse exiting differentiating circuit

Figure 6.8: Response of the *ELab* preamplifier to a δ - shaped pulse of 2 ns width.

for the *CATSA82* preamplifier and

$$\tau = R \cdot C_{coupl} = 2.5\Omega \cdot 1.5 \text{ nF} = 3.75 \text{ ns} \tag{6.3}$$

regarding the *ELab* preamplifier. This estimation shows that the *ELab* preamplifiers rise time is negligible whereas the big coupling capacity of the *CATSA82* preamplifier affects the rise time distribution significantly.

In order to analyze the internal response time of the preamplifiers a δ-like pulse of 2 ns width and 10 mV maximum pulse height is fed to the input. Since the trigger scintillators provide a frequent signal we can use this as a pulse generator. Combined with a discriminator and dual timer as already used in the conventional readout, see Ch. 3.4.1, the resulting box-shaped pulse is fed to a differentiating circuit. This setup supplies the narrow pulse which can be seen in Fig. 6.7 and Fig. 6.8 together with the response of the two preamplifiers. In this manner the internal rise time of the preamplifiers is determined to approximately 10 ns for both (see channels no. 1 in the corresponding Fig. 6.7 and 6.8). The differentiating circuit transfers the scintillator pulse to a sharp negative pulse followed by a smaller overshoot that is repeated around 14 ns after the main pulse. The overshoot with 2 ns delay after the main pulse is not resolved by the preamplifiers. A plateau of the rise time is reached in 10 ns after the main pulse. The second small positive pulse of the test signal gives a second rise to the preamplifier response. The *CATSA82* preamplifier shows a slightly faster response to the δ - shaped pulse than the *ELab* preamplifier whose amplitude is 50% higher, in contrast.
This rise time is negligible in comparison to the 100 ns electron drift time and the ^{55}Fe induced rise times around 106 or 166 ns.

6.2 Rise Time Dependence on Induction - Field

In order to understand the signal rise time formation, data were taken in dependence of the E-field on the induction gap with the X-ray source as well as with cosmic ray muons. This is motivated by the estimate that the detectable pulse begins with the presence of the amplified charges at the lower

electrode of the undermost foil *GEM1* resulting in an induced pulse on the anode.
For these measurements the data was supplied to the flash ADC via the home-made *ELab* preamplifier since it shows less internal response time and higher gain than the *CATSA82*.

6.2.1 ^{55}Fe Measurement with E_{ind}- Field Variation

The iron source was placed centrally on the active area of the detector and the induction field was varied in a range of $0.05\ \mathrm{kV/cm} \leq E_{ind} \leq 2.33\ \mathrm{kV/cm}$ for each data sample of $N_{sample} = 50 \times 10^3$ events (see Fig. 6.9).

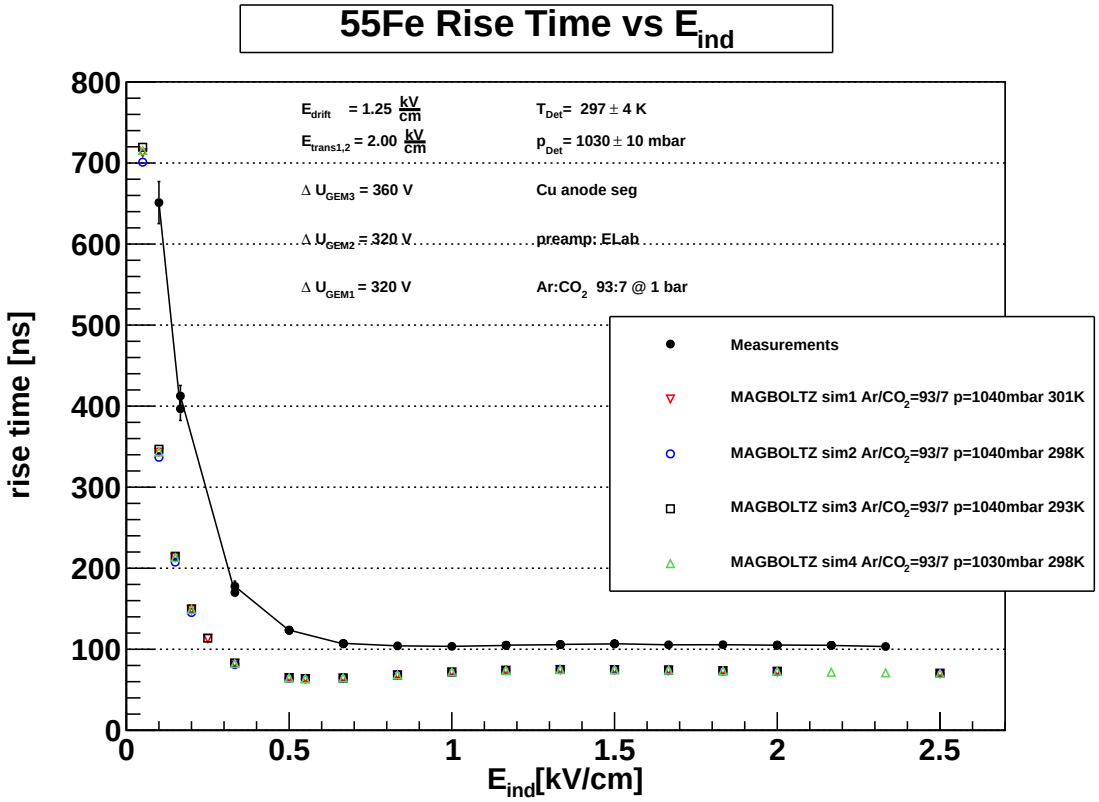

Figure 6.9: ^{55}Fe signal rise time as a function of E_{ind}. (Data is indicated by black dots and guiding line). MAGBOLTZ simulations for drift time of electrons in 3 mm induction gap are plotted (see legend). Concerning also the intrinsic rise time of the preamplifier results in a good approximation for the plateau at high fields (red crosses and green triangles).

The accessible range is limited by frequent discharges at fields $E_{ind} > 2.33\ \mathrm{kV/cm}$. A closer look at Fig. 6.9 shows that the signal rise time starts at approximately 650 ns (indicated by the black dotted data points in the figure). Increasing the induction field strength results in an exponential decrease reaching a plateau of 100 ns rise time at around $0.8\ \mathrm{kV/cm}$. The rapid drop in signal rise time is due to the increase in drift velocity over one magnitude for at $0.05\ \mathrm{kV/cm} \leq E_{ind} \leq 0.8\ \mathrm{kV/cm}$ (see Fig. 6.6). However, in the area of the plateau the variation of the drift velocity with field strength is no longer strong; it is only of about 10%. To illustrate this the drift times of electrons from the lowest foil *GEM1* to the anode are simulated with MAGBOLTZ and additionally plotted in the figure. It is

observed that slight changes in temperature and pressure have no effect on the simulated drift time. The drift time of electrons in the 3 mm wide induction gap reaches an average value of $t_{drift} \approx 70$ ns in the range of 0.8 kV/cm $\leq E_{ind} \leq$ 2.3 kV/cm. The preamplifier's intrinsic rise time, that is determined to 10 ns in the previous section, was found to be negliglible thus the theoretically derived rise time $t_{signal}(theo.)$ for X-ray signals in the considered E-field range is:

$$t_{signal}(theo.) \approx 70 \ ns \tag{6.4}$$

This result underestimates the data that provide an average rise time $t_{signal}(exp.)$ in the plateau region for $E_{ind} \in [0.8 \cdots 2.3\text{kV/cm}]$:

$$t_{signal}(exp.) \approx 100 \ ns \quad ; \tag{6.5}$$

and is assumed to result from diffusion of the point-like distributed charge in the drift gap.
On the other hand, there are also ions liberated in the amplification process in the GEM foils. The ions drift from inside the holes along the field lines to the upper foil electrode. A potential difference of $\Delta U_{GEM1} = 320$ V is identical to an average electric field in the hole of $E_{hole} \approx 53$ kV/cm. With the mobility of ions in Argon $\mu^+ = 1.7$ cm^2/Vs for Argon ions and slightly higher for CO_2^+ ions $\mu^+ = 1.72$ cm^2/Vs, respectively. Thus one can consider an average maximal drift time t^+_{drift} of ions to the upper *GEM1* electrode of:

$$t^+_{drift} = \int_{GEM1 \ low}^{GEM1 \ up} \frac{dz}{E_{hole} \cdot \mu^+} \approx \frac{60\mu m}{1.7\frac{\text{cm}^2}{\text{Vs}} \cdot 53\frac{\text{kV}}{\text{cm}}} = 66 \text{ ns} \quad . \tag{6.6}$$

Due to the higher fields in the GEM foil and shorter drift distance the thousand times smaller mobility of the ions results in a drift time comparable to that of the electrons to the readout structure. Although the simulations underestimate the true measured drift times, it is visible that the signal rise time follows the trend of electron drift times to low electric fields. If it were mostly due to the ion cluster feedback the signal rise time would be more constant since the electric field in the holes, that accelerates the ions, is not changed.

Thus the drift of the charge cluster from the lower side of *GEM1* towards the anode structure is responsible for the signal creation. Similar results were found by [Gued 03] in a double GEM detector using current sensitive preamplifiers.

6.2.2 Cosmic Muon Measurement with E_{ind}- Field Variation

Fig. 6.10 shows the rise time for cosmic muon induced signals as a function of E_{ind}. The low field range $E_{ind} \in [0.05; 0.8\text{kv/cm}]$ from Fig. 6.9 was not available. As mentioned in Ch. 4.4.2 the lower limit of the field range is determined by the noise level and discharges determine the highest fields. At the minimal reasonable field strength of $E_{ind} = 0.8$ kV/cm the rise time reached already the plateau. Again, we assume the electron drift time in the induction gap with about 70 ns. A convolution of the drift times of electrons in the drift gap with an $E_{drift} = 1.25$ kV/cm, the induction gap with $E_{ind} = 2.0$ kV/cm and the intrinsic rise time of the charge sensitive preamplifier yield:

$$\sigma^t_\mu = \sqrt{(\sigma^t_{local})^2 + (\sigma^t_{preamp})^2 + (\sigma^t_{drift})^2} = \sqrt{(70^2 + 10^2 + 100^2)} \approx 122 \text{ ns} \quad . \tag{6.7}$$

This is in accordance with the average measured signal rise time $t_{signal}(exp.)$ for cosmics at identical field configuration:

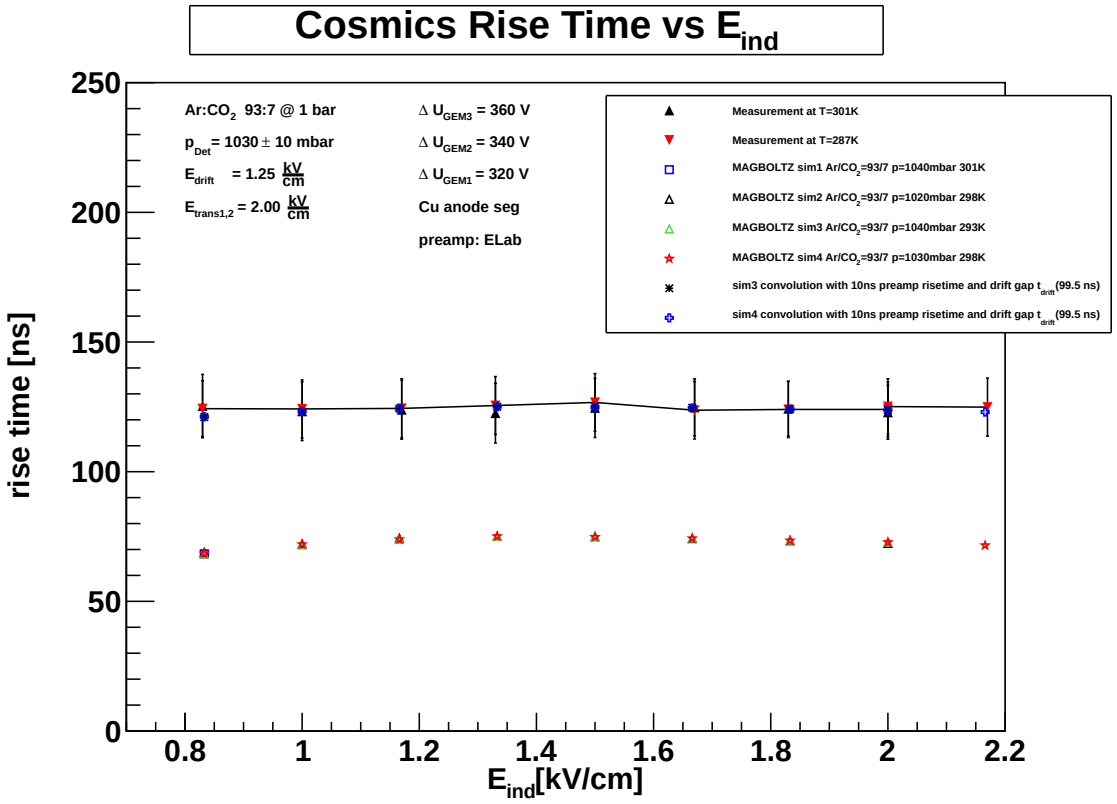

Figure 6.10: Signal rise time of comic ray muons as a function of the induction field E_{ind}. Data sample for two different gas temperatures are taken (triangles in the plot). Additionally, simulations of electron drift times in AR/CO_2 at various pressures and temperatures are plotted (below measurements). These drift times combined with the preamplifier's intrinsic rise time and convoluted with an simulated drift time of approximately 100 ns in the drift gap results in the points in the data error range.

$$t_{signal}(exp.) = 124 \text{ ns} \ . \tag{6.8}$$

Chapter 7

Gas Gain Studies

This chapter describes the gas gain of prototype 1.0 filled with a gas mixture of Ar/CO_2 at the ratio $93/7$.

7.1 Gain Studies for Ar/CO_2 at $93/7$

The gas gain G is defined as the ratio of total created charge over primary charge in the detector. Due to recombination and electron transparency it is possible that not all liberated electrons in the triple GEM detector reach the anode. Furthermore, not all charges that reach the anode contribute to the recorded pulse due to voltage equalization on C_{det} and C_{coup} (see Ch. 3.4.3). Thus it is more reasonable to use the expression *effective gas gain* G_{eff} [Bach 99]:

$$G := \frac{N_{total}}{N_{primary}} = \mathrm{e}^{\alpha x} \quad \overset{chargelosses}{\longrightarrow} G_{eff} = \frac{N_{signal}}{N_{primary}} \tag{7.1}$$

where N_{signal} corresponds to the fraction of created charge Q_{coup} reaching the coupling capacitor C_{coup} of the preamplifier:

$$N_{signal} \cdot e =: Q_{coup} \tag{7.2}$$

with the elementary charge $e = 1.6 \times 10^{-19}$ C. The gain depends on various parameters as the gas pressure and temperature, the gas itself and on the applied voltages as well as the geometry of the GEM holes. As stated in Ch. 1.2.4 the gain is exponentially depending on the thickness of the amplification gap x in Eq 7.1. The first Townsend coefficient α is directly proportional to the applied fields [Leo 94]. To determine the effective gain we used the K_α line of the ^{55}Fe source. The amount of detected charges N_{signal} is taken from the mean value of the Gaussian fit to the histogram (cf. Ch. 4.1):

$$N_{signal} = \frac{U_{out}}{F_{\mathrm{CV}} \cdot e} = \frac{K_\alpha \mathrm{mean} \cdot m_{ADC}}{F_{\mathrm{CV}} \cdot e} \tag{7.3}$$

where F_{CV} is the charge-to-voltage conversion factor, i.e. the internal amplification of the preamplifier and m_{ADC} the scaling factor of the flash ADC, 0.244 mV per ADC channel. The estimated error ΔN_{signal} corresponds to the standard deviation σ of the fitted K_α peak in the same way.

Data were taken with a centrally placed irradiation source and readout via the *Canberra2004* preamplifier with the tabulated conversion factor $F_{\mathrm{CV}} = 1$ V/pC. The temperature and pressure were held constant at $T = 296 \pm 1$ K and $p = 1020 \pm 10$ mbar, respectively. It can be seen that the effective

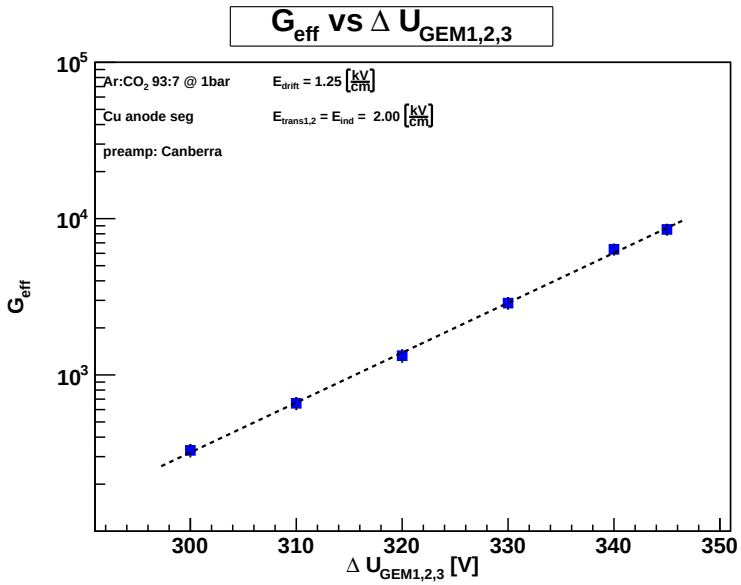

Figure 7.1: Effective gain of the prototype 1.0 as a function of voltage difference at the GEM foils. The voltages were chosen to be identical at all three foils.

gain increases exponentially with higher fields in the GEM holes. This illustrates the exponential dependence on the first Townsend coefficient stated in equation 7.1. A maximum $U_{gem} = 345$ V could be applied before discharges occurred too often for further stable operation. In this setup a maximum gain of :

$$G_{eff} = 8.5 \times 10^3 \tag{7.4}$$

is observed.
These operation parameters were used to calibrate the *ELab* preamplifier. Repeating the set of measurements with this preamplifier and comparing the pulse height spectra results in an average charge-to-voltage conversion factor F_{CV} for the *ELab* preamplifier of:

$$F_{\mathrm{CV}}(ELab) = 0.83 \pm \ 0.04 \frac{\mathrm{V}}{\mathrm{pC}} \tag{7.5}$$

and is shown in Fig. 7.2.

Using this calibration is was possible to evaluate the data taken with the *ELab* preamplifier. Fig. 7.3 shows measurements recorded with the *ELab* preamplifier with voltages cascaded to each other as well as identical $\Delta U_{gem1,2,3}$. In the first case the voltages were chosen with respect to foil GEM2 with GEM1 being 10% less and GEM3 being 10% higher in voltage.
In a cascaded setup slightly less gain in observed before reaching the limit of frequent discharges.
In this set of measurements with the *ELab* a $\Delta U_{GEM} = 350$ V were applicable thus resulting in a maximum gain that is:

$$G_{eff} = 1.0 \times 10^4 \ . \tag{7.6}$$

These results are in agreement with observations reported by [Bach 02] for a triple GEM detector in a Ar/CO_2 gas mixture at a ratio of $70/30$.

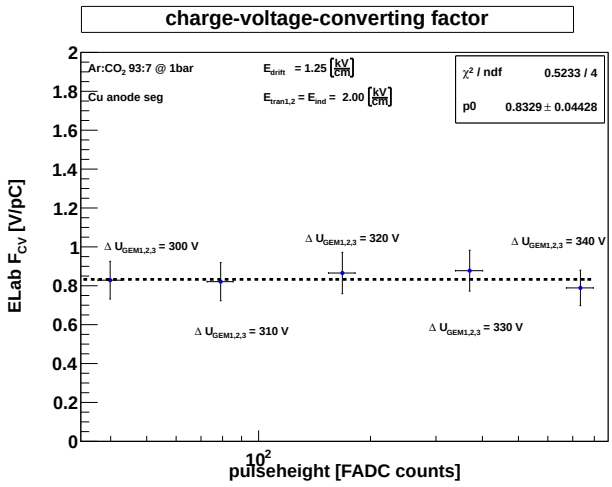

Figure 7.2: Charge-to-voltage conversion factor F_{CV} of the *ELab* preamplifier. Evaluated by comparison of pulse height spectra of the K_α line recorded with the *Canberra 2004* preamplifier.

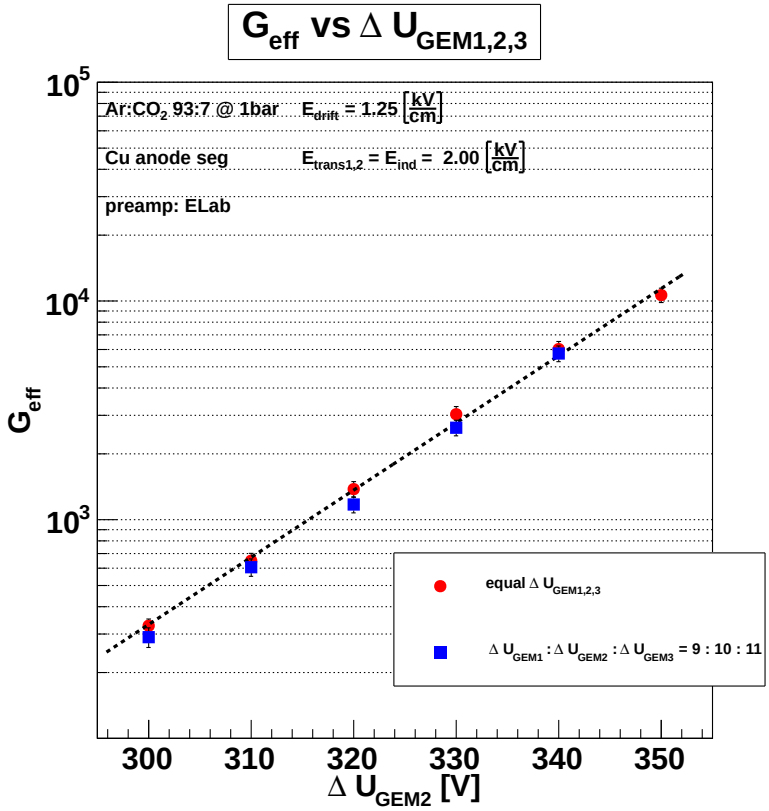

Figure 7.3: Effective gain as a function of ΔU_{GEM2}. Measurements with cascaded voltages at all three GEM foils in the ratio 9 : 10 : 11 as well as equal voltages at all foils are presented. Data was recorded via the *ELab* preamplifier

Chapter 8

Implementation of Highly Segmented Strip Readout

This chapter documents the construction of a triple GEM prototype 2.0 with highly segmented anode. The design of the detector is shown in Ch. 8.1. Two different readout systems are implemented. A readout based on the charge integrating 16 channel GASSIPLEX chip is illustrated in Ch. 8.2. The implementation of a readout based on 128 channel APV25 chips is reported in Ch. 8.3

8.1 Design of the Prototype 2.0

For the investigation of high spacial resolution a complete new detector was designed.

8.1.1 The Highly Segmented Anode

Fig. 8.1 shows a picture of the high-segmented anode. The anode has an overall surface of 250 $\times$ 360 mm^2. In the multi layer production process it was possible to integrate the HV supply lines in the board for reduction of passive material in the detector volume. We implemented three different designs for the active area of the detector. The micro strips of all three PCBs have equal dimension of 150 μm width and 250 μm pitch. They are made of copper and covered with a 5μm thick lead-free tin layer. For the readout based on GASSIPLEX chips we have chosen an active area of 90 $\times$ 100 mm^2 (Fig. 8.1) as well as a the total achievable active area of 100 $\times$ 100 mm^2. The detection area of an anode based on APV25 readout is 96 $\times$ 100 mm^2. In every version of the readout PCB the active area is surrounded by a grounded top layer; a grounded bottom layer provides shielding. Tab. 8.1 summarizes the dimensions and numbers of strips of the different readout systems with GASSIPLEX and APV25 frontend modules (FE), respectively. The different readout systems are explained in the following sections.

PCB for readout with	6 GASSIPLEX FEs	7 GASSIPLEX FEs	3 APV25 FEs
active detector area	0.0090 m^2	0.0100 m^2	0.0096 m^2
Number of strips	360	400	384

Table 8.1: Dimension and numbers of micro strips of the PCB anode designed for readout systems based on GASSIPLEX and APV25 frontends.

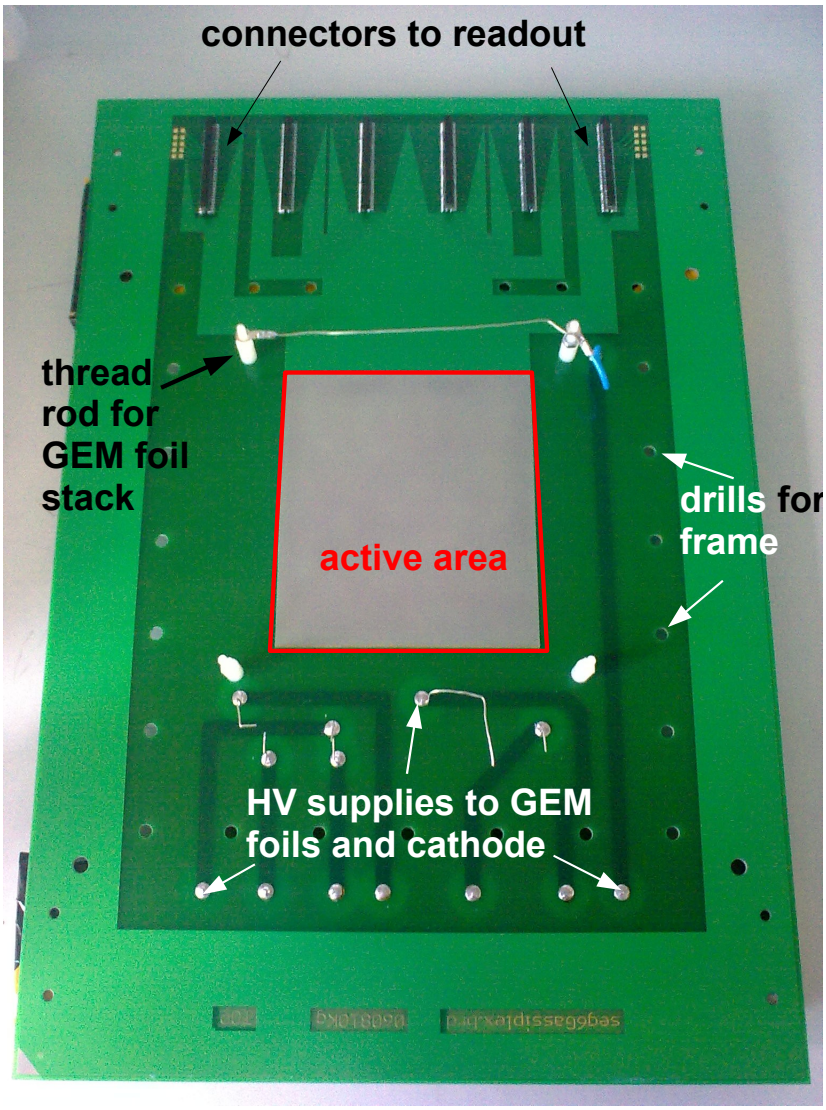

Figure 8.1: Top view of the readout PCB. Shown is the GASSIPLEX based readout anode with six frontend modules (see Ch. 8.2). Solder contacts with mounted copper wires for HV supply are visible at the bottom. Thread rods at each corner of the active detector area are installed for support of the triple GEM foil stack and the cathode. Connectors to the readout are shown on top. The active area (gray area in the picture) of $90 \times 100\text{mm}^2$ is segmented by 360 strips of 150 μm width and 250 μm pitch. The green layer surrounding the active area is the solder mask.

8.1.2 The GEM Stack

In contrast to prototype 1.0 the gap sizes are reduced in this detector by 1mm. We implemented a triple GEM foil stack with each foil at a distance of 2 mm covered by the 3 mm distant cathode, as it is shown in Fig. 8.2. The cathode, like in prototype 1.0, is made of a 36μm thick aluminized *mylar* foil.

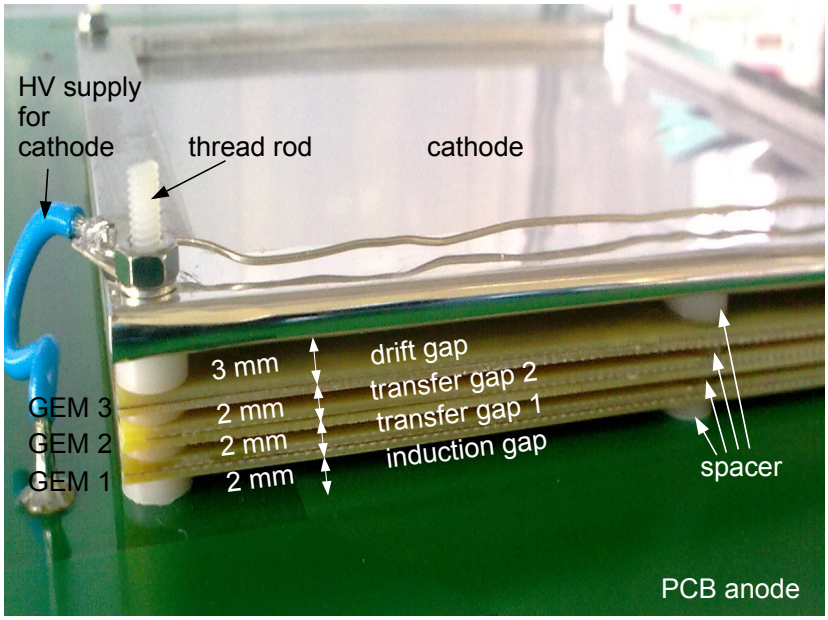

Figure 8.2: Side view of the triple GEM stack and the cathode in the prototype 2.0. The drift gap is 3 mm, the transfer gaps and the induction gap are 2 mm wide. The HV supply for the cathode (blue wire) soldered on the PCB (green layer) is visible.

8.1.3 Detector Housing

For noise reduction the frame of prototype 2.0 is built of aluminum, see Fig. 8.3. The enclosed volume is $25 \times 145 \times 170\text{mm}^3 = 0.62\ l$ and thus smaller than in the previous detector making divider walls unneeded. A top plate of 2 mm thick aluminum has five inlets for X-ray applications (Fig. 8.4).

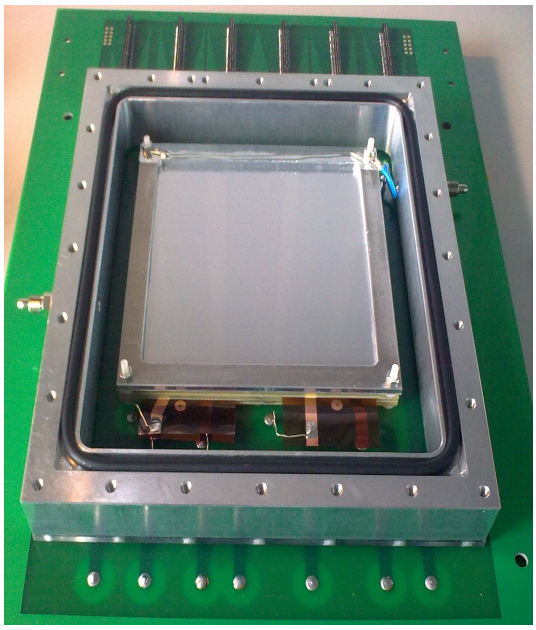

Figure 8.3: Top view of the opened prototype 2.0. The frame is made of aluminum. It includes a gas volume of $25 \times 145 \times 170\text{mm}^3 = 0.62\ l$.

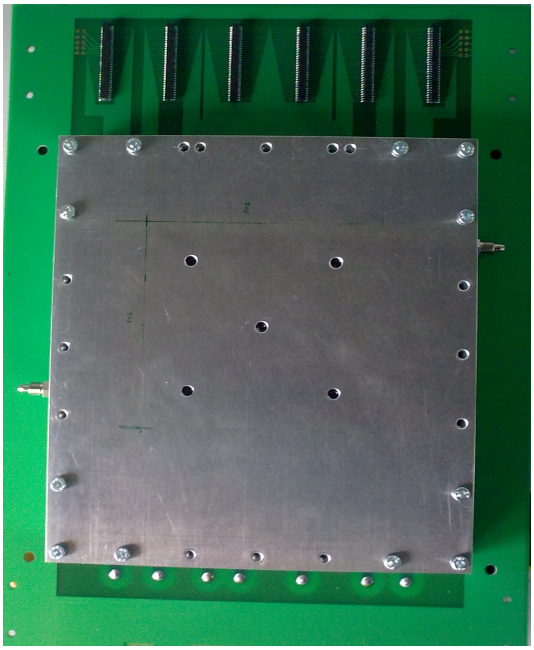

Figure 8.4: Top view of prototype 2.0. As in prototype 1.0 the cover plate is realized with ^{55}Fe X-ray inlets.

8.2 Prototype 2.0 with GASSIPLEX Based Readout

A possibility to simultaneously read out all strips is to use a system based on the GASSIPLEX [Beus 94] frontend modules. Originally it was designed for the HADES[1] RICH[2] [Zeit 99]. In this experiment it was implemented to read out 28500 pads on the backside of the detector. A detailed explanation of the readout system can be found in [Bohm 99].
By courtesy of the *E*12 department of the Technical University of Munich this system was modified by J. Bortfeldt for the readout of a MICROMEGAS[3] detector [Bort 10].
In this section a brief summary of adaptions from the MICROMEGAS readout electronic system to the triple GEM prototype 2.0 will be given. Fig. 8.5 shows a schematic of the whole readout chain.

8.2.1 The Readout Chain

The frontend modules consist of four GASSIPLEX chips containing 16 channels each. Every channel exhibits a charge sensitive preamplifier, a shaper and a track-and-hold circuit in the analog part. This is followed by a digitization part with a 20MHz sampling ADC on the frontend board and described in detail in [Bort 10]. For the prototype 2.0 with a PCB anode containing 360 micro strips, six frontend modules are needed, four of them being completely connected and two contributing 52 channels each. Protection circuits on the FEs are only capable of handling positive discharges since this was the requirement in the HADES experiment. The signals as well as discharges in the triple GEM detector are negative and an additional protection circuit has to be implemented to prevent potential damage

[1] **H**igh **A**cceptance **DiElectron S**pectrometer at GSI Darmstadt
[2] **R**ing **I**maging **Ch**erenkov detector
[3] **Micro Me**sh **Gas**eous detector

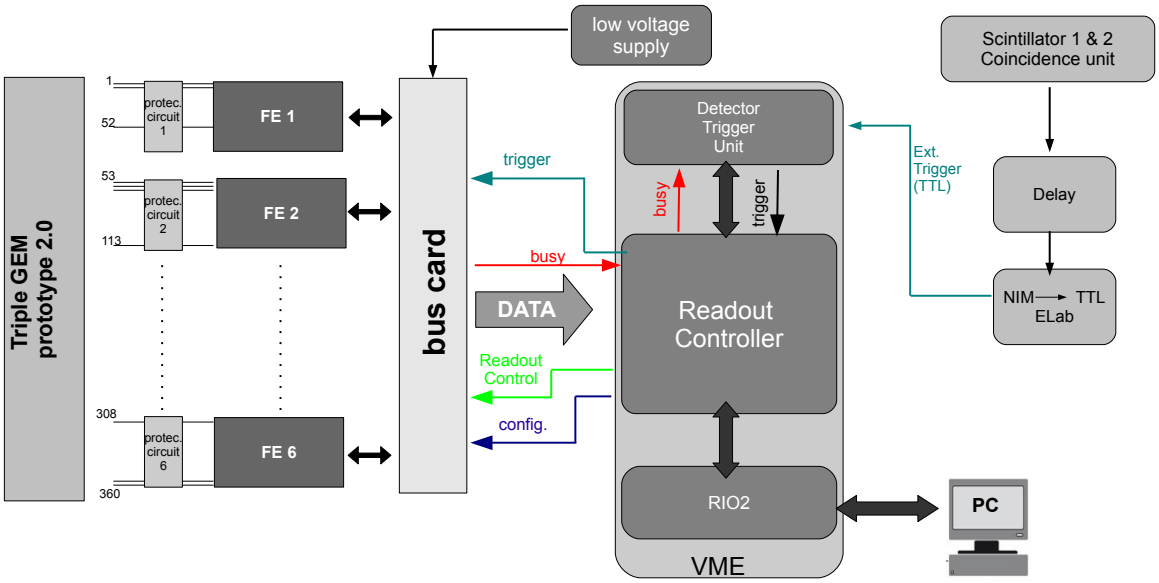

Figure 8.5: Schematic of the components for the readout system based on GASSIPLEX ASICs. The frontend modules are connected to the detector via additional protection circuits on the left. The data is further processes via bus cards to the readout controller. The coincidence of the scintillators provides the trigger [Bort 10].

of the electronics. A temporal storage of up to 15 events is possible on the FEs. Since no internal trigger exists on the frontend modules the data is readout if the readout controller (RC) receives a trigger from the detector trigger unit and transmits it to the FEs via the bus cards. The low voltage of the frontends is supplied by an external module. In Fig. 8.5 the bus cards are only schematically shown; in reality two bus cards are needed to readout the detector since four FEs are supplied by one bus card. Additionally, the readout controller is responsible for the frontend configuration and sets e.g. the mapping of the channels and thresholds of the individual channels. The detector trigger unit receives an external trigger, created in the conventional trigger scintillator coincidence, as already used in the setup of prototype 1.0 (see Ch. 3.4.1). Since the GASSIPLEX frontends have an intrinsic shaping time of 550 ns acting as a delay, the trigger has to be transmitted 550 ns after the particle's passage trough the detector system.
This assembly was implemented during the last days of this thesis. The GEM prototype 2.0 was in a table top setup with three MICROMEGAS detectors in order to build a stand alone tracking station for cosmic muons. Recent measurements reveal a spatial resolution of

$$79 \pm 5\mu m \quad . \tag{8.1}$$

The spatial resolution is limited by multiple scattering of the mostly low energetic cosmic muons and is expected to become considerably better in a high energy muon beam [Bort 10].

8.3 Prototype 2.0 with APV25 Based Readout

In this section the readout system based on the APV25[4] chip is presented. We use the APV25 frontend modules (FE) as they are designed for the triple GEM detectors installed in the COMPASS experiment. Fig. 8.7 shows a picture of the COMPASS APV25 frontend module. The supply and readout of the FE was designed in cooperation with HISKP Bonn.

8.3.1 The COMPASS APV25 Frontend Module

The APV25 [Jone 01] is a chip originally designed for the silicon tracker of the CMS detector at the LHC at CERN. The chip is capable to read data from 128 channels each equipped with a shaper and preamplifier stage. It has a pipeline storage of 192 cells. Within this memory 160 cells are reserved for buffering data. If one of these events is marked by a trigger it will be copied in the remaining 32 cells and is queued for output. The samples are written at a frequency of 40 MHz to the cells behind the amplifier stage of each channel resulting in a maximum storage time of 4 μs before the first event will be overwritten. To chose the right event tagged by the trigger, the chip has to point back in the pipeline. This is called the *latency*. The APV25 has three different modes of operation with the "multi mode" being the one of interest. In this operation mode three sequent cells of each channel are readout serially. Thus a maximum of ten triggered events can be stored on the chip. The data is then readout by an analog 128-to-1 multiplexer with a variable frequency from 20 MHz up to 40 MHz. In differential current form within the range of ± 4 mV the chip sends a digital header containing an error information and cell numbers, as shown in Fig. 8.6. This is in contrast to the GASSIPLEX readout whose signal is only digitized available.

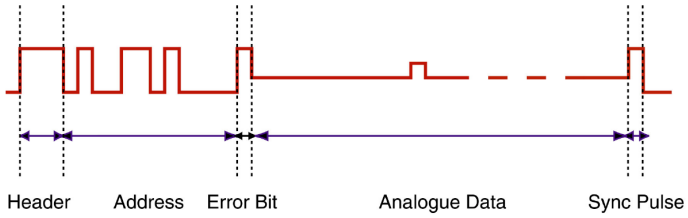

Figure 8.6: Data output of the APV25 in analogue form [Jone 01].

The header is followed by the amplitudes of each channel in the corresponding cells. It is important to note that the APV25 does not write out the channels as they are geometrically placed due to different multiplexing steps. To prevent the APV from damages caused by high signals or discharges, respectively, protection circuits are put in front of the chip in the signal line.

Fig. 8.7 shows a picture of the frontend card. The detector will be connected with the white connector on the left side. Since the APV25 reads data from 128 channels and the connector provides 130 pins, two pins are open to be connected to ground level. The protection circuit are made of a *BAV*99 diode followed by a 220 pF capacitor. Any signal higher than ± 0.7 V will be grounded to prevent damages of the electronics [Simo 01]. A pitch adapter is needed to route the channels to the $44 \mu m$ pitch of the chip. The multiplexed output signal of the APV is fed to a 26 pin connector. The -3.3 V and $+5.0$ V low voltage that the chips needs are also supplied via this connector. Additionally all required

[4] **A**nalog **P**ipeline **V**oltage

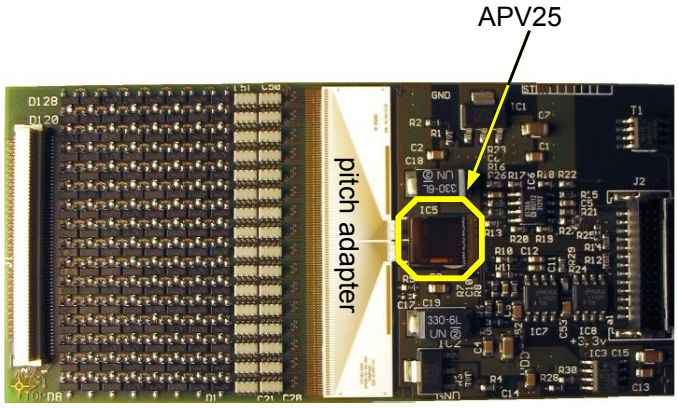

Figure 8.7: The APV frontend module designed for COMPASS triple GEM detectors [Uhl 08]. 128 channels from the detector are connected via the withe connector on the left with the frontend module and fed to the APV after passing the protection circuits and the pitch adapter. The multiplexed analog signal is readout via the 28 pin connector to the right. Communication with the chip as well as low voltage supply is ensured also within this connector.

components for communication with the APV25 are delivered this way. A detailed documentation of the chip settings can be found in [Jone 01].

8.3.2 Readout Concept for APV25 Frontend

Three APV frontend modules are needed for the triple GEM prototype 2.0 designed for an APV readout and equipped with a high segmented anode of 384 strips. To suit this requirements a readout concept was designed in collaboration with the HISKP[5] at Bonn. Based on the development of an APV readout systems for silicon-strip-detectors [Koop 10] an adapter module was designed to connect the APV25 FEs with the VME[6] based readout .

To record the multiplexed signal of a APV frontend module the data is transferred to an analogue-to-digital converter (ADC) card that is able to host four frontend modules in total. The data is digitized at 50 MHz in a 12 bit range with 65 Ms/s. It is then readout via a field-programmable-gate-array (FPGA). Since the FPGA board can contain three ADC cards it is possible to readout 4 detectors in total as shown in Fig. 8.8.
Communication with the APV chips is implemented via the I^2C standard enabling to read from and write to the APV25. The digital inputs of clock and trigger for the chip are low voltage differential signals (LVDS) and have to be generated by the FPGA board. The trigger to the FPGA board comes from the usual scintillator coincidence in NIM standard. The APV frontend cards provide the possibility of temperature monitoring with a “1-wire” connection that is illustrated on the right side in the schematic layout.
In order to use this system for the prototype 2.0 an adapter board was designed as can be seen in Fig. 8.9. The frontend modules are connected at the top of the plane. The 34 pin header in the front receives all required settings from the FPGA as well as data input and output lines. Fig. 8.10 shows the 1 : 4 multiplexer that is developed to connect four triple GEM detectors to one readout.
The planning and design of the presented readout system could be finished within this thesis. Since

[5] **H**elmholtz **I**nstitut für **S**trahlen- und **K**ernphysik
[6] **V**ersa **M**odule **E**urocard-bus

the production of the APV25 frontend modules and the other electronic components is expected to be available in early 2011 the commissioning of the triple GEM prototype 2.0 with APV based readout can be started soon.

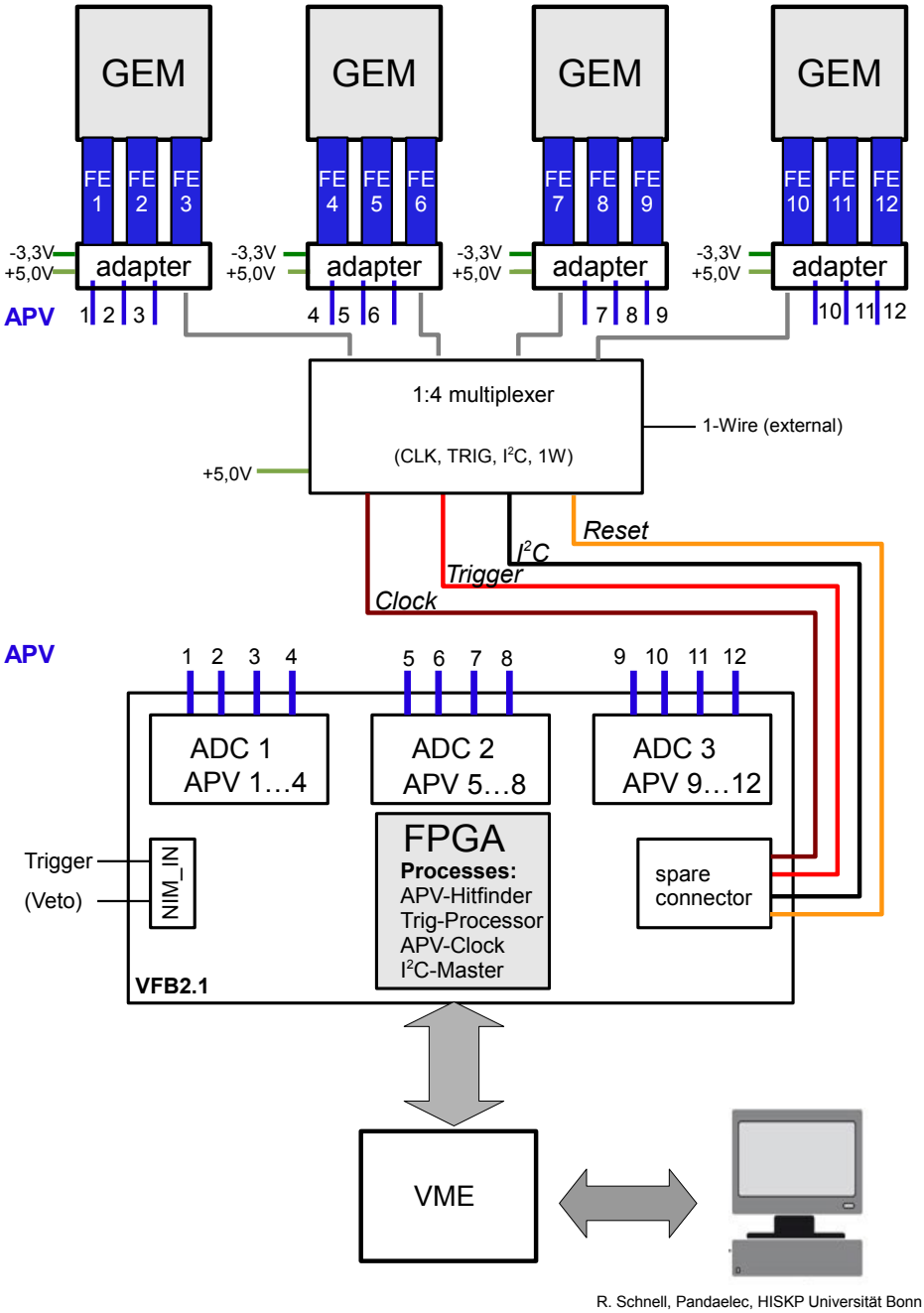

Figure 8.8: Readout concept based on APV for a tracking station containing four triple GEM detectors [Schn 10].

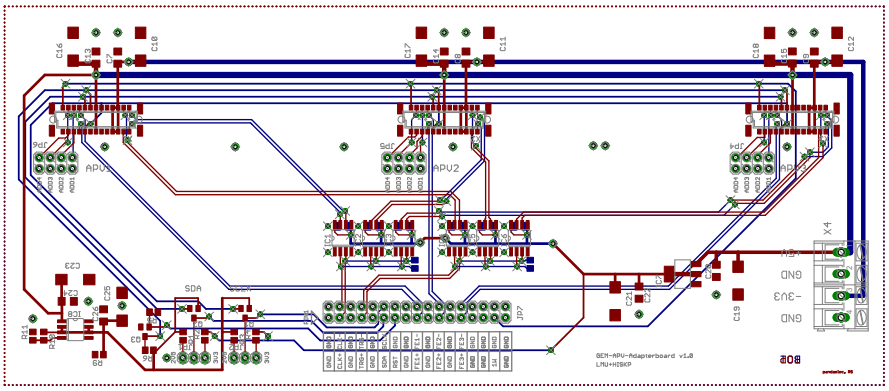

Figure 8.9: Layout of the adapter board to connect APV25 frontend module with ADC card and FPGA board [Schn 10].

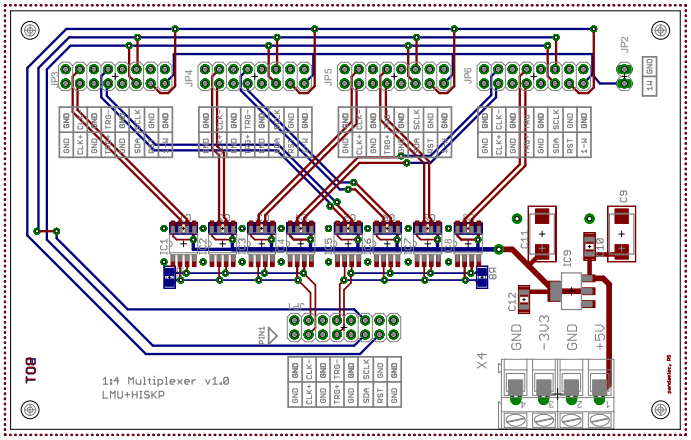

Figure 8.10: Layout of the 1:4 Multiplexer for the readout of four triple GEM detectors [Schn 10].

Chapter 9

Summary and Outlook

This work presents the construction, commissioning and operation of triple GEM detectors.
Three different detectors were built. The version with unsegmented and the second version with five-fold segmented anode are referred to as "prototype 1.0". A third version equipped with an anode segmented in 360 strips being $150\mu m$ thick at a pitch of $250\mu m$ is referred to as "prototype 2.0".
Prototype 1.0 contains three GEM foils which are mounted at a distance of 3 *mm* to each other. The distance to the anode and cathode is 3 *mm* and 4 *mm*, respectively. In prototype 2.0 all distances have been reduced by 1 *mm*. Both prototype versions are running reliably.
The GEM detectors were investigated using X-rays of a ^{55}Fe source and by cosmic ray muons. The thesis is outlined as follows:

After introducing the GEM foil principle the assembly of the detector was described. For investigation of the energy resolution a ^{55}Fe source was used. It was observed that the most characteristic peak, the 5.90 keV K_α line, is detected with a resolution of 18% FWHM. The energy spectrum of ^{55}Fe is 10% to 20% better resolved at outer regions of the active area compared to a centrally placed source location. This effect is mainly due to field deviations affecting the unstabilized GEM foils central region and does not result from any inefficiencies of the foil itself. The implementation of a spacer grid could be corrective but would reduce the active detector surface.
Cosmic muons were detected with the prototype in combination with a coincidence unit of two trigger scintillators. The pulse height spectrum represented by a Landau distribution is completely detectable and no cut off at low energies was observed. The dependence of the pulse height on the induction field was studied and observed to increase almost linearly with $0.1\frac{kV}{cm} \leq E_{ind} \leq 2.3\frac{kV}{cm}$ for X-ray measurements and $0.8\frac{kV}{cm} \leq E_{ind} \leq 2.0\frac{kV}{cm}$ for cosmic muons, respectively. As expected, the pulse height rises for higher fields owing to enhanced electron transfer processes from last GEM foil to the anode. At higher E_{ind}-fields more field lines of the amplification region are guided to the anode, extracting more charges and thus generating a higher pulse. To study this further it would be reasonable to implement a 3d simulation model of the detector since the charge transfer processes in a GEM detector are complex. Variations of the drift field E_{drift} do not impact the pulse height significantly.
With the implementation of a five-fold segmented anode the pulse height was examined as a function of segmentation. Using a theoretically derived fit function it was shown that the gas gain $G \approx 10^4$ resulting from these fits is in accordance with results obtained by explicit gain measurements. However, the investigation on capacities involved in the signal creation has to be iterated since the experimentally derived values for C_{strip} deviate by a factor of five from theory.
Concerning the efficiency of the triple GEM detector on cosmic muons it was essential to guarantee

stable flow and pressure conditions in the detector. In this way efficiencies of $\varepsilon_{corr} > 95\%$ could be achieved. Furthermore, an influence of the temperature could be observed by cooling the detector which results in a decrease of ε_{corr}. Monitoring the temperature additionally to flow and pressure control is thus recommended.
The triple GEM detector presented in this work is filled with Ar/CO_2 in the ratio $93/7$ and provides an effective gain $G_{eff} = 10^4$. The applicable potential difference ΔU_{GEM} is limited to approximately 350 V due to frequent discharges of $\mathcal{O}(\text{discharge}) \approx 1\text{min}^{-1}$ at higher values.
The most stable working point of the triple GEM prototype 1.0 is:
$E_{ind} = 1.25\frac{kV}{cm}$, $E_{trans1,2} = E_{ind} = 2.00\frac{kV}{cm}$ for the electric fields in the gap regions and $\Delta U_{GEM1} = 320$ V, $\Delta U_{GEM}2 = 340$ V and $\Delta U_{GEM3} = 360$ V at the GEM foils, respectively. With this setup a stable operation of the detector in long term overnight-measurements is ensured.
Furthermore, the signal rise time was analyzed as a function of electric field in the induction gap, E_{ind}. In preparation for this analysis a GARFIELD / MAGBOLTZ simulation was implemented to study the electron drift time in the drift region of the detector depending on the electric field. It was found that the rise time by X-ray generated signals follows the drift time of electrons in the 3 mm induction gap. This could be observed for ^{55}Fe measurements in the range $0.1\frac{kV}{cm} \leq E_{ind} \leq 2.3\frac{kV}{cm}$ as well as for cosmic muons in the range $0.8\frac{kV}{cm} \leq E_{ind} \leq 2.0\ \frac{kV}{cm}$. This leads to the conclusion that the signals in the triple GEM detector are dominated by electrons and not by ion induced pulses.

A prototype 2.0 with highly segmented strip anode is meanwhile realized. The active area of the anode is divided in $150\mu m$ thick copper strips with $250\mu m$ pitch. In cooperation with the TU Munich (E18) and HISKP Bonn a readout system is designed based on APV25 frontend modules. A first prototype 2.0 setup including the APV readout is probably available in early 2011.

A complete readout system based on the GASSIPLEX frontend modules is implemented and data are taken just now. Mounted in a table top tracking station, a first sample of 1083 muon events is recorded. 90.6% of all tracks are considered for the fit that provides $79 \pm 5\mu m$ spatial resolution of the triple GEM detector.
In combination with MICROMEGAS detectors developed simultaneously to this work this setup promises to be reliable for track reconstruction of cosmic muons with high resolution. Tests of the triple GEM detectors' tracking capability of 140 GeV muons at the H8 beam line at CERN and their position accuracy of cosmic muon detection at increased background of gammas or neutrons are foreseen.

Bibliography

[Adom 10] S. Adomeit. "Konstruktion, Bau und Einsatz eines Szintillator-Trigger-Hodoskops". Ludwig-Maximilians-Universität Munich, January 2010. Diploma thesis.

[Altu 02] C. Altunbas, M. Capans, K. Dehmelt, J. Ehlers, J. Friedrich, I. Konorov, A. Gandi, S. Kappler, B. Ketzer, R. D. Oliveira, S. Paul, A. Placci, L. Ropelewski, F. Sauli, F. Simon, and M. van Stenis. "Construction, test and commissioning of the triple-gem tracking detector for compass". *Nucl. Instr. and Meth. A*, Vol. 490, No. 1-2, pp. 177 – 203, 2002.

[ATLA 10] ATLAS. "The Atlas etours". http://atlas.ch/etours.html, November 2010.

[Bach 01a] S. Bachmann, A. Bressan, B. Ketzer, M. Deutel, L. Ropelewski, F. Sauli, A. Bondar, A. Buzulutskov, L. Shekhtman, A. Sokolov, A. Tatarinov, A. Vasil'ev, S. Kappler, and E. Schulte. "Performance of GEM detectors in high intensity particle beams". *Nucl. Instr. and Meth. A*, Vol. 470, No. 3, pp. 548 – 561, 2001.

[Bach 01b] S. Bachmann, A. Bressan, B. Ketzer, M. Deutel, L. Ropelewski, F. Sauli, S. Kappler, and E. Schulte. "Optimisation of the gas electron multiplier for high rate applications". *Nucl. Instr. and Meth. A*, Vol. 461, No. 1-3, pp. 42 – 46, 2001. 8th Pisa Meeting on Advanced Detectors.

[Bach 02] S. Bachmann, A. Bressan, M. Capeáns, M. Deutel, S. Kappler, B. Ketzer, A. Polouektov, L. Ropelewski, F. Sauli, E. Schulte, L. Shekhtman, and A. Sokolov. "Discharge studies and prevention in the gas electron multiplier (GEM)". *Nucl. Instr. and Meth. A*, Vol. 479, No. 2-3, pp. 294 – 308, 2002.

[Bach 99] S. Bachmann, A. Bressan, L. Ropelewski, F. Sauli, A. Sharma, and D. Mrmann. "Charge amplification and transfer processes in the gas electron multiplier". *Nucl. Instr. and Meth. A*, Vol. 438, No. 2-3, pp. 376 – 408, 1999.

[Benl 98] J. Benlloch, A. Bressan, M. Capens, M. Gruw, M. Hoch, J. C. Labb, A. Placci, L. Ropelewski, and F. Sauli. "Further developments and beam tests of the gas electron multiplier (GEM)". *Nucl. Instr. and Meth. A*, Vol. 419, No. 2-3, pp. 410 – 417, 1998.

[Beus 94] W. Beusch, S. Buytaert, C. Enz, E. Heijne, P. Jarron, F. Krummenacher, F. Piuz, and J. Santiard. "Gasplex a low analog signal processor for readout of gaseous detectors". *Internal note*, Vol. CERN-ECP/94-17, 1994.

[Bich 06] H. Bichsel. "A method to improve tracking and particle identification in TPCs and silicon detectors". *Nucl. Instr. and Meth. A*, Vol. 562, No. 1, pp. 154 – 197, 2006.

[Bieb 03] O. Biebel, M. Binder, M. Boutemeur, A. Brandt, J. Dubbert, G. Duckeck, J. Elmsheuser, F. Fiedler, R. Hertenberger, O. Kortner, T. Nunnemann, F. Rauscher, D. Schaile, P. Schieferdecker, A. Staude, W. Stiller, R. Stroehmer, and R. Vertesi. "A Cosmic Ray Measurement Facility for ATLAS Muon Chambers". *ArXiv Physics e-prints*, No. arXiv:physics/0307147, July 2003.

[Bieb 08] O. Biebel. "Detektoren für Teilchenstrahlung". Lecture at Ludwig-Maximilians-Universität Munich, 2008.

[Bij 05] E. van der Bij (CERN-EST-DEM). "Features of Gas Electron Multiplier GEM-100x100-140-70/50-P-F SCEM: 08.82.00.101.4". http://ts-dep-dem.web.cern.ch/ts-dep-dem/products/gem/stores/GEM-100-100-140-70-50-P-F.htm, 2005.

[Bohm 99] M. Böhmer. "Das Auslesesystem fr den Ringabbildenden Cerenkovdetektor im HADES Spektrometer". Technical University Munich, 1999. Diploma thesis.

[Bort 10] J. Bortfeldt. "Development of Micro-Pattern Gaseous Detectors - Micromegas". Ludwig-Maximilinas-Universität Munich, November 2010. Diploma thesis.

[Buzu 02] A. Buzulutskov. "Physics of multi-GEM structures". *Nucl. Instr. and Meth. A*, Vol. 494, pp. 148–155, Nov. 2002.

[CAEN 10] CAEN. "MOD. V1729 Revision n. 8 4 CHANNEL/12BIT SAMPLING ADC MANUAL REV.8". http://www.caen.it, February 2010.

[CANB 07] CANBERRA Industries. "CANBERRA Model 2004 Semiconductor Detector PreamplifierData Sheet". http://www.canberra.com, 2007.

[CERN 10] CERN. "Homepage". http://public.web.cern.ch/public/, November 2010.

[Deil 04] M. Deile, J. Dubbert, S. Horvat, O. Kortner, H. Kroha, A. Manz, S. Mohrdieck-Mck, F. Rauscher, R. Richter, A. Staude, and W. Stiller. "Resolution and efficiency of the ATLAS muon drift-tube chambers at high background rates". *Nucl. Instr. and Meth. A*, Vol. 535, No. 1-2, pp. 212 – 215, 2004. Proceedings of the 10th International Vienna Conference on Instrumentation.

[Engl 09] A. Engl, O. Biebel, R. Hertenberger, R. Mameghani, D. Merkl, F. Rauscher, D. Schaile, and R. Stroehmer. "Temperature Studies for ATLAS MDT BOS Chambers". *ArXiv e-prints*, No. 0908.1541, Aug. 2009.

[Fano 47] U. Fano. "Ionization Yield of Radiations. II. The Fluctuations of the Number of Ions". *Phys. Rev.*, Vol. 72, No. 1, pp. 26–29, Jul 1947.

[Grif 08] D. J. Griffiths. *Introduction to Elementary Particles; 2nd ed. TextBook Physics*, Wiley, New York, NY, 2008.

[Groo 01] D. E. Groom, N. V. Mokhov, and S. I. Striganov. "Muon Stopping WPower and Range Tables 10 MeV - 100 TeV". *Atomic Data and Nuclear Data Tables*, Vol. 78, No. 2, pp. 183 – 356, 2001.

[Grup 08] C. Grupen and B. Shwartz. *Particle Detectors*. Cambridge University Press, 2008.

[Gued 03] G. P. Guedes, A. Breskin, R. Chechik, and D. Mrmann. “Effects of the induction-gap parameters on the signal in a double-GEM detector”. *Nucl. Instr. and Meth. A*, Vol. 497, No. 2-3, pp. 305 – 313, 2003.

[Haas 04] F. Haas. “Design and Commissioning of a General Purpose Triple GEM and Installation of a GEM Tracking Detector at COMPASS”. 2004. Diploma thesis.

[Hash 84] A. Hashiba, K. Masuda, T. Doke, T. Takahashi, and Y. Fujita. “Fano factor in gaseous argon measured by the proportional scintillation method”. *Nucl. Instr. and Meth. A*, Vol. 227, No. 2, pp. 305 – 310, 1984.

[iseg 01] iseg. *Operator Manual for High Voltage Power Supply SHQ HIGH PRECISION series with RS232 interface*. iseg Spezialelektronik GmbH, Bautzner Landstr. 23 D - 01454 Radeberg / Rossendorf, October 2001.

[Jone 01] L. Jones. *APV25-S1: User guide version 2.2*. RAL Microelectronics Design Group, Chilton, 2001.

[Karg 10] J. Karg. “Schematics of the charge sensititve preamplifier 2003-1 by Karg”. eagle board and schematics, 2010.

[Ketz 03] B. Ketzer, J. Ehlers, J. Friedrich, B. Grube, S. Kappler, I. Konorov, S. Paul, A. Placci, L. Ropelewski, and F. Sauli. “A fast Tracker for COMPASS based on the GEM”. *Nuclear Physics B - Proceedings Supplements*, Vol. 125, pp. 368 – 373, 2003. Innovative Particle and Radiation Detectors.

[Ketz 04] B. Ketzer, Q. Weitzel, S. Paul, F. Sauli, and L. Ropelewski. “Performance of triple GEM tracking detectors in the COMPASS experiment”. *Nucl. Instr. and Meth. A*, Vol. 535, No. 1-2, pp. 314 – 318, 2004. Proceedings of the 10th International Vienna Conference on Instrumentation.

[Klei 92] K. Kleinknecht. *Detektoren für Teilchenstrahlung*. Teubner Studienbücher, 1992.

[Kolb 84] K. S. Kölbig and B. Schorr. “A program package for the Landau distribution”. *Computer Physics Communications*, Vol. 31, No. 1, pp. 97 – 111, 1984.

[Koop 10] K. Koop, M. Becker, K. Brinkmann, T. Wrschig, and H. Zaunick. “Entwicklung eines Auslesesystems für Silizium-Streifen-Detektoren”. DPG conference Bonn, March 2010. Poster.

[Leo 94] W. R. Leo. *Techniques for Nuclear and Particle Physics Experiments*. Springer, second Ed., 1994.

[Loeb 10] J. v. Loeben, B. Bittner, J. Dubbert, M. Kilgenstein, O. Kortner, S. Kortner, H. Kroha, R. Richter, P. Schwegler, S. Adomeit, O. Biebel, A. Engl, R. Hertenberger, F. Legger, F. Rauscher, and A. Zibell. “Performance of Fast High-Resolution Muon Drift Tube Chambers for LHC Upgrades”. IEEE Nuclear Science Symposium and Medical Imaging Conference 2010, Knoxville, November 2010.

[Murt 02] F. Murtas. “Development of a gaseous detector based on Gas Electron Multiplier (GEM) Technology”. Instituto Nazionale di Fisica Nucleare, Frascati, November 2002. SRG Lab Seminar.

[NIST 10] NIST. "XCOM: Photon Cross Sections Data". http://www.nist.gov/pml/data/xcom/index.cfm, November 2010. National Institue of Standards and Technology.

[Nuhr 02] D. Nührmann. *Das komplette Werkbuch Elektronik*. Franzis' Verlag, 2002.

[PDG 10] PDG. "The Review of Particle Physics". *Journal of Physics G*, Vol. 37, No. 075021, July 2010. Particle Data Group.

[Saul 03] F. Sauli. "Development and applications of gas electron multiplier detectors". *Nucl. Instr. and Meth. A*, Vol. 505, No. 1-2, pp. 195 – 198, 2003. Proceedings of the tenth Symposium on Radiation Measurements and Applications.

[Saul 04] F. Sauli. "GEM HANDLING". Delivered with GEM foils by CERN-PH-TA1-Gas Detectors, 2004.

[Saul 77] F. Sauli. "Principles of Operations of Multiwire Proportional and Drift Chambers". CERN 77-09, 1977.

[Saul 97] F. Sauli. "GEM: A new concept for electron amplification in gas detectors". *Nucl. Instr. and Meth. A*, Vol. 386, No. 2-3, pp. 531 – 534, 1997.

[Schn 10] R. Schnell. "Private communications during visit in Munich". October 2010.

[Semi 10] F. Semiconductor. "Samll signal diode BAV99". http://www.fairchildsemi.com, 2010.

[Shar 00a] A. Sharma. "3D simulation of charge transfer in a Gas Electron Multiplier (GEM) and comparison to experiment". *Nucl. Instr. and Meth. A*, Vol. 454, No. 1, pp. 267 – 271, 2000.

[Shar 00b] A. Sharma. "A How-to Approach for a 3d Simulation of Charge Transfer Characteristics in a Gas Electron Multiplier (GEM)". *ICFA Journal*, 2000.

[Shar 93] A. Sharma and F. Sauli. "First Townsend coefficient measured in argon based mixtures at high fields". *Nucl. Instr. and Meth. A*, Vol. 334, No. 2-3, pp. 420 – 424, 1993.

[Simo 01] F. Simon. "Commissioning of the GEM Detectors in the COMPASS Experiment". 2001. Diploma thesis.

[Spie 05] H. Spieler. "Radiation Detectors and Signal Processing". http://www-physics.lbl.gov/, October 2005. Lecture series for University of Heidelberg, Oct.10-Oct.14, 2005.

[Thwa 83] D. I. Thwaites. "Bragg's Rule of Stopping Power Additivity: A Compilation and Summary of Results". *Radiation Research*, Vol. 95, No. 3, pp. pp. 495–518, 1983.

[Tran 87] Transchel Nuklear Elektronik. "Charge and time sensitive preamplifier CATSA 82". Data sheet, delivered with device, december 1987.

[Uhl 08] S. Uhl. "Construction and Commissioning of the PixelGEM Tracking System for the COMPASS Experiment". 2008. Diploma thesis.

[Veen 98] R. Veenhof. "Garfield, recent developments". *Nucl. Instr. and Meth. A*, Vol. 419, No. 2-3, pp. 726 – 730, 1998.

[Volt 07] Voltcraft. “VOLTCRAFT DL-120 TH USB-Temperature- and Moisture-Datalogger”. March 2007.

[Weit 03] Q. Weitzel. “Triple GEM Detectors in COMPASS - A Performance Study”. 2003. Diploma thesis.

[Zeit 99] K. Zeitelhack, A. Elhardt, J. Friese, R. Gernhuser, J. Homolka, A. Kastenmller, P. Kienle, H.-J. Krner, P. Maier-Komor, M. Mnch, W. Przygoda, W. Schn, A. Ulrich, and J. Wieser. “The HADES RICH detector”. *Nucl. Instr. and Meth. A*, Vol. 433, No. 1-2, pp. 201 – 206, 1999.

Appendix A

Assumptions for Efficiency Simulation

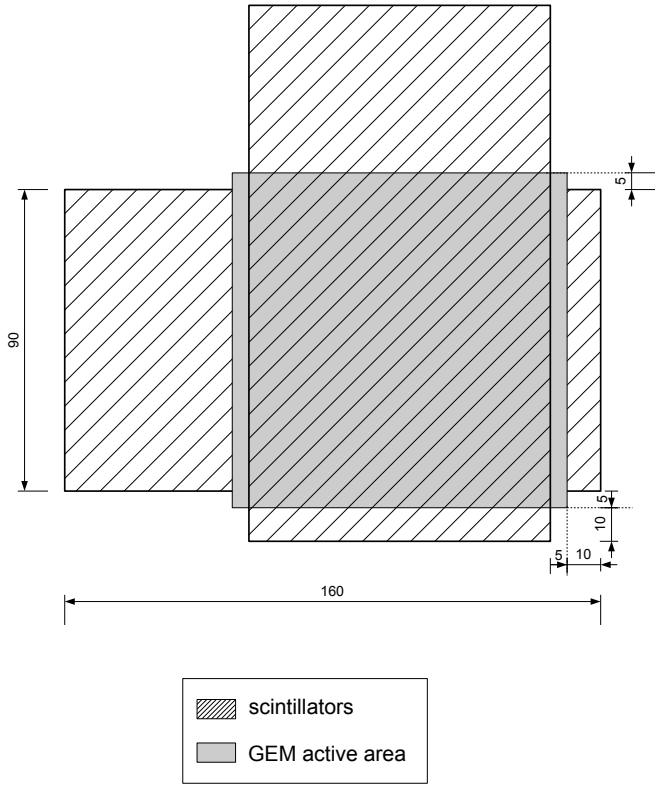

Figure A.1: Positioning and dimensions of the triple GEM enclosed by two scintillators as used for Monte Carlo Simulation to calculated the geometrical correction factor f_{corr}

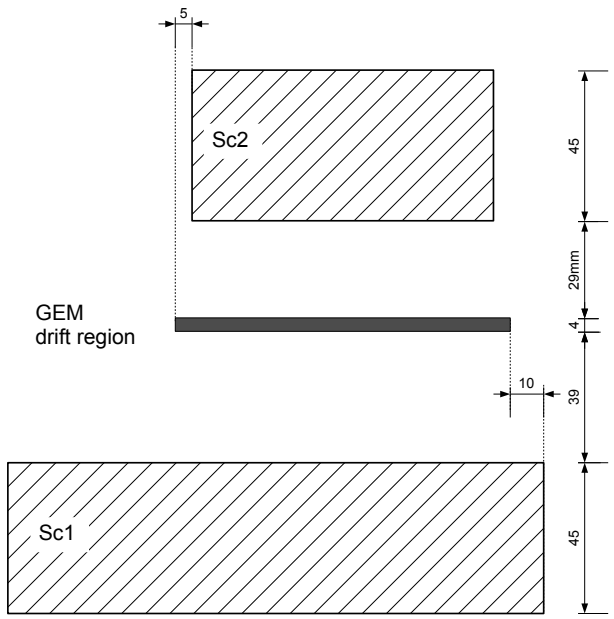

Figure A.2: Dimensions of the Detectors used for Monte Carlo Simulation

Appendix B

Construction Drawings of Prototype 1.0

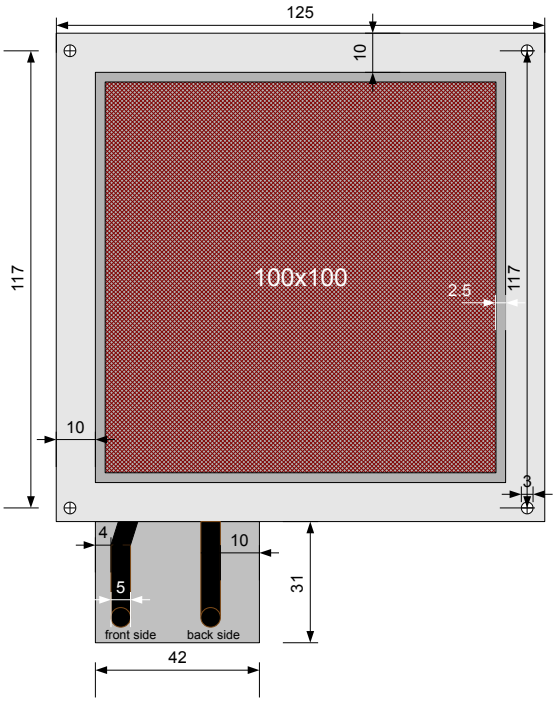

Figure B.1: Dimensions of the framed standard-designed GEM foil by CERN

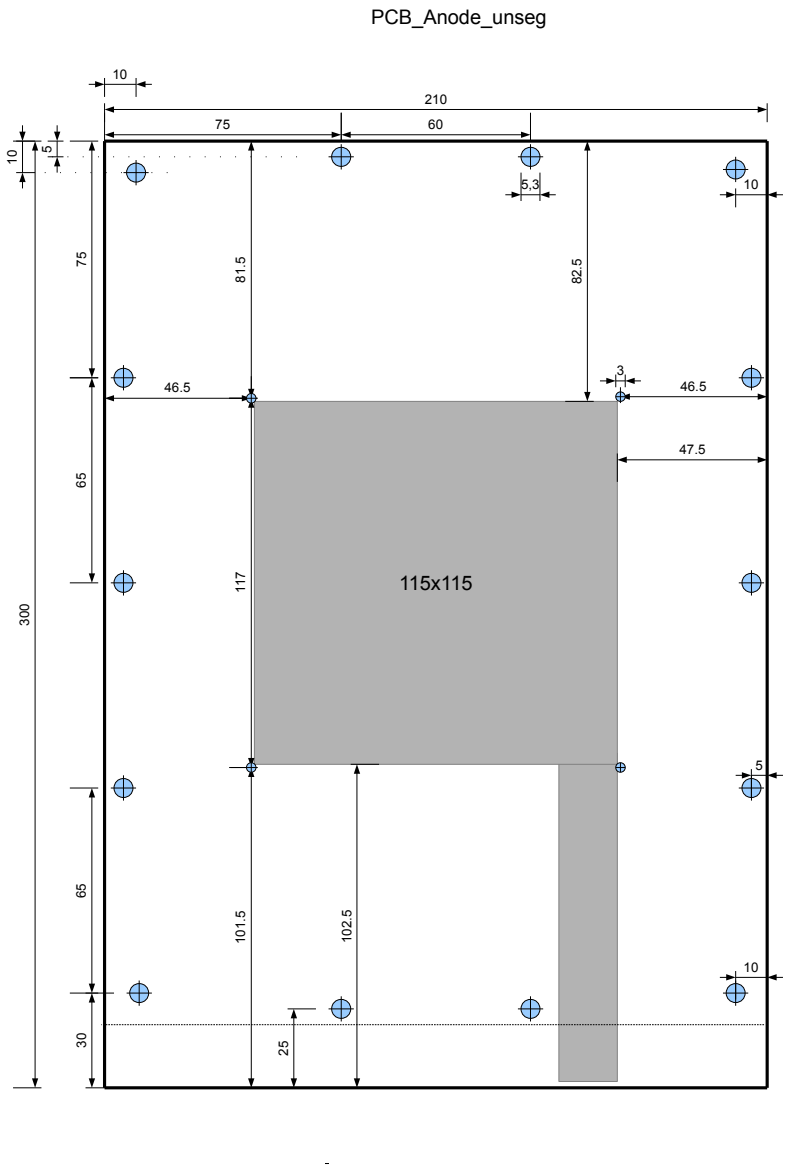

Figure B.2: Unsegmented readout plane with 115 x 155 mm^2 copper anode of prototype 1.0

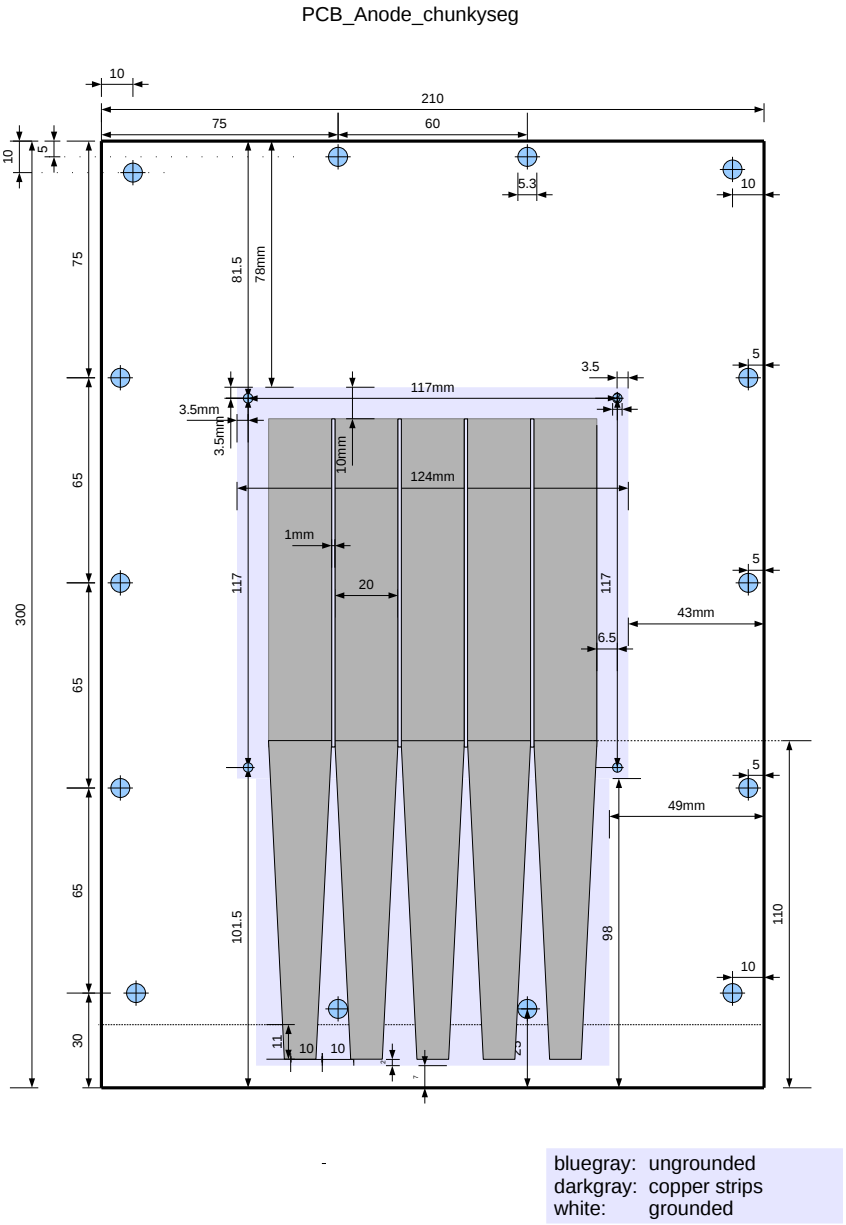

Figure B.3: Fivefold segmented anode of prototype 1.0

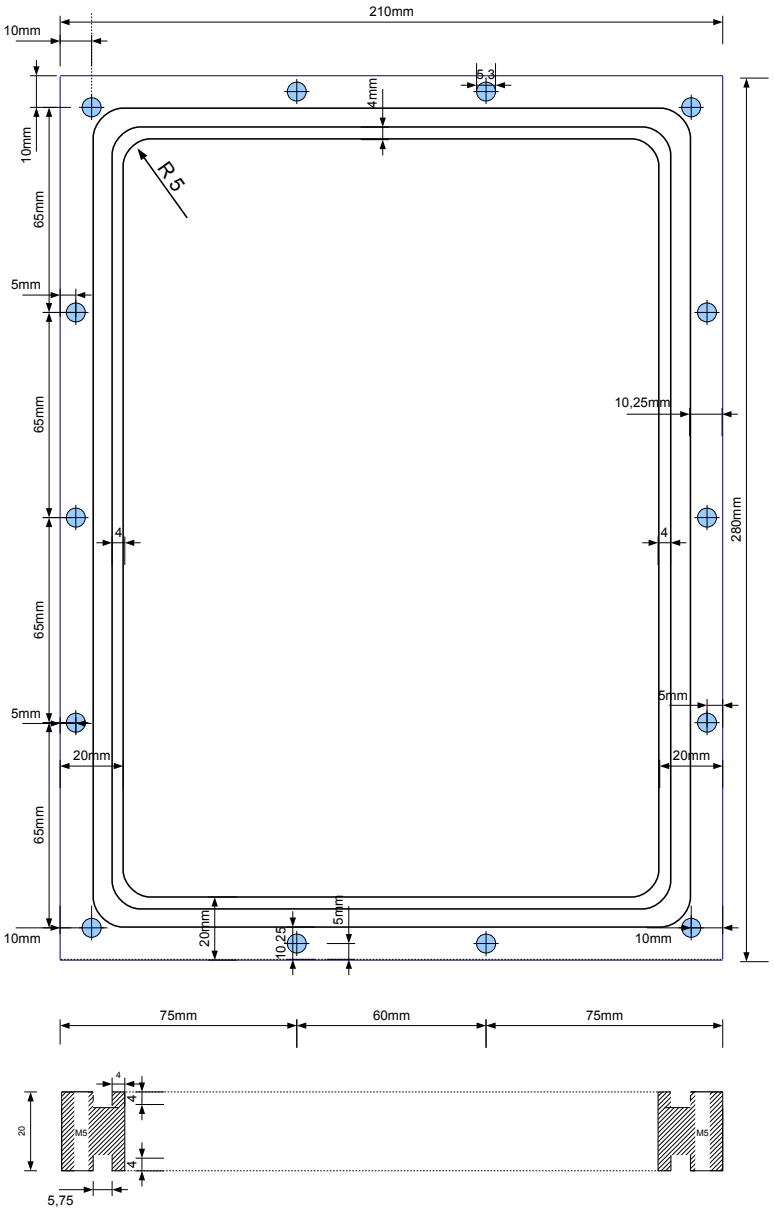

Figure B.4: Frame of prototype 1.0

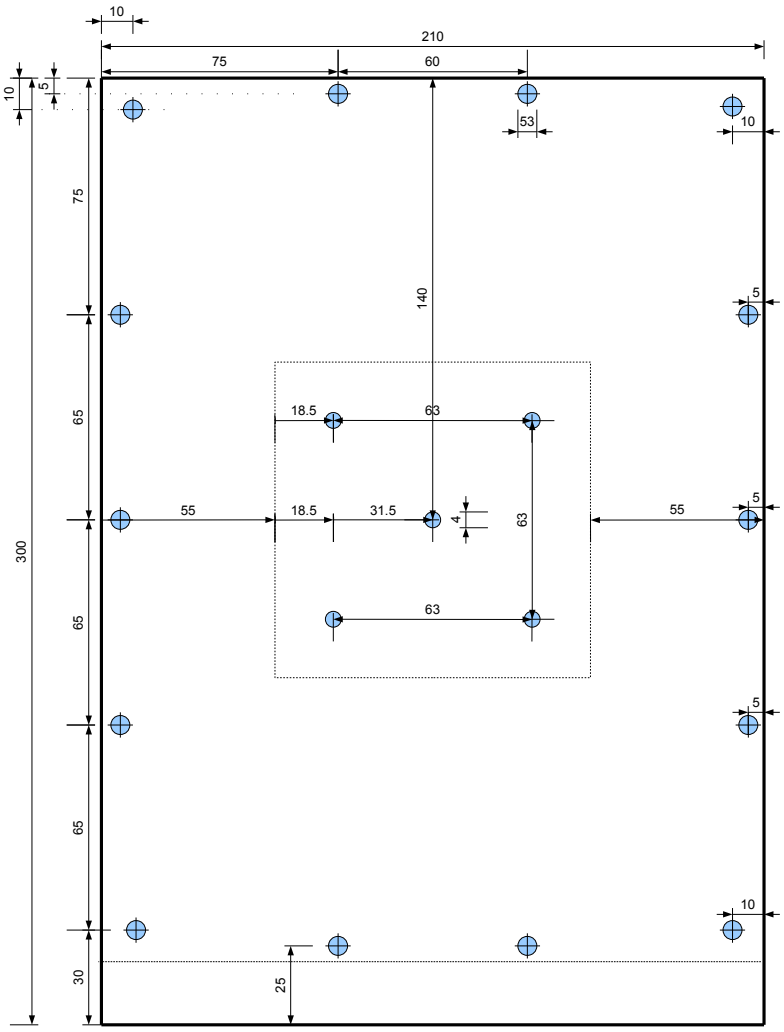

Figure B.5: Top plate of prototype 1.0 with five drills for X-ray inlet.

Appendix C

Design of Prototype 2.0

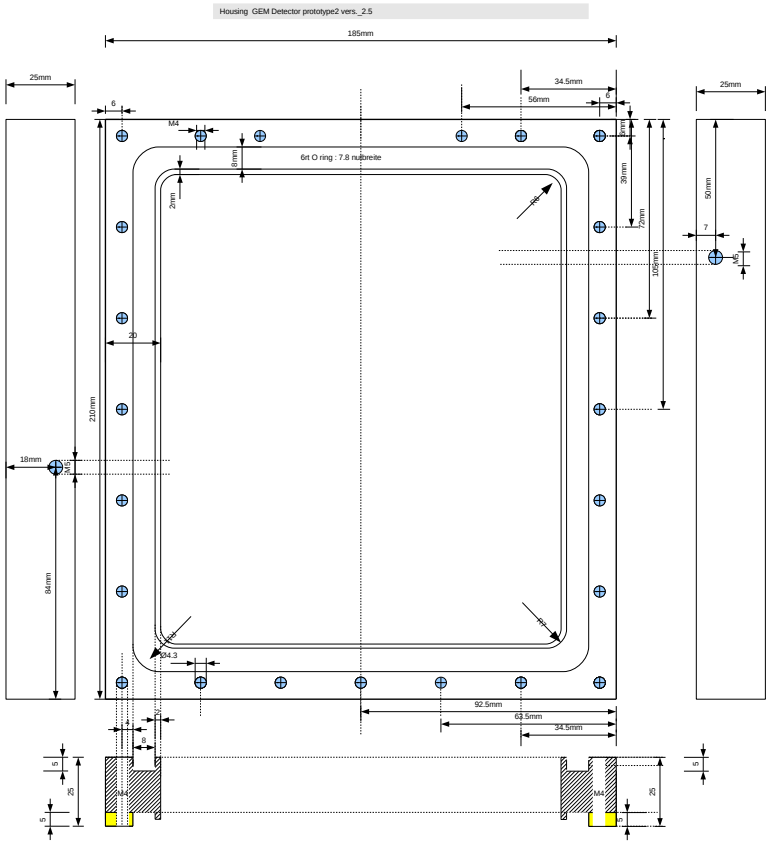

Figure C.1: Schematic of the frame of prototype 2.0. It includes a gas volume of $25 \times 145 \times 170\text{mm}^3 = 0.62l$.

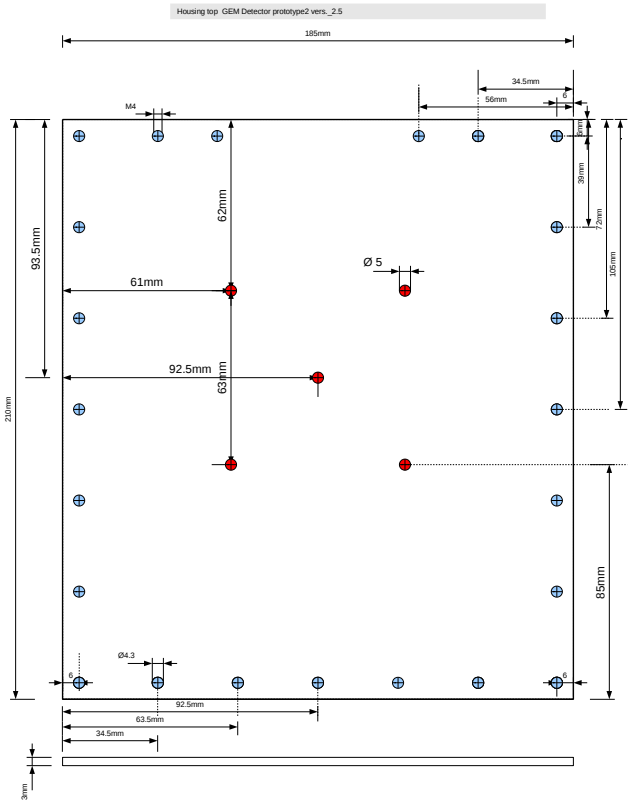

Figure C.2: Schematic of the top plate of prototype 2.0.

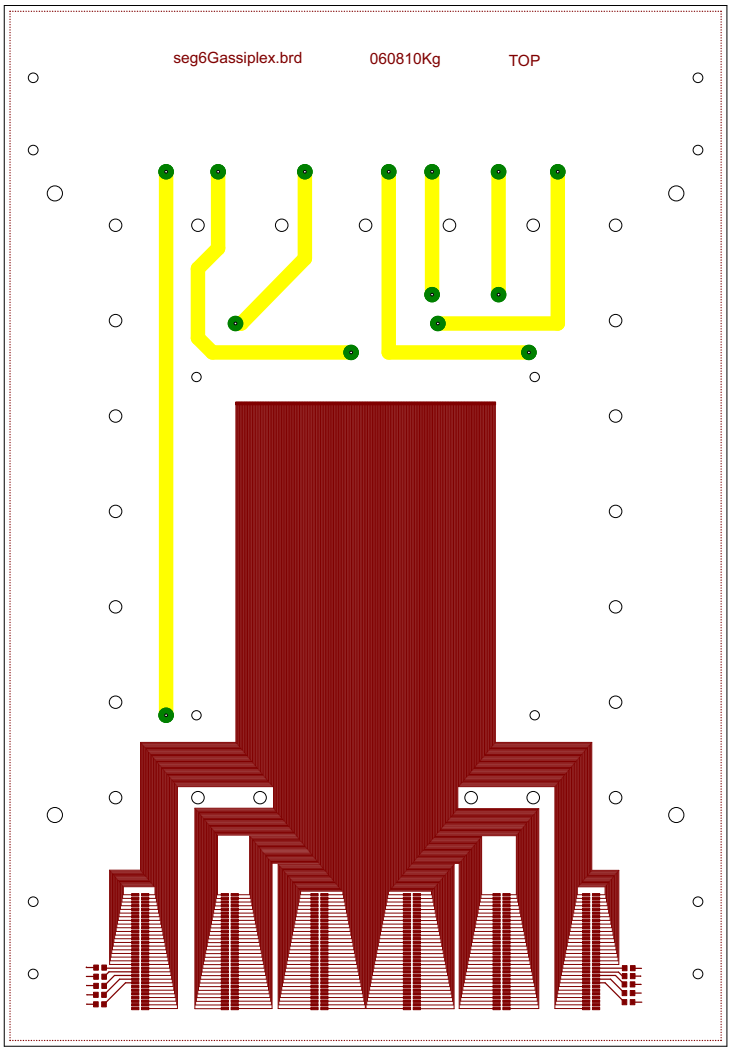

Figure C.3: *eagle* layout of the anode of prototype 2.0 (by J. Karg, ELab LMU) for readout with 6 Gassiplex Frontends

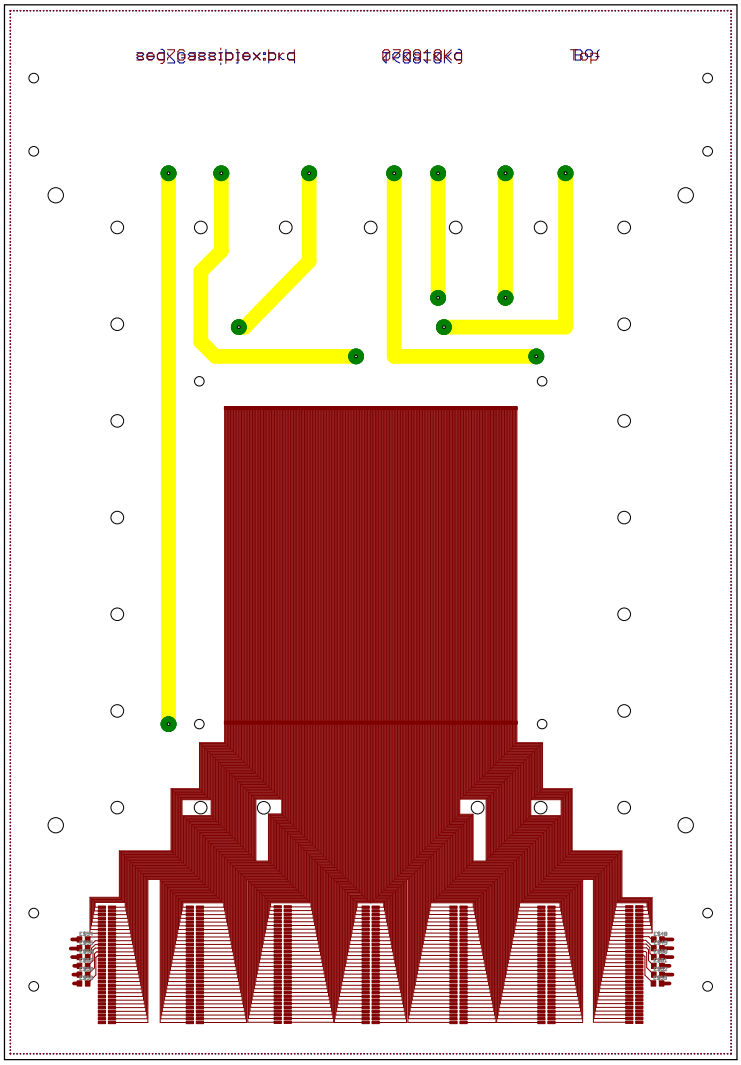

Figure C.4: *eagle* layout of the anode of prototype 2.0 (by J. Karg, elec. Workshop LMU) for readout with 7 Gassiplex Frontends

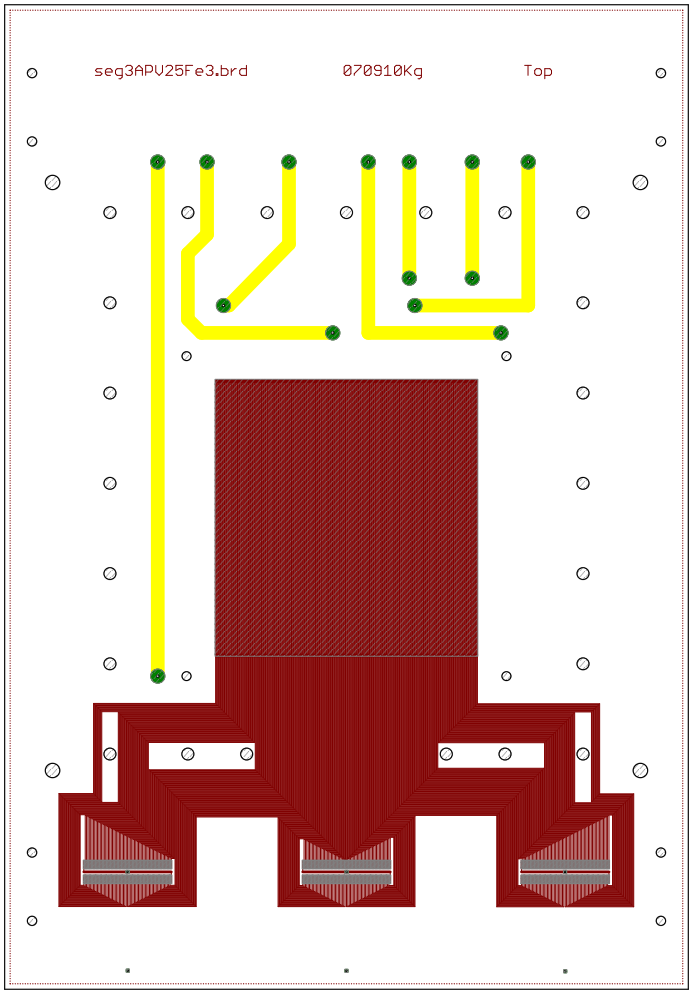

Figure C.5: *eagle* layout of the anode of prototype 2.0 (by J. Karg, elec. Workshop LMU) for readout with 3 APV Frontends

Appendix D

Software

D.1 Programs for Communication with *iseg* SHQ high voltage supply

All programs developed for HV control of the detector can be found in the directory:
/data/etp6/heereman/iseg/
After loading the required libraries with `isegload.C`, the program `isegcontrol_gem.C`is responsible for providing voltage limits via RS232 commands to the several HV devices. An important feature of the RS232 interface control program is, that it periodically checks, if a discharge occurred in the detector.

D.2 Algorithms for Signal Analysis

All programs developed for signal analysis can be found in the directory:
/data/etp6/heereman/data/

Acknowledgements

First of all I would like to thank my advisor Prof. Otmar Biebel for the opportunity to write this thesis. I am grateful for his invaluable support and advice over the last year.

I am deeply indebted to Dr. Ralf Hertenberger for the excellent supervision throughout the entire thesis process. I appreciate the assistance he provided at all levels of the research project.

My sincere thanks are due to Prof. Dorothee Schaile for the cordial welcome at her chair.

I owe gratitude to Prof. Wolfgang Dünnweber for being the second advisor of this thesis.

I would like to thank Jonathan Bortfeldt for his precious company during the last six years, his encouragement and becoming a real friend.
I am grateful for the support of Alexander Ruschke, Albert Engl, Andrè Zibell and Nicola Tyler, who offered helpful advice in the hardware group meetings and on the balcony.

I would also like to thank Marcus Otten for his editing assistance.

Thanks are also due to the entire working group for creating a pleasant and friendly atmosphere in Munich and at conferences, Stefanie Adomeit, Steve Beale, Dr. Philippe Calfayan, Dr. Günter Duckeck, Johannes Ebke, Dr. Johannes Elmsheuser, Dr. Marie-Helene Genest, Julien de Graat, Dr. Christian Kummer, Dr. Federica Legger, Markus Lichtnecker, Jeanette Lorenz, Christoph Anton Mitterer, Christian Meineck, Dr. Thomas Müller, PD Dr. Thomas Nunnemann, Dr. Felix Rauscher, Dr. Michiel Sanders, Christopher Schmitt, Dr. Cedric Serfon, Attila Varga, Tobias Verlage, M.Sc. Dan Vladoiu, Josipa Vujaklija, Dr. Rod Walker, Jonas Will as well as Josephine Wittkowski and Dr. Xuai Zhuang.

I further would like to thank the members of the electronic laboratory of the LMU at Garching, Johann Karg, Johann Krapfl and Peter Klemm for the production of the required electronics, especially for the implementation of the layout of the highly segmented anode.

A special thanks goes to the entire mechanical laboratory of the LMU at Garching for the production of the triple GEM detector housing.

Especially I would like to thank Robert Schnell from the HISKP in Bonn for his help and support in the development of the APV readout system.

Further thanks to Bernhard Ketzer at the TU Munich for providing the APV25 frontend modules.

I am grateful to my parents, Ingrid and Hubertus Heereman, for the support they provided throughout my entire studies. I would like to thank my partner Maria for her love and for giving me encouragement throughout the years.

Last not least I may thank my fellow students Niklas Boers, Hannes Huster, Sabine Hemmer, Sven Schneider, Sina Fietz, Isabelle Huber and Nino Karpf with whom I shared the ups and downs of student life.

Selbständigkeitserklärung

Ich versichere hiermit, die vorliegende Arbeit selbständig verfasst zu haben und keine anderen als die angegebenen Quellen und Hilfsmittel verwendet zu haben.

David Heereman v. Zuydtwyck

München, den 23. November 2010